論文 / 著書情報
Article / Book Information

題目(和文)	相互作用する高速プラズマ流を用いた実験室天体物理への試み
Title(English)	An Experimental Approach to Astrophysical Phenomena using Interacting High-Speed Plasma Flow
著者(和文)	足立興市郎
Author(English)	Koichiro Adachi
出典(和文)	学位:博士(工学), 学位授与機関:東京工業大学, 報告番号:甲第9519号, 授与年月日:2014年3月26日, 学位の種別:課程博士, 審査員:堀岡　一彦,奥野　喜裕,赤塚　洋,長谷川　純,河村　徹,高橋　努
Citation(English)	Degree:Doctor (Engineering), Conferring organization: Tokyo Institute of Technology, Report number:甲第9519号, Conferred date:2014/3/26, Degree Type:Course doctor, Examiner:,,,,,
学位種別(和文)	博士論文
Type(English)	Doctoral Thesis

An Experimental Approach to Astrophysical Phenomena using Interacting High-speed Plasma Flow

Koichiro Adachi

The Interdisciplinary Graduate School
of Science and Engineering
Tokyo Institute of Technology

Department of Energy Sciences
Supervisor: Professor Kazuhiko Horioka

February 27, 2014

Contents

List of Figures

List of Tables

Chapter 1

Introduction

1.1 Background and Motivation

Recently, human active region is expanding rapidly in the space. The cold war between the United States and the Soviet Union became a trigger of the energetic space development race. While the cold war advanced technology of rockets, artificial satellites and nuclear weapons to watch and attack the hostile country from far away, it also extended the human active region. Yuri Gagarin, an astronaut in Soviet Union, became the first human being who reached outside the Earth in 1961. As of June 2013, a total of 532 people from 36 countries have reached 100 km (altitude of boundary between the Earth and the universe) or more in altitude. In 1969, in NASA(The National Aeronautics and Space Administration)'s Project, Apollo11 successfully transported humans to the surface of the Moon. Now, the manned exploration is going to reach the Mars. Manned explorations to the Mars are planned by ESA(The European Space Agency) and NASA respectively after 2030. On the other hand, on September 12, 2013, NASA announced that Voyager 1(launched by NASA on September 5, 1977) had crossed the heliopause and entered interstellar space on August 25, 2012, making it the first manmade object to do so. Thus, the human active region is gradually and definitely extending.

On the other hand, charged particles called cosmic rays shower on astronauts and/or artificial satellites in the space. Basically, it is difficult for human being to

live in the space without protective measures. In general, the energetic particles causes DNA damage in a human body. Also, one high-energy charged particle can cause great damges on electric circuits of the satellite by induced electro-magnetic field. The cosmic rays come from anywhere in the space with a power low spectrum of kinetic energy ranging from ~ 10 to $\sim 10^{20}$ eV [1–3]. Astronauts in ISS(International Space Station) are exposed usually to the radiation of about 1 mSv per day. Solar flare, which is a sudden brightening observed over the Sun's surface or the solar limb, is interpreted as a large energy release of up to 6×10^{25} joules, which exposes 10-100 mSv/burst of radiation to the astronauts outside ISS. Generally, a dose of 4000 mSv is considered to be fatal to human body.

In 1912, Victor Hess conducted a measurement with Wulf electrometers and a free balloon that revealed the cosmic rays enter Earth's atmosphere from the space [4]. Recently, the origins of cosmic ray have been considered to be astrophysical phenomena relevant to high-energy-density plasma such as solar activity, shock acceleration in supernovae and active galactic nucleus jets. Hence high-speed plasma flows relate to the generation of the cosmic rays.

The high-speed plasma flows and the cosmic rays may induce the climate change of our planet. A report that says cosmic rays affect the earth's environment was published [5]. Also, high-speed plasma flows cause escape of planet's atmosphere [6,7]. Most of cosmic rays measured near the Earth have a root in the solar wind from the Sun. High-speed charged particles mainly composed of protons and electrons are decelerated by magnetosphere of the Earth and dissipates their kinetic energy mostly through a shock formation. Highly energetic particles sometimes penetrate over the magnetic barrier of the Earth. Global motion of geomagnetic tail with annihilation of magnetic field due to magnetic reconnection also passes the high energy particles into the Earth's surface. However, the Mars and the Venus do not have the global magnetic field sufficient to protect the energetic particles and, as a result, solar wind interacts directly with their ionospheres and upper atmospheres. Then atmosphere's particles can get momentum of solar wind particles and escape from these planets

for a long time. Collisional process induced by the high energy particles plays an important role for the escape of atmospheric matter.

Among astrophysical phenomena relevant to high-speed plasma flows, plasma shocks are regarded as the most likely origin of high energy particles, because the power low spectrum can be explained by Fermi acceleration model and diffusive shock acceleration model [1, 8, 9]. Therefore, relativistic acceleration of the particles with Lorentz factor $\gamma_c = 1/(1 - v^2/c^2)^{1/2} \sim 100$ in plasma shocks has been studied [10].

The plasma shocks are ubiquitous because any types of obstacles can induce disturbance in a high-speed plasma flow. When the disturbance grows in a time shorter than the time-scale of dissipation of flow energy, a shock can be formed. Some of astrophysical phenomena relevant to the high-speed plasma flows are shown in Fig. 1.1. Although there is an agreement that these astrophysical phenomena are relevant to high-speed plasma flow, the exact details still remain unclear. Hence, interaction of the high-speed plasma flows should be studied to understand the generation mechanism of the cosmic rays.

High-speed plasma flows form plasma shock waves of which structure is closely related to the generation of cosmic rays. The structure of the plasma shock waves depends on which process is dominant for dissipation. Hence, characteristics of the plasma shocks differ greatly in two cases; whether that is formed under *collisional* or *collision-less* condition. Binary collisions of neutral particles dominates the dissipation process of conventional shock waves in atmospheric air in which a part of the kinetic energy in the high-speed plasma flow is converted to random translational kinetic energy by the binary collisions. In collision-less condition, the kinetic energy is distributed not only to compression of plasma, heating, dissociation, excitation of particles but to magnetic field, and generation of electric field also. Then the dissipation process in collision-less plasma is considered to depend strongly on plasma parameters, which makes the dissipation mechanism complicated.

As has been introduced in this section, the interaction of high-speed plasma flows are not well-understood, although it is ubiquitous in the space.

1.2 Collisional and collision-less process in interacting high-speed plasma flows

High-speed plasma flows exist anywhere in the space. These plasma flows are accompanied by shock waves. However, the structure is not unique, which depends strongly on the parameters of interacting plasma [11].

In the air, a density disturbance propagates at a sound speed. Shocks are formed where the density disturbance steepened by a supersonic piston is balanced out by the dissipation due to viscosity of the fluid. When we use similarity parameter, we can say that shock waves can be formed in cases with Mach number $M = U/C_s > 1$, where U and C_s are the fluid velocity and the sound speed. Chemical reactions of gas particles should be considered in a condition of $M \gg 1$. For example, a strong and collisional plasma shock wave is formed in front of the space shuttle when it is reenter-

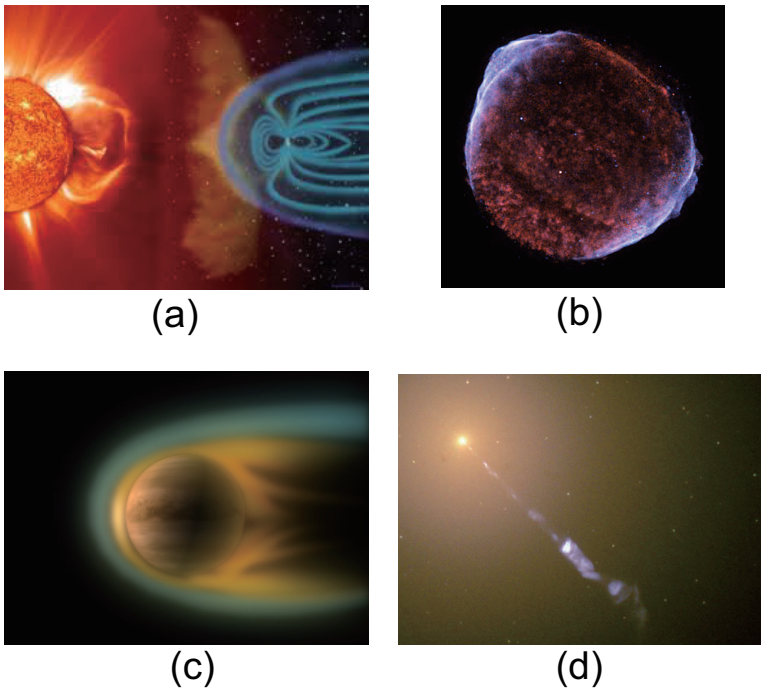

Figure 1.1: Astrophysical phenomena relevant to high-speed flow: (a)Interaction beween the solar wind and magnetosphere of the Earth [12]. (b)Supernova explosion (SN1006) [13]. (c)Escape of atmosphere on Venus [14]. (d) Active galactic nuclei jet from M87 [15].

ing the atmosphere at $M > 10$ [16]. The dissipation processes in the strong shock are accompanied by dissociation, excitation and ionization of atmospheric particles [17].

Mean free path λ of neutral particles determines the shock thickness because the viscosity is caused by momentum transfer through a few collisions of particles in the fluid. The mean free path of neutral particles is defined by:

$$\lambda = \frac{1}{\sigma n_n} \tag{1.1}$$

where σ and n_n are the cross section of collision and the number density.

The presence or the absence of binary collision between the particles characterizes the structure of plasma shock wave also. For example, the binary collision induces strong dissipation through the momentum transfer. In a collisional plasma condition, shock thickness, density and temperature transition scale, is determined basically by the mean free path of Coulomb collision between ions λ_{ii}. Then the transition time is considered to be an order of λ_{ii}/v_i.

The ion-ion mean free path λ_{ii} is described by:

$$\lambda_{ii} = \frac{(4\pi\epsilon_0)^2 m_i^2 v_i^4}{Z^4 e^4 n_i \ln\Lambda}, \tag{1.2}$$

where Z and e are the charge of ion and elementary charge, n_i, m_i and v_i are the ion density, mass of the ion and the ion velocity, and $\ln\Lambda$ and ϵ_0 are the Coulomb logarithm and permittivity in vacuum, respectively.

As shown with the equation above, decreasing the ion density increases the ion-ion mean free path $\lambda_{ii} \propto m_i^2 v_i^4/(Z n_i)$. Astrophysical shocks usually propagates in a low density medium. Observation with artificial satellite reveals that the transition scale of the astrophysical shocks is less than ion-ion mean free path λ_{ii}. Actually, the thickness of the astrophysical shocks, such as the bow shock near the earth and that in supernova remnants, were shorter than the mean free path of Coulomb collision [18]. This means the kinetic energy of the plasma flow is dissipated without the classical binary collision between ions. When the binary collision is neglected, charged particles in the plasma may interact to each other and form a shock waves through electric

and/or magnetic field. Those are called collision-less shocks and regarded as one of the origin of cosmic rays [19, 20]. In case with astrophysical plasma in collision-less condition, the plasmas satisfy the following condition:

$$\lambda_D, \;\; c/\omega_{pi} < \lambda_{ii} \tag{1.3}$$

where λ_D and c/ω_{pi} are Debye length and ion inertial length.

Fluid velocity is normalized by the ion acoustic velocity in unmagnetized plasmas, as follows:

$$M_i = \frac{U}{\sqrt{\gamma k_B (T_e + T_i)/m_i}} \tag{1.4}$$

where k_B, T_e, T_i, and m_i are the Boltzmann constant, electron and ion temperature, and mass of ion. In astrophysical plasma, electrostatic shock waves can be formed in a high-speed flow with the ion acoustic Mach number $M_i > 1$. Specific heat ratio γ can be assumed to be equal for ions and electrons if energy distribution to the internal degree of freedom of ions is negligible. The order of M_i can be estimated by $U/\sqrt{k_B T_e/m_i}$ because of higher electron temperature than ion temperature in general astrophysical plasma.

Meanwhile, electromagnetic shock waves can be formed in a flow with Alfvén Mach number $M_A > 1$. Alfvén Mach number is defined by:

$$M_A = \frac{U}{B/\sqrt{m_i n_i \mu_0}} \tag{1.5}$$

where B, n_i and μ_0 are magnetic field in the plasma flows, ion density and magnetic permeability in vacuum. As shown, the fluid velocity is normalized by the Alvén wave velocity for scaled magnetohydrodynamical experiments.

When the kinetic energy of the high-speed plasma flow exceeds the excitation energy of internal degree of ions, the kinetic energy is also distributed to the internal energy. Populations of specific atomic states relate the energy distribution in the internal degrees of freedom. Time evolution of the population can be described by a rate equation with rate coefficients of excitation, de-excitation, ionization and recom-

bination by electron impact and radiative processes. These rate coefficients depend on plasma temperature, density and ionization degree.

The kinetic energy of high-speed plasma flows is distributed to work for the compression, heating, dissociation, excitation, ion reflection and so on in the shock structure. The structure of collision-less shocks are determined depending on the plasma parameters and the relaxation processes in which a suddenly formed non-equilibrium state progresses to an equilibrium state without classical collision, i.e. dissipation processes through electric and/or magnetic field in the shock structure.

1.3 Approach to Astrophysical Phenomena with Laboratory Experiments

The dissipation process in the collision-less shocks is too complicated to make clear without experimental evidence. The discusion of the mechanism needs a parametric study of shocks. If the astrophysical phenomena can be reproduced in a scaled versions of the same process in a device with laboratory scale, the parametric study is much more advantageous than the measurements with satellites.

In past studies, most astronomers used the data from telescope and/or artificial satellites to measure the parameters of astrophysical plasma. Observation satellites can detect charged particles directly in plasmas near the Earth while it can not clarify the global image of astrophysical phenomena. In the meanwhile, for far astronomical objects, we can see global image of a phenomenon with light emission but that brings only a piece of qualitative information of the plasmas. Therefore, both quantitative value of the plasma parameters and the global image can not be measured simultaneously with conventional methods. Laboratory astrophysics experiments which can control the experimental condition and utilize various diagnostics, are useful for the parametric study.

Collision-less shocks, magnetic reconnection, and astrophysical jets have been studied for the past dozens of years. These phenomena play important roles in energy

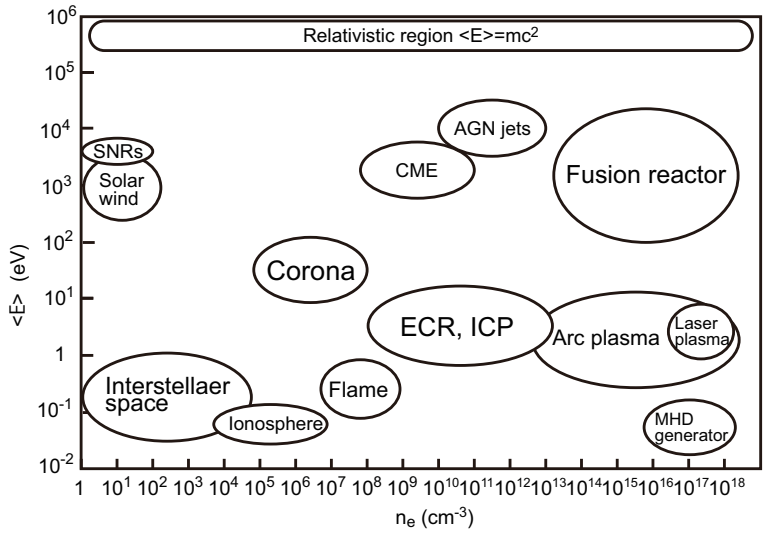

Figure 1.2: Typical parameter regions of electron density and averaged energy of space and laboratory plasmas.

transport and evolution of charged-particle distribution functions in astrophysical environments. Laboratory studies of collision-less shocks have been conducted since the 1960s [21]. Laboratory studies of not only collision-less shocks but also magnetic reconnection [22] were reported. However data obtained by those early studies were ambiguous and not reproducible. Recent development of pulse power devices enables us to make high-energy-density state of matter under a controllable and reproducible condition. The high-energy-density condition is advantageous to make extremely large pressure gradient and accelerates a plasma to a high speed region comparable with astrophysical phenomena [23].

Astrophysical plasmas have a wide range of parameters as mentioned in Sec. 1.1. The typical plasma parameters containing astrophysical plasmas are shown in Fig. 1.2. Needless to say, but the spacial and temporal scales of astrophysical plasma are extremely large compared with laboratory plasma. A huge astrophysical phenomenon could be reproduced in a laboratory scale device by adjusting the relevant scaling parameters such as Mach number, magnetic Reynolds number, Euler number and scale lengths normalized by the mean free path according to exploring physics [24] [25].

These scaling parameters are determined by the plasma parameters such as plasma velocity, density, temperature, and ion mass. In collision-less plasma, the scale of shock thickness becomes an order of Debye length λ_D or ion inertial length c/ω_{pi}. These scale lengths decrease with increasing of plasma density because $\lambda_D \propto \sqrt{T_e/n_e}$ and $c/\omega_{pi} \propto \sqrt{m_i/n_i}$. As shown by Eq. (1.2) and (1.5), the mean free path of ions is represented by $\lambda_{ii} \propto \frac{m_i^2 v_i^4}{Z^4 n_i}$ and the ion acoustic Mach number is $M_i \propto v_i/\sqrt{T_e/m_i}$. These scaling parameters are correlated each other through v_i and they can not be changed independently.

A controllable and well-defined plasma source is needed to perform the parametric study of the astrophysical phenomena. In previous studies, several types of plasma sources were used for laboratory astrophysics experiments. They are roughly divided into two types: a hydro-dynamic one and an electro-magnetic one.

The former are laser ablation plasma sources [26] [27]. In general, because the lasar produced plasma (LPP) is accelerated hydro-dynamically, the acceleration inevitably accompanies density and temperature decrease. Therefore, the plasma parameters of LPP can be controlled by the laser intensity at the focal spot and distance from the target.

The latters are discharge produced plasma sources. These devices accelerated the plasma directly by the magnetic pressure induced by the discharge current. This means the correlation of plasma parameters is expected to be weak compared with the simple hydrodynamic acceleration. Therefore, discharged plasma sources such as Magneto-Plasma-Dynamic (MPD) arc channels [28], plasma guns [29] [30] have been conventionally used to form high-speed plasma flows with larger scale length. Also, experiments were conducted both with Lasers and plasma guns [31] [32]. Pulse discharge devices such as coaxial plasma guns [33], z pinch devices [21], plasma focus devices [34] [35] and wire array discharge devices [36] [37] were constructed.

In case of the electro-magnetic acceleration using wire-arrayed implosion plasma [37], the initial plasma boundary is well controlled by the wire configuration and the pinching plasma can be high-speed and/or dense, depending on the shape of wire array. With MAGPIE device at Imperial College in London UK, a dense-high-speed

plasma flow was obtained with MA scale of fast rising discharge current [36]. Wire-arrayed Z-pinch discharges can generate the most dense plasma by the strong self-magnetic field. The z-pinch discharges are suitable for the formation of dense, high-speed plasma flow by the localized strong magnetic pressure. The plasmas in z-pinch and plasma focus devices are strongly magnetized in general because plasmas are directly driven by discharge current with the devices. Then we think that when initial geometry of the pinching plasma is well defined and magnetization can be controlled, the electro-magnetic force is useful for the acceleration and the compression of a bulk plasma in a controllable manner.

1.4 Purpose of study

The purpose of this study is to develop a device with which we can make interaction experiments of high-speed plasma flow in a well-defined condition. Based on the consideration described in the previous section, we have made an attempt to develop a table-top apparatus performing interaction experiments with well-defined high-Mach-number flows under controllable, reproducible, and repetitive condition.

We propose a new type of plasma source with tapered pinch discharge in a thin capillary to investigate the complicated dissipation processes arising in interacting high-speed plasma flow [38,39]. In the tapered pinch discharge scheme, a time evolving discharge current sheet forms a plasma jet in a capillary which has taper shape. The taper-pinched plasma was expected to be radially compressed and axially accelerated by the discharge current sheet. A high-Mach number flow is expected to be formed by the strong electro-magnetic force in a thin capillary filled with Argon gas which has low thermal speed. This also means possibility of construction of a compact device to form high-speed flows. The plasma parameters of the taper-pinched plasma are controlled by the pinching motion depending on discharge current, pre-filled gas density, and the taper geometry. Also the table-top apparatus expected to be able to make parametric studies easily due to its flexibility.

In the new type of plasma device, pre-ionizing plasma is pinched under a stational and uniform gas supply with differential pumping. Pre-ionization can prevent the pinching plasma from localization during the drive of main pulsed discharge current. Thus reproducible plasma flows is expected to be formed in this scheme. Also, this scheme is repetitive in comparison with wire-arrayed z-pinch discharges. The pinched plasma is extracted to a test chamber through a small aperture of electrode. The extracted plasma drifts and expands freely in the test chamber. Hence, well-defined plasma can be obtained in this experimental apparatus. The spacio-temporal scale of freely expanding plasma is cm-μsec in the test chamber. That is also advantageous for the experiments because we can apply well-established diagnostics to the plasma. For example, the acoustic Mach number and mean free path of high-speed plasma were estimated by the measurement of electron temperature with a Langmuir probe and average speed with a Faraday cup.

We will try to make an interaction experiment of high-speed plasma flows by counter-facing the tapered pinch plasma sources. Based on the experimental results, we will show that the taper-pinched plasma sources enable us to perform reproducible and controllable experiments in a wide range of astrophysical plasma parameters.

1.5 Scope and Outline of Thesis

The thesis started with a brief history of space exploration and an introduction of the influence of cosmic rays on human body. We showed examples of interacting high-speed plasma flows in terrestrial environment. First, we pointed out that the interactions of high-speed plasma flows; thereby the formation of the shock waves, the magnetic reconnection, and the cosmic rays generally exist in the space, and showed the background and motivation of this thesis. Indication of the importance of parametric study of the phenomena for laboratory astrophysics and a review of previous experimental studies followed the introduction. We described that the purpose of this study is to develop a device with which we can make controllable interac-

tion experiments of high-speed plasma flow relevant to astrophysics in a well-defined condition.

Chapter 2 describes overviews of the plasma shock waves, namely, the complicated structure and the dissipation processes in strong shock waves, and the scaling parameters for well-organized analysis. We also show past experimental approaches for the astrophysical phenomena and characteristics of the representative experimental apparatus.

Chapter 3 shows a new type of plasma source composed of a taper pinch capillary for the parametric study on the strong shock waves. We indicate that the tapered pinch plasma (TPP) can be controlled by pre-filled gas density in the capillary, the peak discharge current and the taper geometry.

Chapter 4 presents counter-streaming plasma experiments. We describe that we have constructed an experimental apparatus that can drive counter-streaming plasma flows formed by the tapered pinch discharge device. We show that the counter-streaming TPP device can provide a reproducible, controllable and well-defined interacting plasma with a wide parameter range of fluid velocity, plasma density and magnetization degree.

Chapter 5 explains and discusses the results obtained in this study. The explanation is connected to discussions of the interaction of high-speed plasma flows in collision-less condition. Results show enhancement of light emission, decrease of ion velocity, increase of ion density, and rise of electron temperature as signs indicating growing disturbance of the counter-streaming flow in the interacting region.

Finally, in Chapter 6, we summarize these results with a consideration on future contribution for the understanding of astrophysical phenomena and conclude this study. In conclusion, we will show that we have constructed experimental apparatus with TPP device which form a controllable, a well-defined and reproducible high-speed plasma flow for conducting the parametric study of laboratory astrophysics experiments.

Chapter 2

Laboratory Experiments on Shock Waves

2.1 Concept of laboratory astrophysics

Astrophysical data are inherently limited. A satellite can get information of astrophysical plasmas in the solar system by direct measurement of electro-magnetic field and/or velocity distribution of charged particles in its own scale length and time. While it is difficult for the satellite to measure plasma parameters of far astrophysical objects and phenomena having extremely high temperature, we can evaluate the light emission from the astrophysical plasma with a telescope. The light emission from a plasma contains valuable information to estimate its parameters of the astrophysical plasmas and global structure of it. In general, shifted and/or broaden line emissions due to Doppler effect and Stark effect from the plasmas give us useful information relating to plasma velocity, density and temperature.

However, direct measurements of the local plasma parameters using artificial satellites and imaging of the global structure of astrophysical plasmas with telescopes can not be carried out simultaneously. As an approach to study unclear mechanisms of the phenomena, not only observation using satellites and numerical simulation, but laboratory astrophysics has attracted great attention also, because imaging, spectroscopic

and probe measurements are available simultaneously with repeatable, controllable and diagnosable manner in laboratory plasmas.

Needless to say, but the plasma parameters of astrophysical phenomena can not be controlled. In contrast, laboratory plasmas can be controlled by experimental parameters. In collisional and weak shock regions, elastic scattering due to binary collisions of neutral particles and/or ion-ion interaction dominate the dissipation process. The dissipation process becomes complex with increase of shock strength. Hence the dissipation process depends on the plasma parameters in the upstream region of shock front. A parametric study is required for understanding the complex dissipation mechanism. A controllable plasma source is needed to perform the parametric study of astrophysical phenomena using the scaling law.

The laboratory plasmas must satisfy a scaling law to reproduce the astrophysical phenomena in the device. The scaling parameters are represented by normalized physical parameters, and dimensionless temporal and spatial scales. Target of physical interest for the astrophysics determines the relevant non-dimensional parameters for scaled laboratory experiments. For example, acoustic Mach number is one of the representative scaling parameters. Fluid velocity is normalized by ion acoustic wave velocity as the acoustic Mach number, which is regarded as a critical parameter for the formation of electrostatic shocks.

In past studies, several types of plasma sources such as lasers, MPD arc jets and z-pinch devices were used for laboratory astrophysics experiments. We propose a new type of discharge produced plasma as a controllable and well-defined plasma source that is suitable for the laboratory experiments.

2.2 Plasma shock waves

2.2.1 Rankin-Hugoniot relation

The plasma which underwent the shock waves is compressed and heated. When we consider 1 dimensional coordinate system shown in Fig. 2.1(b), conservation of

mass, momentum, and energy across the shock front can be expressed as follows:

$$\rho_u v_u = \rho_d v_d = Q, \tag{2.1}$$

$$Qv + p_u = Qv_d + p_d, \tag{2.2}$$

$$\frac{1}{2}v_u^2 + h_u = \frac{1}{2}v_d^2 + h_d, \tag{2.3}$$

with ρ, v, Q, p and h are the ion density, the plasma velocity, the momentum density, the pressure, and the enthalpy. Subscript u and d show upstream and downstream of the shock front. Because ions have most of momentum and mass, the equations sometimes describe only about ions.

Assuming the plasma is ideal gas, the enthalpy is given as:

$$h = C_p T = \frac{\gamma p}{(\gamma - 1)\rho}, \quad \gamma = C_P/C_V \tag{2.4}$$

where γ is the specific heat ratio. From Eqs. (2.1) and (2.2), we get the following relations:

$$p_d - p_u = Q^2 \left(\frac{1}{\rho_u} - \frac{1}{\rho_d} \right). \tag{2.5}$$

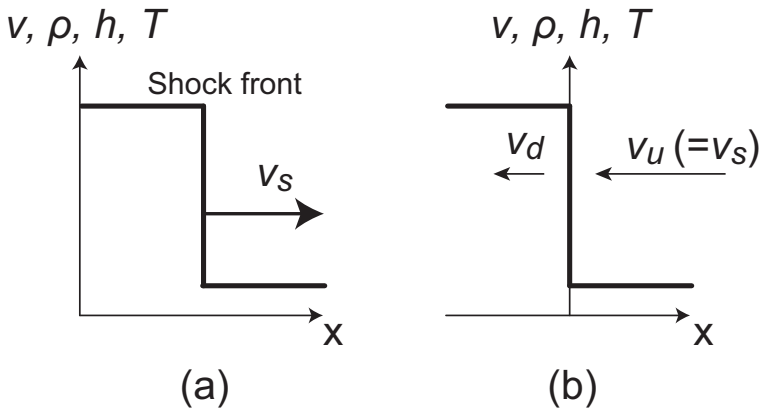

Figure 2.1: A schematic view of the shock wave in observer rest frame (a) and shock rest frame (b).

Employing the definition of upstream Mach number $M_u = v_u/C_{s,u}$, where $C_s = (\gamma p/\rho)^{1/2}$, the following Rayleigh's relation:

$$\frac{p_d}{p_u} - 1 = \gamma M_u^2 \left(1 - \frac{\rho_u}{\rho_d}\right) \tag{2.6}$$

is obtained.

Assuming a perfect gas, from the Rayleigh's relation and equations (2.3) and (2.4), we have the following relation:

$$\left(\frac{p_d}{p_u} + \frac{\gamma - 1}{\gamma + 1}\right)\left(\frac{\rho_u}{\rho_d} - \frac{\gamma - 1}{\gamma + 1}\right) = \frac{4\gamma}{(\gamma + 1)^2} \tag{2.7}$$

between upstream and downstream of the shock layer. Then the following equations of plasma velocity, density, pressure and temperature between upstream and downstream of the shock:

$$\frac{v_d}{v_u} = \frac{\rho_u}{\rho_d} = 1 - \frac{2(M_u^2 - 1)}{(\gamma + 1)M_u^2}, \tag{2.8}$$

$$\frac{p_d}{p_u} = 1 + \frac{2\gamma}{\gamma + 1}(M_u^2 - 1), \tag{2.9}$$

$$\frac{T_d}{T_u} = \frac{C_{s_d}}{C_{s_u}} = 1 + \frac{2(\gamma - 1)(\gamma M_u^2 + 1)(M_u^2 - 1)}{(\gamma + 1)^2 M_u^2}, \tag{2.10}$$

$$M_d^2 = 1 - \frac{(\gamma + 1)(M_u^2 - 1)}{2\gamma M_u^2 - (\gamma - 1)} \tag{2.11}$$

are the Rankin-Hugoniot relations for 1-D ideal gas flow. As shown above, hydrodynamic equations for an ideal fluid allow the existence of discontinuous solutions describing shock waves.

2.2.2 Electrostatic shocks

In the front of electrostatic shock, when the plasma density gradient exists, an ambipolar electric field may be induced by different mobilities between of ions and

electrons. The equation of motion is described by:

$$mn\left[\frac{\partial \mathbf{v}}{\partial t} + (\mathbf{v}\cdot\nabla\mathbf{v})\right] = q_s nE - \nabla p - m_s\nu\mathbf{v}, \tag{2.12}$$

where subscript s shows the particle species and ν is collision frequency of particle s.

In steady state, we obtain the following equation from Eq. (2.12)

$$v = \frac{q_s}{m_s\nu}\mathbf{E} - \frac{k_B T_s}{m_s\nu}\frac{\nabla n}{n} \tag{2.13}$$

We set the mobility μ_s and the diffusion coefficient D_s as follows:

$$\mu_s \equiv |q_s|/m_s\nu, \quad D_s \equiv k_B T_s/m_s\nu \tag{2.14}$$

Employing these definition, we have a flux $\mathbf{\Gamma_s}$ of particle "s" as follows:

$$\mathbf{\Gamma_s} = n\mathbf{v_s} = \pm\mu_s n\mathbf{E} - D_s\nabla n \tag{2.15}$$

Assuming $\mathbf{\Gamma_i} = \mathbf{\Gamma_e} = \mathbf{\Gamma}$, ambipolar electric field may be written by:

$$\begin{aligned} \mathbf{\Gamma} &= \mu_i n\mathbf{E} - D_i\nabla n = \mu_e n\mathbf{E} - D_e\nabla n \\ \mathbf{E} &= \frac{D_i - D_e}{\mu_i - \mu_e}\frac{\nabla n}{n}. \end{aligned} \tag{2.16}$$

Then the shock downstream region tends to have a positive potential relative to the upstream region.

We consider a potential hump formed like a schematic view shown in Fig. 2.2. The relation of ion velocities in upstream and downstream of the shock is described by:

$$v_d = (v_u^2 - \frac{2e\phi}{m_i})^{1/2}, \tag{2.17}$$

where ϕ is the potential in the shock wave. Therefore, by using Eq. (2.17) and the mass conservation law, we get:

$$n_d = \frac{n_u v_u}{v_d} = n_u \left(1 - \frac{2e\phi}{m_i v_u^2}\right)^{-1/2}, \tag{2.18}$$

where $n_{u,d} = \rho_{u,d}/m_i$. In the present configuration, poisson equation is described using Eqs. (2.17), (2.18) and Boltzmann's relation by:

$$\frac{\mathrm{d}^2\phi}{\mathrm{d}x^2} = \frac{e}{\epsilon_0}(n_{ed} - n_d) = \frac{e}{\epsilon_0} n_u \left[\exp\left(\frac{e\phi}{k_B T_e}\right) - \left(1 - \frac{2e\phi}{m_i v_u^2}\right)^{-1/2}\right]. \tag{2.19}$$

Therefore, we obtain the following expression for the electric potential:

$$\frac{\mathrm{d}^2\psi}{\mathrm{d}\xi^2} = \mathrm{e}^{\psi} - \left(1 - \frac{2\psi}{M_i^2}\right)^{-1/2} \equiv -\frac{dV(\psi)}{d\psi}, \tag{2.20}$$

where

$$\psi = \frac{e\phi}{k_B T_e}, \quad \xi = \frac{x}{\lambda_D}, \quad \lambda_D = \left(\frac{\epsilon_0 k_B T_e}{n_u e^2}\right)^{1/2}, \quad M_i = \frac{v_u}{(k_B T_{e,u}/m_i)^{1/2}} \tag{2.21}$$

and $V(\psi)$ in Eq. (2.20) is called *Sagdeev potential* [40].

Integrating Eq. (2.20) under condition of $V(\phi) = 0$ at $\psi = 0$, we have:

$$V(\psi) = 1 - \mathrm{e}^{\psi} + M_i^2 \left[1 - \left(1 - \frac{2\psi}{M_i^2}\right)^{1/2}\right] \tag{2.22}$$

for the *Sagdeev potential*. Pseudo particles that represented by ψ dissipate their energy in the *Sagdeev potential* as schematically shown in Fig. 2.2.

Assuming the reflecting number density of ions to be Δn_i, we have the following equation:

$$\psi = \frac{1}{n_u} \int_0^{\xi} (n_e - n_d + \Delta n_i) \mathrm{d}\xi. \tag{2.23}$$

That indicates the potential ϕ decreases with reducing of ion density in the downstream region. Also this means that ion reflection dominates the dissipation process in the electrostatic plasma shock.

Lower limit of the Mach number M_i for the potential formation is derived by the Taylor developing of Eq. (2.22) as follows:

$$
\begin{aligned}
&1 - \mathrm{e}^{\psi} + M_i^2 \left[1 - \left(1 - \frac{2\psi}{M_i^2} \right)^{1/2} \right] \\
&\quad = 1 - \left(1 + \psi + \frac{\psi^2}{2} + \cdots \right) + M_i^2 \left(1 - \frac{1}{2} \left(\frac{2}{M_i^2} \right) \psi - \frac{1}{4} \left(\frac{2}{M_i^2} \right)^2 \frac{\psi^2}{2} \cdots \right) \\
&\frac{1}{2}\psi^2 - (\psi^2 / 2M_i^2) > 0 \quad M_i > 1. \qquad (2.24)
\end{aligned}
$$

Increasing Mach number increases reflected ions. Then the electrostatic potential also increases, while the incoming ions to the shock layer decrease. When reflected ions equal to incoming ions, it is indicated that the shock structure is unstable [41] [42]. To form electrostatic potential in front of shock, $V(\psi) = 0$ must exists in $\psi > 0$. Thus, upper limit of the Mach number is obtained as follows:

$$
\exp(M_i/2) - 1 < M_i^2 \quad M_i < 1.6. \qquad (2.25)
$$

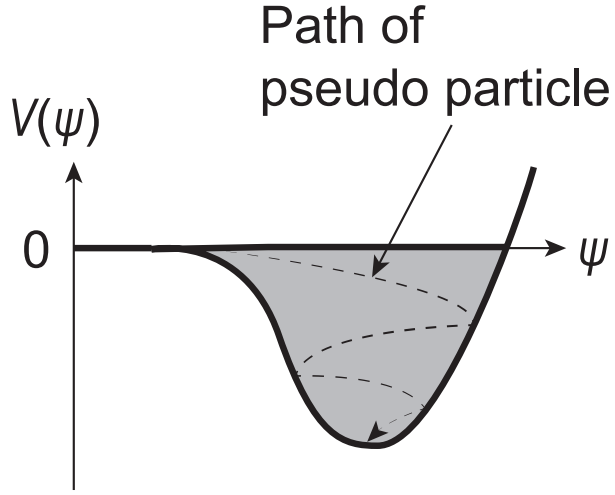

Figure 2.2: A schematic view of Sagdeev potential.

These equations indicate that the simplified model predicts that the electrostatic shock wave can exist in $1 < M_i < 1.6$.

The ion acoustic Mach number changes the shock structure. In 1970-1980s, a double plasma device was used for study of collision-less electrostatic shocks. It was indicated that in a case of $M_i < 1.6$, the thickness of collision-less shocks became an order of Debye length [43]. When a strong ion reflection occurs, the thickness can be more than 10 times Debye length [44]. In fact, the electrostatic shocks can have a few hundred times Debye length of pre-shock structure due to the reflection of ions. Existence of electrostatic shocks at higher Mach number was confirmed by observation with satellite and discussed by PIC simulations [45] [41]. In a region of flow with $M_i \sim 10 - 100$, such as a flow in supernova remnants (SNRs), the electrostatic shocks are considered to have the pre-shock structure with length from an order of ion inertial length c/ω_{pi} to 1000 times of Debye length, where ω_{pi} is ion plasma frequency described by:

$$\omega_{pi} = \sqrt{\frac{n_i e^2}{\epsilon_0 m_i}}. \tag{2.26}$$

The thickness of electromagnetic shocks is predicted to be an order of ion inertial length. As the shock formation time is determined by the dissipation process of ion energy, the time scale is predicted to be from ω_e^{-1} to ω_{pi}^{-1} [41] depending on the acoustic Mach number. However, the exact structure of shock wave remains unclarified.

2.2.3 Electro-magnetic shocks

Ideal MHD (Magneto-Hydro-Dynamic) equations have three types of waves; shear Alfvén wave, fast, and slow mode magneto-sonic waves. The conservation equations [46] for electro-magnetic shocks on x-y plane are described by:

$$\rho v_{x_d} = \rho_u v_{x_u} \tag{2.27}$$

$$\rho v_{x_d}^2 + p_d + \frac{B_{y_d}^2}{2\mu_0} = \rho_u v_{x_u}^2 + p_u + \frac{B_{y_u}^2}{2\mu_0} \tag{2.28}$$

$$\rho_d v_{x_d} v_{y_d} + \frac{B_{y_d} B_{x_d}}{\mu_0} = \frac{B_{y_u} B_{x_u}}{\mu_0} \tag{2.29}$$

$$\begin{aligned} &\frac{1}{2}\rho_d v_{x_d}(v_{x_d}^2 + v_{y_d}^2) + \frac{\gamma}{\gamma-1} p_d v_{x_d} \\ &+\frac{1}{\mu_0}\left(-v_{y_d} B_{y_d} B_{x_d} + v_{x_d} B_{y_d}^2\right) = \frac{1}{2}\rho_u v_{x_u}^3 + \frac{\gamma}{\gamma-1} p_u v_{x_u} + \frac{1}{\mu_0} v_{x_u} B_{y_u}^2 \end{aligned} \tag{2.30}$$

$$B_{x_d} = B_{x_u} \tag{2.31}$$

$$v_{x_d} B_{y_d} - v_{y_d} B_{x_d} = v_{x_u} B_{y_u}, \tag{2.32}$$

where B and μ_0 are the magnetic field and magnetic permeability in vacuum. Subscripts d and u denote downstream and upstream of the shock front. Subscript y shows normal direction for x which the shock waves travels along.

Employing the conservation equations, we obtain the following equation:

$$\begin{aligned} (v_u^2 - X v_{A_u}^2)^2 \{ X c_{s_u}^2 &+ \frac{1}{2} v_u^2 \cos^2\theta [X(\gamma-1) - (\gamma+1)]\} \\ &+\frac{1}{2} v_{A_u}^2 v_u^2 \sin\theta X \{[\gamma + X(2-\gamma)] v_u^2 \\ &-X v_{A_u}[(\gamma+1) - X(\gamma-1)]\} = 0 \end{aligned} \tag{2.33}$$

where θ is the angle of the magnetic field line from the shock normal in the upstream and $X = \rho_d/\rho_u$.

Then we have the following Rankin-Hugoniot equations for MHD shocks from Eq. (2.33):

$$\frac{v_{x_d}}{v_{x_u}} = \frac{1}{X}, \tag{2.34}$$

$$\frac{v_{y_d}}{v_{y_u}} = \frac{v_u^2 - v_{A_u}^2}{v_u^2 - X v_{A_u}^2}, \tag{2.35}$$

$$\frac{B_{x_d}}{B_{x_u}} = 1, \tag{2.36}$$

$$\frac{B_{y_d}}{B_{y_u}} = \frac{(v_u^2 - v_{A_u}^2) X}{v_u^2 - X v_{A_u}^2}, \tag{2.37}$$

$$\frac{p_d}{p_u} = X + \frac{(\gamma-1) X v_u^2}{2 c_{s_u}} \left(1 - \frac{v_d^2}{v_u^2}\right). \tag{2.38}$$

Here, we set the coordinate which the flow line and the magnetic field line are parallel, thus $v_{y_u}/v_{x_u} = B_{y_u}/B_{x_u}$ [47].

In electro-magnetic shocks, the Alfvén Mach number is the index of the dissipation process of kinetic energy of the plasma flow. In a fast mode shock, a phase of magnetic pressure is the same with the plasma pressure. On the other hand, in a slow mode shocks, the magnetic pressure decreases with increase of the plasma pressure. The slow shock is regarded to play an important role for relaxation process of magnetic energy in magnetic reconnection [48, 49].

2.3 Atomic processes

The basic atomic processes of plasma are categorized to: excitation, ionization, deexcitation, recombination, and radiation [50]. Figure 2.3 shows an illustration of the atomic processes existing in a plasma. When the shock wave becomes strong and radiation effect cannot be ignored, the structure of the shock can be modified by the radiation heating in the upstream and cooling in the downstream.

In a plasma in thermodynamic equilibrium, parameters such as particle density, velocity distribution and the populations of excited ions formulated by the temperature, determine the plasma condition. The ratio of the number density of ions in two

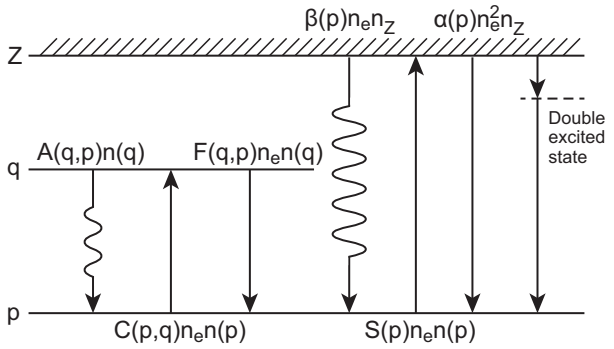

Figure 2.3: A schematic of atomic processes in a plasma.

different energy levels is given by Boltzmann distribution:

$$\frac{n'_p}{n_p} = \frac{g'_p}{g_p} \exp\left[-\frac{E_{p'p}}{k_B T_e}\right], \tag{2.39}$$

where we have assumed levels $p < p'$ in an arbitrary ionization stage, $g_j = 2J + 1$ is statistical weight, and $E_{p'p}$ is the energy gap from p' to p levels. The multiplicity of the energy level j is determined by the quantum number for angular momentum J.

In a non-equilibrium plasma, a change in the population of discrete levels is brought about by spontaneous, stimulated transition of radiations and transitions induced by electron impact. For example, the temporal development of the population in level p in ionization stage $(z-1)$, $n(p)_{z-1}$, can be described by the following rate equation [51] with collisional radiative model:

$$\begin{aligned}
\frac{\partial n_p^{(z-1)}}{\partial t} + \nabla(n_p^{(z-1)} \cdot \mathbf{v}) \;=\; & \sum_{q<p} C_{q,p} n_e n_q \\
& - \left[\left\{ \sum_{q<p} F_{q,p} + \sum_{q>p} C_{p,q} + S_p \right\} n_e + \sum_{q<p} A_{p,q} \right] n_p \\
& + \sum_{q>p} [F_{q,p} n_e + A_{q,p}] n_q \\
& + [\alpha_p n_e + \beta_p] n_e n_z,
\end{aligned} \tag{2.40}$$

where C, F, S, α, and β show the rate coefficient for excitation, deexcitation and ionization by electron impact, three-body recombination, and radiative recombination.

2.4 Dissipation and relaxation processes in shock waves

In collisional shocks, a part of the kinetic energy of supersonic flow is converted to the thermal energy in the downstream through binary collisions. The shock structure maintains a stable state by a balance between the steepening of compression wave by adiabatic compression and the thermal dissipation. In the shock transition layer, the fluid dissipates its kinetic energy as a function of shock strength; i.e., the shock Mach

number, with increasing entropy ΔS:

$$\begin{aligned}\Delta S = S_d - S_u &= C_v \ln\left[\frac{p_d}{p_u}\left(\frac{\rho_u}{\rho_d}\right)^{\gamma}\right] \\ &= C_v \ln\left\{\left[1+\frac{2\gamma}{\gamma+1}(M_u^2-1)\right]\left[\frac{(\gamma-1)M_u^2+2}{(\gamma+1)M_u^2}\right]^{\gamma}\right\}, \quad (2.41)\end{aligned}$$

where subscript d and u denote downstream and upstream of the shock front.

The effect of relaxation appears in cases of rapid heating and cooling. Through the relaxation process, the kinetic energy of the fluid can be distributed to the internal degrees of freedom. For example, a fluid composed of diatomic molecular gas has multiple degrees of freedom; translational, two rotational, and one vibrational motions. In the shock wave, sometimes the structure is affected by the relaxation effect of them as schematically shown in Fig. 2.4. The temperature and the density reach T_2' and ρ_2' transiently before coming to the final equilibrium state [52]. In general, the relaxation times t_1^* for translational and rotational degrees are much shorter than the time for vibration t_2^*. The difference of these relaxation times is due to characteristic energy levels. Rotational levels of diatomic molecules have typically ~ 0.01 eV of energy gaps and those of vibration energy are ~ 0.1 eV. The relaxation times are determined by energy gaps together with collision frequency. For particles of average velocity $\bar{v}$, the relaxation time t^* is represented by:

$$t^* = \frac{\alpha}{\sigma n \bar{v}} \quad (2.42)$$

where α is a factor of proportionality that depends on the degree of freedom and σ is the cross section.

If the kinetic energy is comparable to the ionization energy of species consisting the fluid, the energy is also distributed into excitation of electronic levels and ionization of atoms. When we take into account of the transfer of kinetic energy to the internal degrees of freedom such as excitation, ionization and also radiation, the equation for conservation of energy can be described as follows:

$$Q\left[\frac{1}{2}v^2+\frac{5}{2}R(T_i+\alpha T_e)+\frac{1}{n_i}\sum_{j=1}^{m}n_i^{j+}RE^{j+}\right] \\ +F_{rad}+v(p_{rad}+\varepsilon_{rad})+F_{cond} \;=\; E(x), \tag{2.43}$$

where α is the degree of ionization, R is the gas constant: $R = k_B/m_i$, m_i is the ion atomic mass, m is the maximum charge state, n_i^{j+} is number density of charge state $j+$, E^{j+} is equal to ionization energy divided by k_B, F_{rad} is the radiation flux, p_{rad} is the radiation pressure, ε_{rad} is radiation energy density, F_{cond} is the heat conduction flux by ions and electrons, and $E(x)$ is total energy flux in a position x.

The relaxation between the internal degrees of freedom affects the plasma shock structure [53]. In a collisional plasma shock wave, the ion temperature rises faster than the electron temperature across the shock front as illustrated in Fig. 2.5. Subsequently, the temperatures of ions and electrons are relaxed to an equilibrium state. A simplified expression for the time evolution may be written by:

$$\frac{dT_i}{dt} = -\frac{T_i - T_e}{\tau_{ie}} \tag{2.44}$$

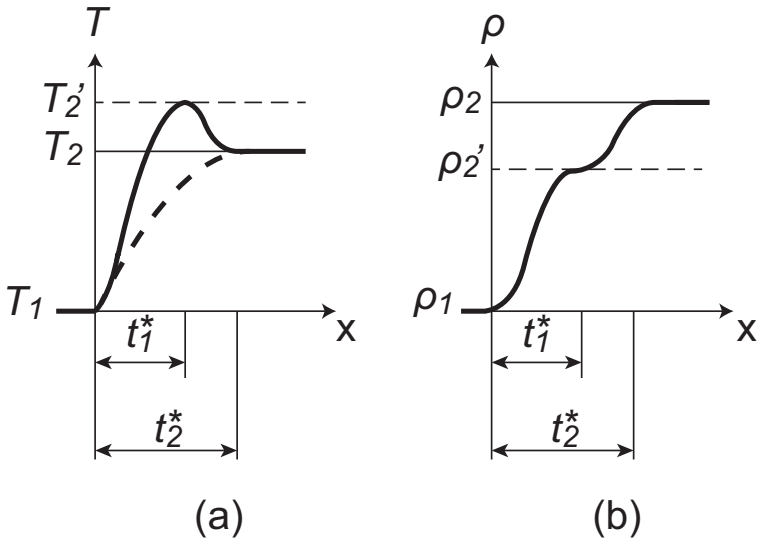

Figure 2.4: Example of relaxation layer; typical temperature (a) and density (b) profiles in a transition layer of shock heated diatomic gas [52].

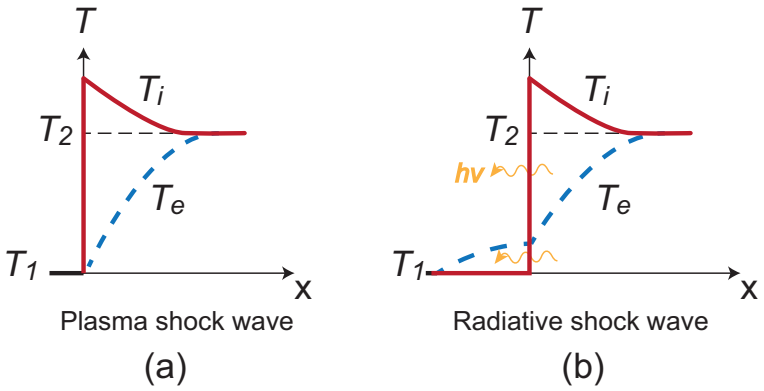

Figure 2.5: Temperature distributions in shock transition layer without (a) with (b) radiative effect.

where τ_{ie} is the ion-electron collisional relaxation time.

In collision-less plasma shocks in high-speed plasma flow, binary collision between ions and/or neutral particles can be neglected and the fast moving ions in background electrons have basically two types of unstable mode; ion-ion instability and ion-electron instability. In the transition layer, a part of the kinetic energy of the ions drifting super-sonically is expected to be dissipated by the instability [54].

When the non-equilibrium state induced by the instabilities relaxes to a final state in which multiple degrees of freedom exist, the structure of transition layer is complex and difficult to predict. That is the reason why parametric study is needed to well-understand the dissipation process of collision-less shocks.

2.5 Similarity and scaling laws

Non-dimensional parameters such as the Mach number and the Reynolds number are used for making scaled magneto-hydrodynamical experiments, that represent the important properties of phenomena. The *scaled experiments* intend to represent primary physical characteristics using a laboratory device with a scaled down device. For example, the ion acoustic Mach number represents compressibility in a non-magnetized plasma. Also, the Mach number is principal scaling parameter of a supersonic flow which characterizes compressibility of the fluid. In a magnetized

plasma, the Alfvén Mach number characterizes compressibility of the magnetic field lines. Those dimensionless parameters represent similarity of phenomena with different plasma parameters.

An astrophysical phenomenum is expected to be reproduced in a laboratory plasma when the relevant scaling parameters are identical. Table 2.1 shows typical values of parameters of astrophysical plasma relevant to high-speed plasma and a sample of required parameters to laboratory plasma.

The solar wind consists mainly of hydrogen ions and electrons with $T_e \sim 10$ eV, and fluid velocity of 450 km/s at near the Earth. Then, the ion acoustic Mach number $M_i = U/\sqrt{k_B T_e/m_i}$ is ~ 10. This means if we can make Argon plasma flow, with $T_e \sim 1$ eV, and $U \sim 20$ km/s, we can discuss the effect of compressibility on the shock formation process with similar level in the solar wind by the laboratory plasma according to the scaling law.

In low speed fluid mechanics in which viscosity plays a significant role, the Reynolds number is used to support the predictability of similar flow patterns in a different fluid flow situation. In case of plasma, magnetic Reynolds number is utilized for the prediction of flow pattern and diffusion of magnetic field. Employing magnetic diffusion equation derived from the Maxwell equations, we can show the

Table 2.1: Physical and scaling parameters of astrophysical phenomena and laboratory plasma

Parameters	Solar wind [55]	Supernova [18]	AGN jet [56]	Laboratory plasma
Ion species	H	H	H	Ar
Plasma density (cm^{-3})	7	∼1-100	$\sim 10^{10} - 10^{13}$	$\sim 10^{13}$
Plasma speed (km/s)	450	400-1000	2000	~ 10
Temperature (eV)	∼10	$\sim 10^3$	$\sim 10^3$	∼1
Magnetic field (nT)	∼7	∼1	-	-
Acoustic Mach number	∼15	$\sim 10^2$-10^3	200	~ 10
R_{e_m}	2×10^9	$\sim 10^7 - 10^8$	$\sim 10^3 - 10^4$	∼10
$c/\omega_{pi}/\lambda_{ii}$	$\sim 10^{-11}$	$\sim 10^{-12}$	$\sim 10^{-9}$	$\sim 10^{-3}$

following induction equation:

$$\frac{\partial B}{\partial t} = \nabla \times (\mathbf{v} \times \mathbf{B}) + \frac{\eta}{\mu_0} \Delta \mathbf{B}, \tag{2.45}$$

where the first and the second terms show convection and diffusion of the magnetic field, respectively. The Reynolds number R_{e_m} is defined by:

$$\frac{|\nabla \times (\mathbf{v} \times \mathbf{B})|}{|\Delta \mathbf{B}(\eta/\mu_0)|} \sim \frac{vB/L}{(B/L^2)(\eta/\mu_0)} = \frac{\mu_0 v L}{\eta} \equiv R_{e_m}, \tag{2.46}$$

where L is scale length of the plasma.

As shown with Eq.(2.46), R_{e_m} is presented by the ratio of magnetic diffusion time $\tau_R = \mu_0 L^2/\eta$ and Alfvén transit time $\tau_H = L/v_A$ ($v \sim v_A$). That also shows for a MHD plasma with $R_{e_m} \ll 1$, magnetic field is governed by diffusion equation. On the other hand, for $R_{e_m} \gg 1$ the magnetic field lines are frozen in the plasma.

In general, the formation time of collision-less shock is order of inverse of ion plasma frequency ω_{pi}. For formation of shock wave, the interaction time of charged particles in laboratory plasma should be enough longer than the formation time of a shock wave under collision-less condition.

A schematic of a Coulomb interaction process is illustrated in Fig. 2.6, where the Coulomb force is deflecting an electron by an angle θ. In case of plasma, the cross section for 90 deg scattering σ is defined by an impact parameter r_0 which can affect impulse $F\Delta t$ corresponding to all of the momentum loss of electron. Under the

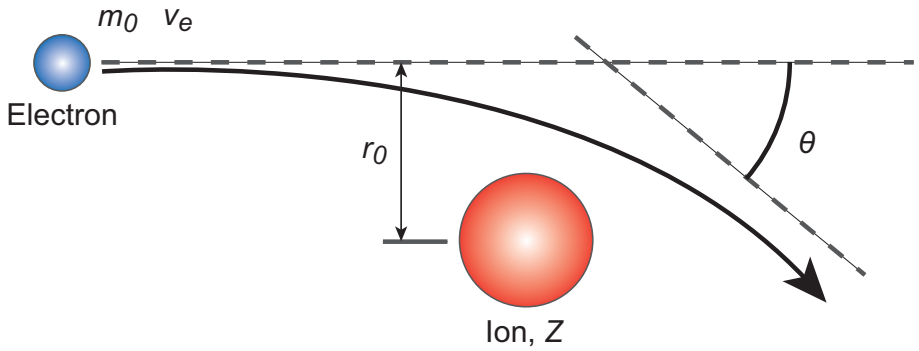

Figure 2.6: Schematic of an electron orbit by Coulomb interaction.

condition, F and δt are described as follows:

$$F = \frac{1}{4\pi\epsilon_0}\frac{Ze^2}{r_0^2}, \quad \Delta t = r_0/v_e \tag{2.47}$$

where ϵ_0, Z and e are electric permittivity in vacuum, ionization degree of ion and elemental charge, respectively. The momentum loss can be described as:

$$\Delta(m_e v_e) \sim (m_e v_e) = F\Delta t = \frac{Ze^2}{4\pi\epsilon_0 r_0^2}\frac{r_0}{r_0 v_e}, \tag{2.48}$$

where m_e is the mass of electron.

Then, the impact parameter for the θ=90 degree scattering of electron by an ion is described by:

$$r_0 = \frac{1}{4\pi\epsilon_0}\frac{Ze^2}{k_B T_e}, \tag{2.49}$$

where $v_e = \sqrt{k_B T_e/m_e}$.

In the collisional plasma, the deflection is actually an accumulation of multiple scatterings. Therefore, we should consider the effect of small angle scattering by introducing Coulomb logarithm $\ln\Lambda = \ln(r_0/\lambda_D)$ [57].

We can estimate the mean free path in a strongly ionized plasma by $\lambda = 1/(\sigma n)$ with $\sigma = \pi r_0^2$. Thus, the mean free path between ions and electrons can be described by:

$$\lambda_{ei} = \frac{(4\pi\epsilon_0)^2 (k_B T_e)^2}{\pi Z^2 e^4 n_i \ln\Lambda}, \tag{2.50}$$

where n_i is ion density, and $\ln\Lambda$ and ϵ_0 are the Coulomb logarithm.

Collision time between a particle moving in a plasma with a velocity v, with a mass m and a charge q in the plasma and a particle having a charge q^*, a mass m^*, a density n^* and a velocity $v_T^* = \sqrt{k_B T^*/m^*}$ is described by:

$$\tau = \frac{4\pi\epsilon_0^2 m m_r v^3}{q^2 q^{*2} n^* \ln\Lambda}, \tag{2.51}$$

where we assume $v > v_T^*$ and $m_r = mm^*/(m+m^*)$ is the reduced mass.

A criterion of collision-less condition can be described by $\tau_{ii}\omega_{pi} \gg 1$. Collision times of electron-ion τ_{ei}, ion-ion τ_{ii}, electron-electron τ_{ee}, and ion-electron τ_{ie} can be compared with the following equations:

$$(electron - ion): \quad \tau_{ei} = \frac{4\pi\epsilon_0^2 m_e^2 v_e^3}{Z^2 e^4 n_i \ln\Lambda} \tag{2.52}$$

$$(ion - ion): \quad \tau_{ii} = \frac{2\pi\epsilon_0^2 m_i^2 v_i^3}{Z^4 e^4 n_i \ln\Lambda} \tag{2.53}$$

$$(electron - electron): \quad \tau_{ee} = \frac{2\pi\epsilon_0^2 m_e^2 v_e^3}{e^4 n_e \ln\Lambda} \tag{2.54}$$

$$(ion - electron): \quad \tau_{ie} = \frac{m_i}{m_e}\frac{4\pi\epsilon_0^2 m_e^2 v_i^3}{Z^2 e^4 n_e \ln\Lambda}. \tag{2.55}$$

Hence for a plasma with $Z = 1$, $n_i = n_e$, and $v_i = v_e$, those are indicating $\tau_{ii} \sim m_i/m_e \cdot \tau_{ie} \sim (m_i/m_e)^2 \cdot \tau_{ei} \sim (m_i/m_e)^2 \cdot \tau_{ee}$.

2.6 Previous experiment for astrophysics

Several types of plasma source were used for laboratory astrophysics experiments. In general, it is difficult to obtain a dense, high-speed bulk plasma flows. In the previous experiments, a huge gradient of plasma kinetic and/or magnetic pressure was needed to accelerate bulk plasma to the astrophysical level. However, recent progresses of intense laser and fast pulse power technology have changed the situation. Ablation plasma made by intense laser and electromagnetic pulse driven by fast pulse discharges can make high-energy-density state to form the pressure gradient. Here, we describe representative devices for the high-speed plasma source.

2.6.1 Intense laser facility

Recently, plasma flows which have ∼1000 km/s of velocity was obtained by high power laser facilities such as Gekko XII in Osaka University, Japan, Omega in USA, LULI in France [27]. In general, the high speed laser produced plasma (LPP) is formed by focusing a high power laser at a local spot on a solid target in vacuum. The lasers can form high-energy-density plasma through heating of electrons in a local area of

the solid target. Then a high-speed plasma can be accelerated hydro-dynamically from a hot-dense; high-energy-density, plasma.

Assuming isentropic process, we have the maximum flow speed as follows:

$$\begin{aligned} h_0 &= C_p T_0 = C_p T_1 + \frac{v_1^2}{2}, \\ v_{max} &\sim \sqrt{2C_p T_0} = \sqrt{\frac{2}{\gamma+1}\gamma R T_0} = \sqrt{\frac{2}{\gamma+1}} C_{s_0}, \end{aligned} \tag{2.56}$$

where h, C_p, T, and C_s are the enthalpy, the specific heat at constant pressure, the temperature, and the sound speed. Subscript 0 and 1 show the stagnated high-energy-density state and a state with motion, respectively. As indicated by Eq. (2.56), the maximum velocity of particles v_{max} is limited by the sound speed at the stagnated state with temperature T_0.

In addition, the free expansion process is uncontrollable, that is, decreasing of plasma density is inevitable for forming a high-speed flow. Namely, in case of the hydro-dynamical acceleration, heating up and consecutive expansion processes are inevitable for making the high-speed flow, in which the density and the flow speed are gas-dynamically correlated.

In addition high-speed plasma flows made by LPP have a short life time for the plasma interaction. As shown in the previous section, inverse of ion plasma frequency $\omega_{pi}^{-1} \propto \sqrt{m_i/n_i}$ is predicted to be the characteristic time for the formation of electrostatic shocks. Then the life time of interacting plasma should be longer than the

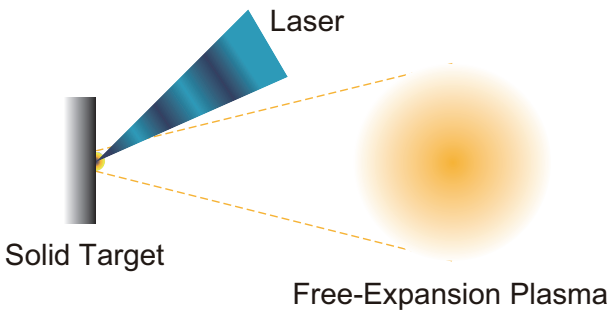

Figure 2.7: A schematic of laser produced plasma.

characteristic time. The scale length of LPP extends with decreasing plasma density. As the interaction time of LPP and formation time of shock wave depend on plasma density, the diagnostics of interacting plasma is difficult to make. For example, probe measurements are difficult to apply to highly transient plasma flow. Because, available interaction region of LPP is very small both in space and time.

2.6.2 Pulsed discharge device

Fast pulse power is suitable for forming high-speed plasmas in a limited space of a cylindrical chamber. When the rise time of discharge current is faster than the diffusion of electro-magnetic wave, a localized current sheet is formed in the pulsed discharge device. The Z machine at Sandia is known as the largest pulsed power device in the world [58]. The large facility, which contains vacuum magnetically insulated transmission lines 4 m diameter, can drive a discharge current of 20 MA in a pulse-shaping mode from 100 ns to 300 ns. Also, this scheme can provide experimental data which is useful for analysis of astrophysical x-ray sources [59].

In the fast discharge device, the current sheet plays as a piston in the plasma and forms a shock wave. In 1960's, collision-less shocks were observed in high temperature plasma for the first time with z-pinch discharge in the laboratory scale [21]. An experiment was also performed with theta-pinch discharge [61]. Figure 2.9 shows schematic diagrams of dynamics of z-pinch and theta-pinch discharge. These scheme are similar to each other, however, z-pinch discharge can make more dense-high-speed

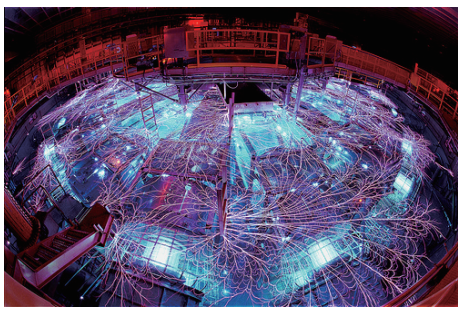

Figure 2.8: Photograph of the Z-machine [60].

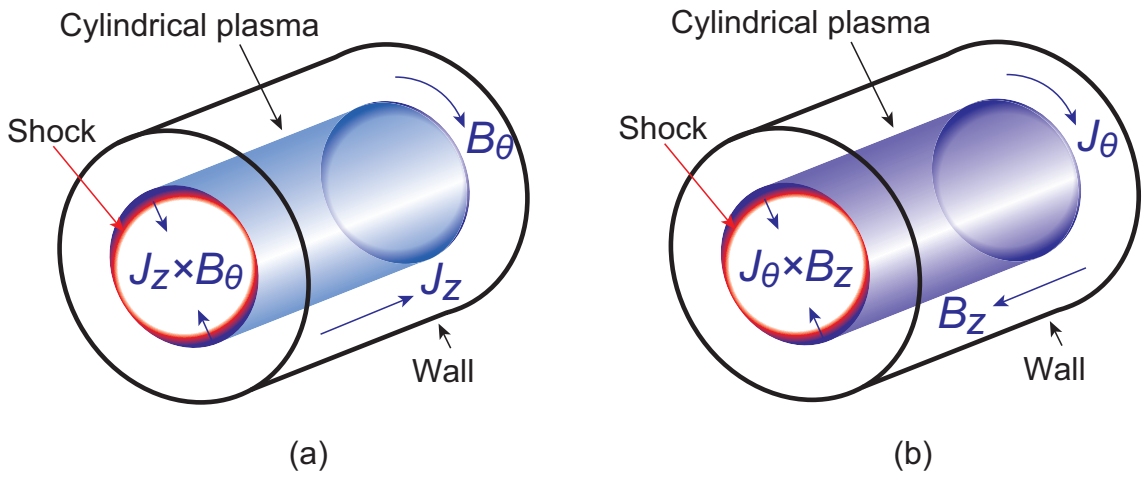

Figure 2.9: Formation of high-energy-density plasma using z-inch (a) and theta-pinch (b) device.

plasma than theta-pinch discharge because B_θ becomes strong with decrease of the plasma radius. They observed the shock waves are driven by the piston of discharge current sheet. However, the method needs a large scale chamber including implosion phase (a few ten cm in diameter and $\sim$ 1 m in length) to avoid the effect of shock reflection. The density in the chamber is limited in a range where formation of uniform discharge is possible in a gas. Therefore a large number of capacitors is needed to accelerate large size plasma for a time scale with diagnosable length in this scheme.

A.D. Craig [33, 62] attempted experiments of collision-less shocks without background magnetic field using a piston driven by a discharge current sheet shown in Fig. 2.10. Probe measurements were carried out for the evaluation of high-speed plasma flow. However, due to weak magnetic field change, it was difficult to distinguish magnetic fields of the background plasma and the piston plasma [33].

The plasma focus and z-pinch devices are representative pulsed discharge devices. The plasma focus device consists of two coaxial electrodes as shown in Fig. 2.11. The discharge current sheet axially accelerates the gas in the device.

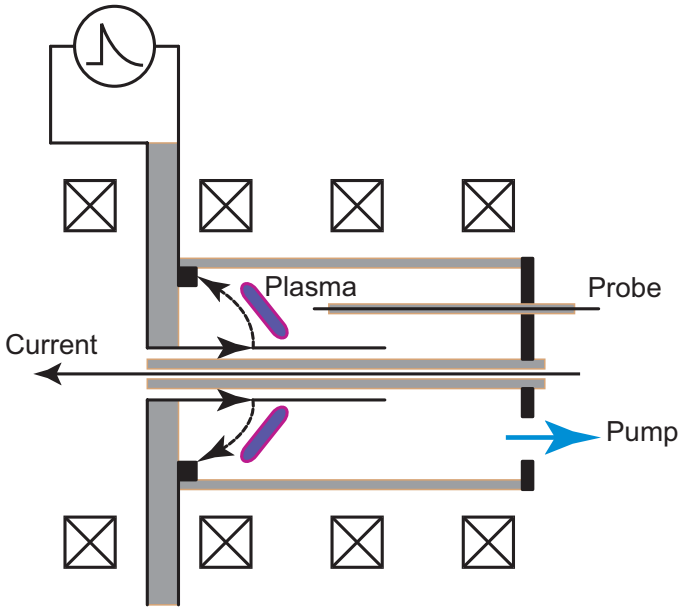

Figure 2.10: Formation of high-speed flow using plasma focus device.

The equation of motion of the current sheet in the acceleration phase of plasma focus can be described by:

$$m(z)\frac{\mathrm{d}^2 z}{\mathrm{d}t^2} = \frac{I^2}{2}\frac{\mathrm{d}L(z)}{\mathrm{d}z}, \tag{2.57}$$

$$I = -C_0\frac{\mathrm{d}U}{\mathrm{d}t}, \tag{2.58}$$

$$\frac{\mathrm{d}(LI)}{\mathrm{d}t} = U, \tag{2.59}$$

where $m(z)$, C_0, and U are the mass of the current sheet, the capacitance, and the voltage between electrodes. The effective inductance L increases due to the extension of discharge current path with time. At last, pinching of the current sheet at the top of center electrode forms a dense high temperature plasma. In the z-pinch device and the implosion phase of the plasma focus device, the Lorentz force strongly depends on the plasma radius, because the magnetic pressure can be $B^2/2\mu_0 \approx I^2/(8\pi\mu_0 r^2)$. However, intensive pinching normally causes collaps of the plasma with instabilities. This means reproducibility is the critical issue of the pinching device.

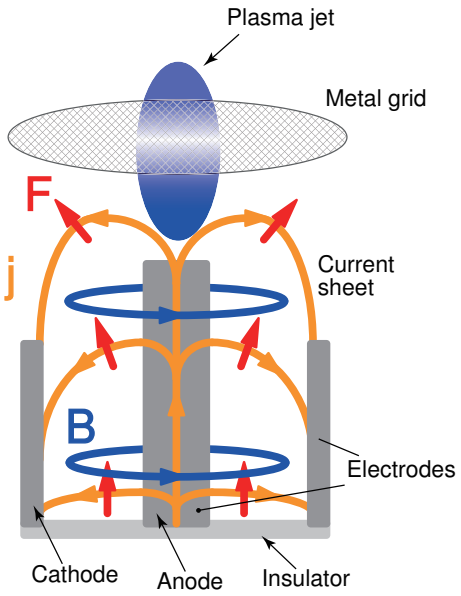

Figure 2.11: A schematic of plasma focus device.

When a plasma is accelerated by the Lorentz force, current can be induced in the plasma. S. Minami et al. attempted to simulate dynamic behavior of the Earth's magnetosphere with a coaxial plasma gun [29, 30]. However reproducibility can not be obtained enough, because the current sheet was driven under the gas pressure of 10^{-5} Torr in the experimental chamber. In an experiment with the plasma focus [34], a metal grid was used to cut the induced current and magnetic field in the moving plasma.

Plasma sources having large stored energy and low capability of repetitive operation are not so suitable for the parametric study. It seems to be needed device utilizing direct acceleration by the Lorenz force and relatively heavy ion species to form high-speed plasma flows without large storage energy. We expect that gas discharges without large capacitance can realize easily repetitive operation and good reproducibility. However, a means to strongly accelerate plasma at lower peak discharge current due to low stored energy is needed. Therefore, we consider that it is needed to divide a high-speed plasma driven by discharge current sheet and a well-defined unmagnetized low-density plasma to form electrostatic shock.

2.7 Summary

In this chapter, we showed the concept and the importance of laboratory experiments for astrophysics. We explained that the structure of astrophysical shock wave depends on the plasma parameters. We indicated importance of *similarity* and well-designed *scaling* for the laboratory experiments in which complex and unclear shock structure can be discussed quantitatively over a wide range of normalized parameters. We showed that for the scaled experiments to reproduce astrophysical shock waves, a controllable and well-defined plasma source should be established.

After a brief introduction of previous attempts to the laboratory astrophysics, we indicated that well-controlled laboratory experiment is important for parametric study of the unknown mechanism in the shock waves. We pointed out an electromagnetically accelerated plasma is advantageous to make a controllable high-speed plasma flow. We also stressed the need for a controllable, a reproducible, a well-defined plasma with gas discharge devices.

Chapter 3

Plasma Source with Tapered Pinch Discharge

3.1 Concept of tapered pinch discharge

As has been explained in the previous chapter, we need a controllable and well-defined plasma source for performing scaled astrophysical experiments in a laboratory. Electromagnetic acceleration based on discharged plasma scheme is considered to be suitable for controlling the plasma flows. Because plasmas can be accelerated without hydrodynamic expansion, the velocity of electro-magnetically accelerated plasma can be almost independent of plasma density and temperature.

Among the discharged plasma devices, z-pinch devices have been used to make dense, high-temperature plasmas aiming to high energy density studies such as x-ray light sources and nuclear fusion devices. We proposed a new type of plasma source with a small, thin, and tapered shape capillary which can compress not only radially but accelerate a plasma axially by the z-pinch effects. We call that type of Z-pinch plasma source as tapered pinch plasma (TPP).

In z-pinch device, the maximum plasma density can be controlled by the temporal profiles of magnetic pressure induced by the discharge current. The tapered pinch plasma is expected to be able to control the plasma velocity and the plasma density

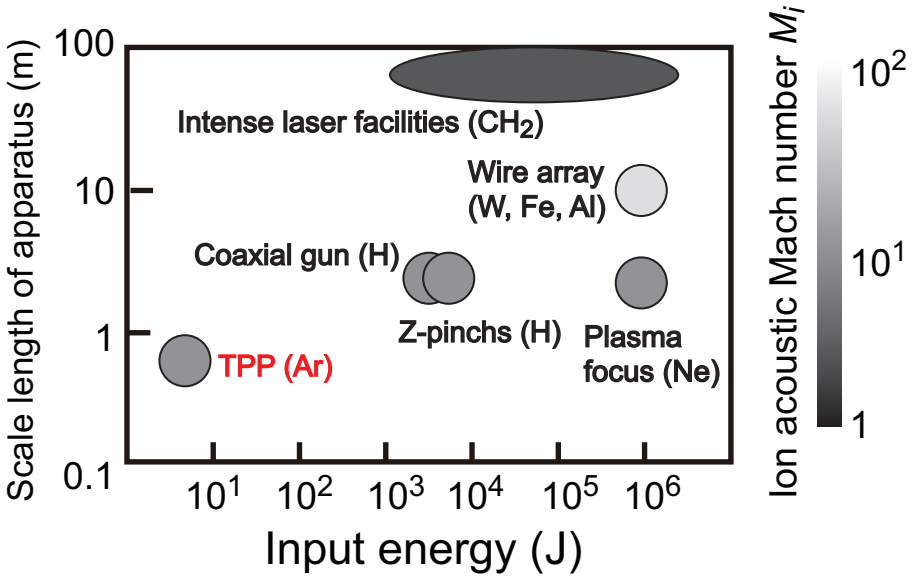

Figure 3.1: Typical plasma parameters of taper pinched plasma device and those of previous works. Ion species typically used in the devices are shown in parentheses.

independently. Hence, TPP is considered to be suitable for the parametric study of laboratory astrophysics.

Parameter regions of our apparatus and previous works were shown in Fig. 3.1. Various ion species were used for formation of high-speed flows. We constructed a compact device to make high-Mach number plasma flow with a thin capillary rather than huge, energetic devices in previous studies. As shown in the figure, TPP can make a high-speed plasma flow of equipment Mach number level with compact pulsed power device which can be driven less than one hundredth of input energy. The tapered pinch plasma source can be much more repetitive and reproducible than the other plasma source in virtue of the compactness. Moreover, the TPP can form unmagnetized plasma easily in comparison with conventional z-pinchs, θ-pinchs, and coaxial plasma guns. Therefore we can apply well-established diagnostics to the plasma by virtue of the moderate spacio-temporal scale of cm-μsec in a test chamber.

3.1.1 Z-pinches

Z-pinch utilizes radial implosion of a cylindrical or an annular plasma under the influence of a strong magnetic field produced by a current flowing in thin layer along the length of plasma [63]. When a balace between the current density distributions and the radial pressure profile in a Z-pinch is considered, the pressure balance is described by:

$$\frac{\mathrm{d}p}{\mathrm{d}r} = -J_z B_\theta, \tag{3.1}$$

where J_z and B_θ are axial current density and magnetic field in angular direction. Employing the axial component of Ampére's law, we have:

$$\frac{1}{r}\frac{\mathrm{d}}{\mathrm{d}r}(rB_\theta) = \mu_0 J_z \tag{3.2}$$

and by integration of Eq. (3.2), we obtain:

$$B_\theta = \frac{\mu_0}{r}\int_0^r J_z r\mathrm{d}r = \frac{\mu_0}{2\pi r}\int_0^r 2\pi J_z r\mathrm{d}r. \tag{3.3}$$

The ion line density N_{li} is defined by:

$$N_{li} = \int_0^a 2\pi n_i r\mathrm{d}r \tag{3.4}$$

where a is the plasma radius. Taking the mean electron and ion temperature to be T_e and T_i, respectively, we can write:

$$N_{li}k_B(ZT_e + T_i) = \int_0^a 2\pi p r\mathrm{d}r, \tag{3.5}$$

where Z is ionization degree. Employing equations (3.1)and (3.3), we have the *Bennett relation*:

$$8\pi N_{li}k_B(ZT_e + T_i) = \mu_0\left(\int_0^a 2\pi J_z r\mathrm{d}r\right)^2 \tag{3.6}$$

for stationary plasma. That indicates small radius is advantageous for confinement of high-energy density plasma.

3.1.2 Snow-plow model for fast pinching plasma

In a capillary, if the skin depth δ shown below is smaller than its radius, a localized current sheet is expected to be formed along the capillary wall:

$$\delta = \sqrt{\frac{\eta\tau}{\mu_0\pi}}, \tag{3.7}$$

where η, τ are resistivity of the plasma in the capillary and the discharge period, respectively. When we assume the resistivity of plasma is described by the Spitzer formula [40], we can use the following equation:

$$\eta(\Omega \cdot m) = \frac{Z\pi e^2 m_e^{1/2} \ln\Lambda}{(4\pi\epsilon_0)^2 (k_B T_e)^{3/2}}. \tag{3.8}$$

In the dynamic phase of fast pinching plasma, the current sheet is driven inward by the magnetic pressure against the inner kinetic pressure of pinching plasma. As the piston at radius $r(t)$ moves radially inwards due to the pinch effect, all the plasma or the filled gas is assumed to be swept up and accumulated ahead of the skin layer like a *snow-plow*.

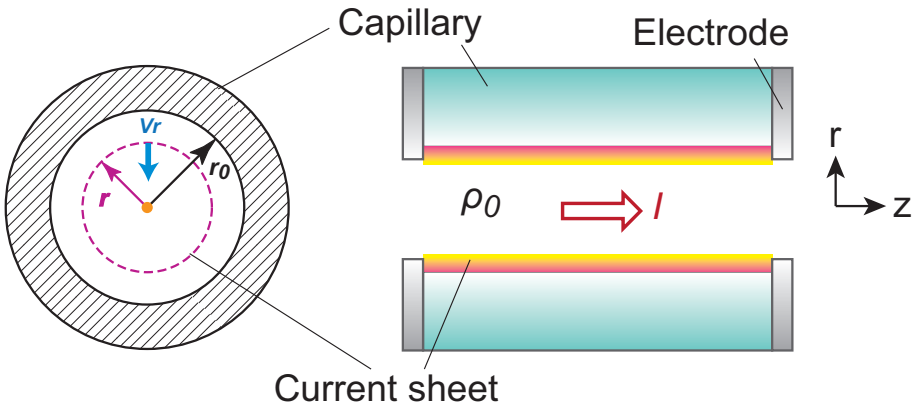

Figure 3.2: Schematic of snow-plow model in a z-pinch discharge device.

The mass of the layer is therefore continuously increasing, and the momentum equation per unit length for the imploding layer is given by:

$$\frac{d}{dt}\left[\rho_0\pi(r_o^2-r^2)\frac{dr}{dt}\right] = -\frac{\mu_0 I^2(t)}{4\pi r} + 2\pi r P_0\left(\frac{r_0}{r}\right)^{2\gamma}, \tag{3.9}$$

where ρ_0, P_0, r_0 and r are the initial gas density filled in the tapered capillary, the initial pressure, the initial radius of current sheet and the radius of pinching plasma, respectively. The specific heat ratio γ during the compression is usually assumed to be 5/3 for simplicity.

Introducing an assumption of adiabatic compression we have $2\pi r P_0(\frac{r_0}{r})^{2\gamma}$ as the pressure that makes calculation of the pinching dynamics possible with Eq. (3.9). However, strictly speaking, the snow-plow model does not conserve energy after maximum pinching, and so is only applicable to a phase of Z-pinch process in which the magnetic pressure can exceed thermal pressure during the implosion. It therefore might be applicable to argon or xenon discharges where the kinetic energy per ion is comparable to or less than the ionization potential.

3.1.3 Zipper effect

"Zipper effect" is called phenomena that plasma column propagating along the pinch axis of z-pinch devices [64, 65]. With the capillary that has a tapered shape, the current sheet can be also sequentially pinched along the symmetry axis in a controllable manner.

We can introduce a condition in which pressure gradient in the axial direction maintains $\frac{\partial}{\partial z}\left(\frac{B^2}{2\mu_0}\right) < 0$ by the tapered capillary because the magnetic pressure is a function of the radius of discharge current sheet. Then, if the geometry is rationally designed, the current sheet in the tapered capillary not only radially compresses and but axially accelerates the plasma also as shown schematically in Fig. 3.3. In a past study, this scheme was used to accelerate an argon plasma by a fast pulse power generator which drove a load current of 80 kA with a pulse width of 70 ns [66].

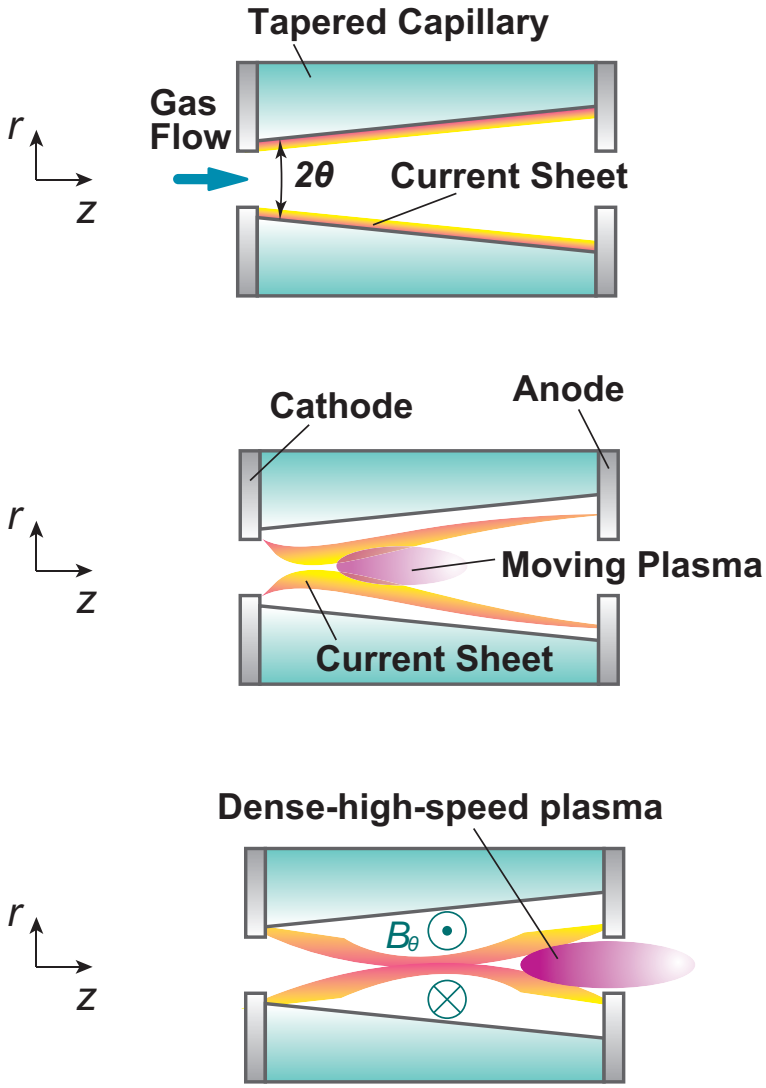

Figure 3.3: Concept of plasma formation and acceleration with tapered pinch discharge.

The taper angle is expected to affect the plasma parameters. However, it is difficult to predict the plasma velocity from the dynamics of the current sheet in the tapered capillary. Canto et al. [67] described a mechanism for the production of interstellar jets with the convergence of supersonic conical flows like the dynamics of the tapered pinch. The dynamics of jet formation was discussed using an analytical formation, however it was under an assumption of steady state in the shock interaction region. In the model by Canto, when the angle of the conical shock α satisfies $\tan\alpha = \sqrt{(\gamma-1)/(\gamma+1)}$ and the angle of convergent flows θ_c, we have jet velocity v_j:

$$v_j = \frac{v_0 \sin(\theta_c + \alpha)}{\cos(\alpha)}. \tag{3.10}$$

This equation shows that v_j is dependent on θ_c and the steller jet can not be accelerated larger than initial flow velocity v_0 in the steady state condition.

3.2 Experimental setup

3.2.1 Behavior of pinching plasma

First, we determined a discharge current waveform to drive the high speed plasma flow.

The motion of current sheet is expected to be that illustrated in Fig. 3.3, if the skin depth is less than the scale length of tapered capillary with radius of a few mm. In the parameter region of our experiment, the value of resistivity η was estimated to be $1.6 \times 10^{-4}\ \Omega \cdot \mathrm{m}$ from Eq. (3.3) with $Z = 1$, ion density $n_i = 10^{22}\ \mathrm{m}^{-3}$ and $T_e = 1$ eV. The skin depth in the capillary plasma was estimated to be $\sim$1 mm using Eqs. (3.7) and (3.8) with $\tau = 400$ ns.

We determined the requirement for peak discharge current from maximum radial velocity of the pinching current sheet. The maximum radial velocity is estimated by numerical integration of Eq. (3.9) with 4th order of Runge-Kutta method. The

equations modified from Eq. (3.9) for the Runge-Kutta method are

$$\frac{dv}{dt}(r,v,t) = 2\pi r\frac{\rho_0 v^2 - P_m + P_p}{\pi\rho(r_0^2 - r^2)}, \tag{3.11}$$

$$\frac{dr}{dt}(r,v,t) = v, \tag{3.12}$$

$$P_m(r,t) = \frac{\mu_0 I^2(t)}{4\pi r}, \tag{3.13}$$

$$P_p(r,t) = 2\pi r P_0 \left(\frac{r_0}{r}\right)^{2\gamma}, \tag{3.14}$$

where P_m and P_p are the magnetic pressure and plasma pressure, respectively. Then, temporal profile of the velocity and radius of the current sheet are obtained by iteration of the following calculation:

$$t_{i+1} = t_i + \Delta t, \quad v_{i+1} = v_i + k_v, \quad r_{i+1} = r_i + k_r,$$
$$k_{r,v} = \frac{1}{6}(k_{0_{r,v}} + 2k_{1_{r,v}} + 2k_{2_{r,v}} + k_{3_{r,v}}),$$

where $k_{0_{r,v}}$, $k_{1_{r,v}}$, $k_{2_{r,v}}$, $k_{2_{r,v}}$ are as follows:

$$\begin{aligned}
k_{0_v} &= \Delta t\frac{dv}{dt}(t_i, r_i, v_i), \quad k_{0_r} = \Delta t\frac{dr}{dt}(t_i, r_i, v_i) \\
k_{1_v} &= \Delta t\frac{dv}{dt}(t_i + \frac{\Delta t}{2}, r_i, v_i + \frac{k_{0_v}}{2}), \quad k_{1_r} = \Delta t\frac{dr}{dt}(t_i + \frac{\Delta t}{2}, r_i + \frac{k_{0_r}}{2}, v_i) \\
k_{2_v} &= \Delta t\frac{dv}{dt}(t_i + \frac{\Delta t}{2}, r_i, v_i + \frac{k_{1_v}}{2}), \quad k_{2_r} = \Delta t\frac{dr}{dt}(t_i + \frac{\Delta t}{2}, r_i + \frac{k_{1_v}}{2}, v_i) \\
k_{3_v} &= \Delta t\frac{dv}{dt}(t_i + \Delta t, r_i, v_i + k_{2_v}), \quad k_{3_r} = \Delta t\frac{dr}{dt}(t_i + \Delta t, r_i + k_{2_v}, v_i).
\end{aligned}$$

Here, we set the time interval Δt to be 10^{-12} s. The discharge current assumed to be $I(t) = I_0 \sin(\omega t)$ in the simulation.

Figure 3.4 shows the time evolution of plasma radius and radial velocity of the discharge current sheet. The radial velocity was changed steeply near the central axis due to the increase of magnetic pressure which is determined by P_m. As the behavior of the discharge current sheet is incorrect after maximum pinching, we stopped the simulation at r =10 μm. We can estimate that, in a condition of I_0=10 kA and τ= 400 ns, the radial velocity reaches 59 km/s at 0.17 mm in radius from the result.

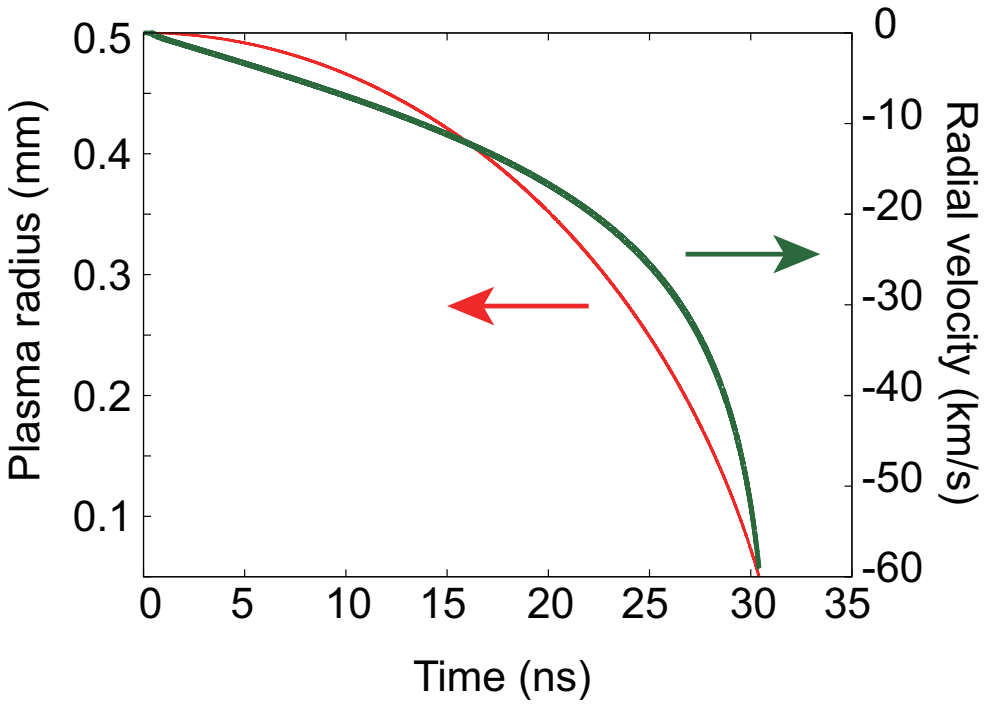

Figure 3.4: A result of snow-plow simulation of the behavior of discharge current sheet. The pre-filled gas density is 2.4×10^{-6} g/cm^3 , the peak discharge current is 10 kA, and the period is 400 ns.

We ignored the axial motion of the tapered pinch plasma and estimated roughly the axial velocity of plasma from the 1D simulation. Axial velocity of the plasma is predicted to be slightly lower than the maximum radial velocity in acceleration with tapered pinch discharge. As illustrated in Fig. 3.4, we expected to obtain high-speed plasma flows with U ∼10km/s, with discharge current of ∼ 10 kA at peak and 400 ns period. As the ion acoustic velocity of Argon plasma is estimated to be ∼ 1 km/s at $T_e \sim 1$ eV, we can expect to form a M_i ∼10 flow with the discharge condition.

3.2.2 Design of pulsed power driver

Next, we considered the discharge circuit to obtain the required current waveform. As higher peak current was expected to be desirable to form higher energy density plasma, we designed the pulse power device so as to drive the current as high as possible. Also, we aimed to design a compact device in contrast to previous

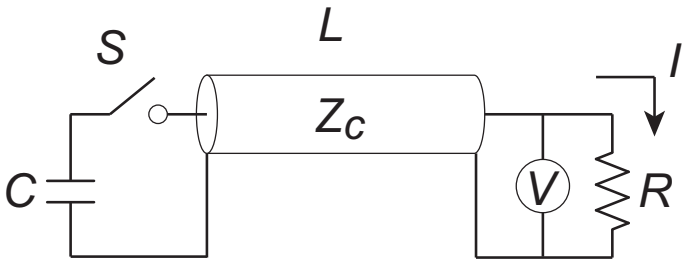

Figure 3.5: Schematic of transmission line model.

experimental devices as has been mentioned in Sec. 2.6.2 because compact device is suitable for the compression and the acceleration with magnetic pressure $P_m = \frac{\mu_0 I^2}{2\pi r^2}$.

In general, when the transmission length of electromagnetic wave is longar than wavelength of the current waveform, a distributed transmission line model must be used [68]. In a distributed transmission line model with impedance Z_c, a part of the electromagnetic wave through the transmission line reflects at the load R. The reflection coefficient of voltage ρ_v and current ρ_i are described by:

$$\rho_v = \frac{V_r}{V_i} = \frac{R - Z_c}{R + Z_c}, \quad \rho_i = \frac{I_r}{I_i} = \frac{Z_c - R}{R + Z_c} = -\rho_v \tag{3.15}$$

where V_r, V_i, I_r, and I_i are voltages and currents of the reflection and the incident wave. The impedance Z_c is needed to be as close to the load as possible, that is, to minimize the reflection. The plasma impedance is generally quite low. Then the driver impedance should be as small as possible.

On the other hand, when the transmission line is shorter than the wavelength of the current waveform, we can use a circuit model composed of electrical elements lump. Hence the discharge current waveform can be described by a circuit model; the inductance L, the capacitance C, and the resistance R as shown in Fig. 3.6.

The LCR circuit equation is described by:

$$V_0 = RI + L\frac{dI}{dt}L + \frac{1}{C}\int I dt, \tag{3.16}$$

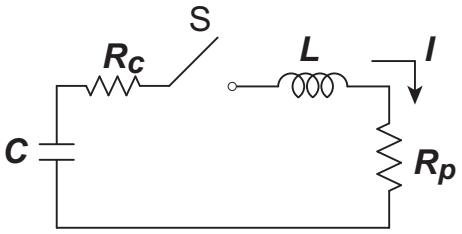

Figure 3.6: Schematic of LCR circuit.

where V_0 and I are voltage charged to the capacitor and the discharge current. The resistance R is consisted of internal resistance of the circuit R_c and load resistance R_p.

For $\frac{1}{LC} > \left(\frac{R}{2L}\right)^2$, the solution of Eq. (3.16) is

$$I(t) = \frac{V_0}{Z_c\sqrt{1-\zeta}} \mathrm{e}^{-\alpha t} \sin(\omega_0\sqrt{1-\zeta^2}t), \tag{3.17}$$

$$Z_c = \sqrt{\frac{L}{C} - \left(\frac{R}{2}\right)^2}, \tag{3.18}$$

$$\omega_0 = \sqrt{\frac{1}{LC}}, \tag{3.19}$$

$$\zeta = \frac{\alpha}{\omega_0} = \frac{R}{2}\sqrt{\frac{C}{L}}, \tag{3.20}$$

where Z_c is the impedance of the circuit. In general, we can assume $\zeta \ll 1$ and $\sqrt{L/C} \gg R$ because the resistivity of the capillary plasma is order of 0.1-0.01 Ω. Hence, the peak discharge current and period can be described as follows:

$$I_p \sim V_0/Z_c \sim V_o\sqrt{\frac{C}{L}}, \quad \tau = \pi/\omega_0 = \pi\sqrt{LC}. \tag{3.21}$$

3.2.3 Specification of pulsed power driver

For the discharge devices, we can determine the inductance L and the capacitance C of the circuit with $\omega_0 = 1/\sqrt{LC}$ and $Z_c \sim \sqrt{L/C}$. However it is difficult to construct the discharge circuit with low impedance $Z_c < 0.1$ Ω [69]. We designed a discharge circuit with circuit impedance $Z_c \sim 1$ Ω and period of the current $\tau \sim 400$ ns. To deal

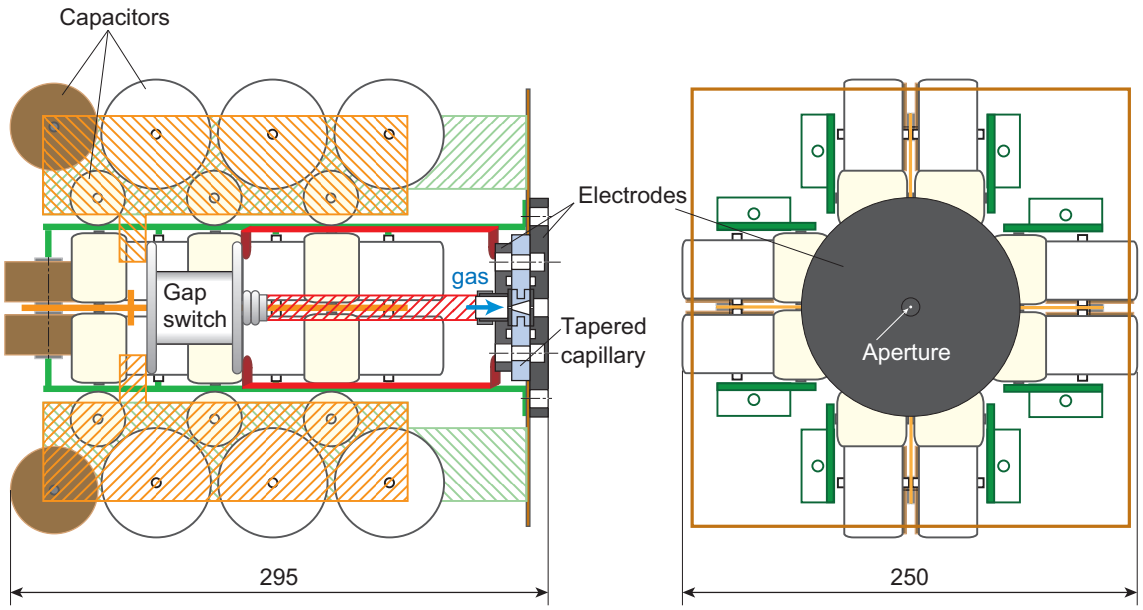

Figure 3.7: Schematic of discharge device with tapered capillary; the side view (left) and the front view (right).

this with circuit model, as indicated in the previous section, the size of the discharge circuit was enough smaller than scale length of variation of electromagnetic waves propagating in the circuit.

In order to drive the fast pinching plasma, pulse power device was constructed. We made efforts to decrease the discharge inductance as low as possible to approach the plasma impedance in the capillary. Figure 3.7 shows a schematic of the pulse power device with a tapered capillary. In the figure, the parts indicated by red, green and orange lines are made of copper sheet that reduced the stray inductance. The capacitors were placed so as to surround a gap switch and the tapered capillary. The main discharge circuit was axisymmetrically arranged as shown by Fig. 3.7 and also with the photograph in Fig. 3.8 to form symmetric discharge current sheet in the capillary. Half of the capacitors of main discharge circuit are shown on the side view in Fig. 3.7. To reduce the circuit inductance, low inductance ceramic capacitors with 55 nF total were installed for energy strage. Then the stored energy in the capacitors was $\sim 3 - 5$ J.

The tapered capillary was made of epoxy resin by molding in a polyacetal flange using a brazen rod which has a contoured shape as illustrated in Fig. 3.9. We can make optional taper geometry with this method. The length and the inlet radius of tapered capillary were 10 mm and 0.5 mm, respectively. The boundary of the polyacetal joint has steps to prevent surface flashover along the outer surface.

Figure 3.10 shows the discharge circuit. The discharge device was composed with main discharge circuit, DC pre-ionization discharge circuit, and pulse pre-ionization discharge circuit. The main and pulse pre-ionization discharge current were measured by a Rogowski coil.

The gap switches [PerkinElmer optoelectronics inc., GP-86] were installed for switching high voltage discharge of $\sim$ 10 kV. The jitter of the gap switch was less than 100 ns in applicable voltage. We developed a 20 kV trigger pulser to drive the gas switch which is shown in Fig. 3.11. A delay pulse generator [Stanford Research System, Inc., DG535] controlled the timing between the main and the pre-ionizing discharge. The delay pulse generator was connected by an optical fiber to isolate the pulser from the high voltage circuit.

Typical waveforms of pre-ionization and main discharge currents are shown in Figs. 3.12 and 3.13. The main discharge was driven $\sim$ 40 μs after the rise of the second pre-ionization current. The stray inductance of the discharge circuit was estimated to be $\sim$ 80 nH from the current waveform, then the impedance of discharge circuit $Z_c = \sqrt{L/C}$ was estimated to be 1.2 Ω. The nominal period of discharge current τ was $\sim$ 400 ns.

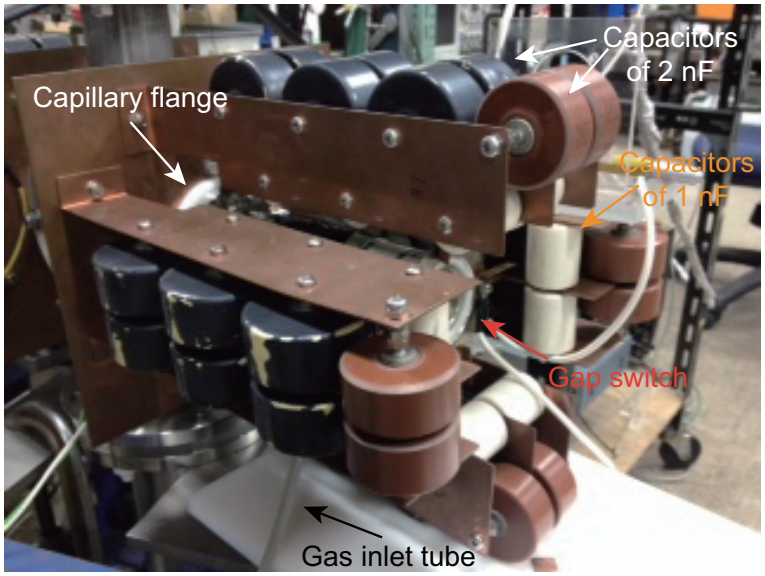

Figure 3.8: Photograph of TPP device.

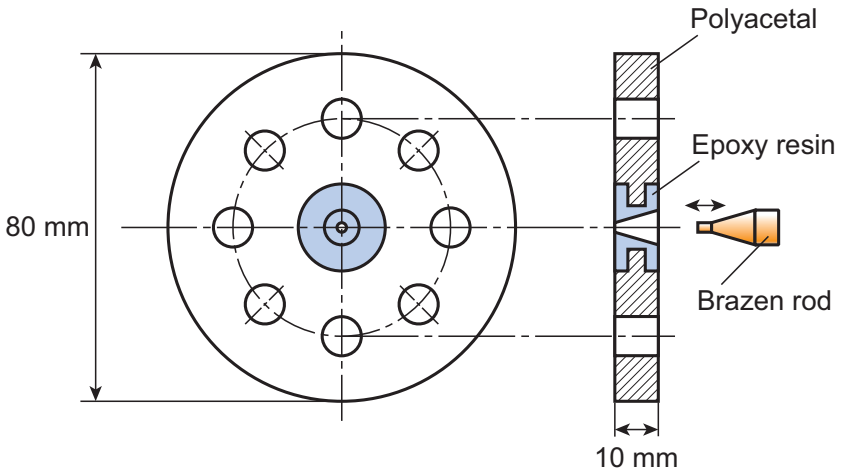

Figure 3.9: Details of tapered capillary.

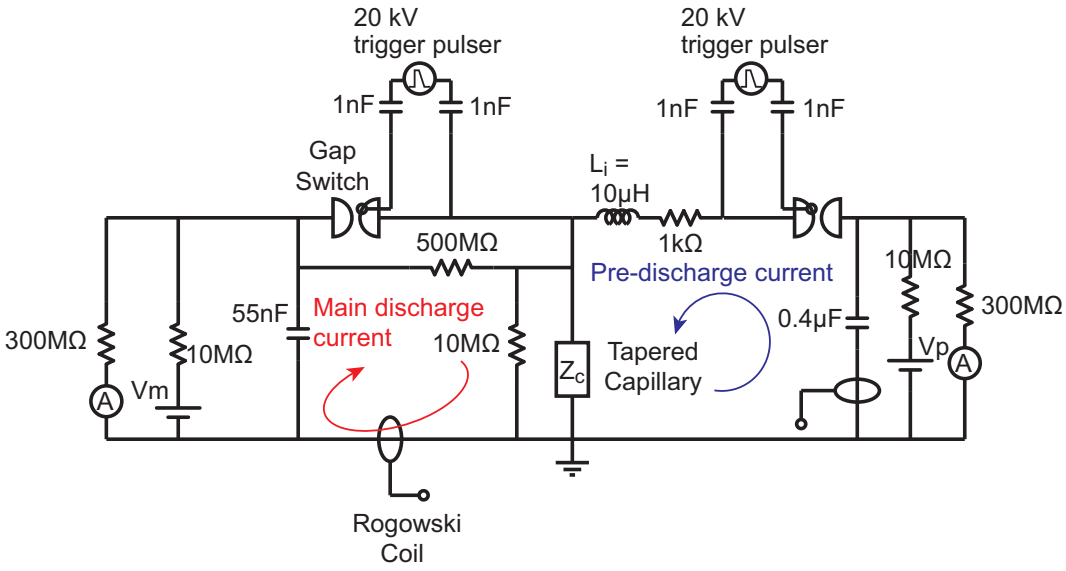

Figure 3.10: Equivalent circuit of pre-ionization and current drive for tapered pinch plasma.

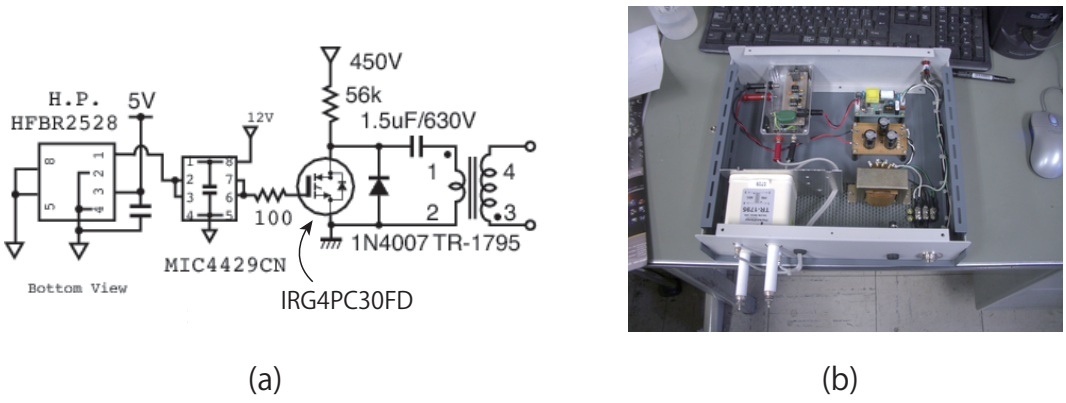

(a) (b)

Figure 3.11: Diagram of discharge circuit of 20 kV trigger pulser (a) and the photograph (b).

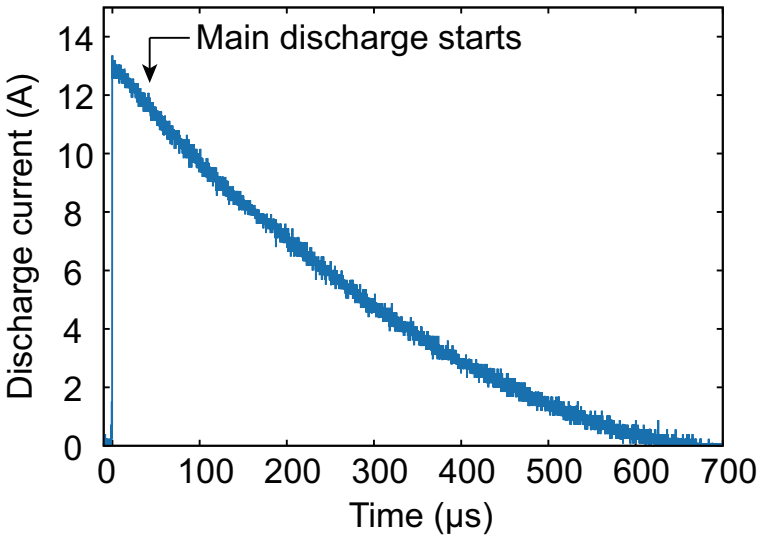

Figure 3.12: Pre-discharge current waveform.

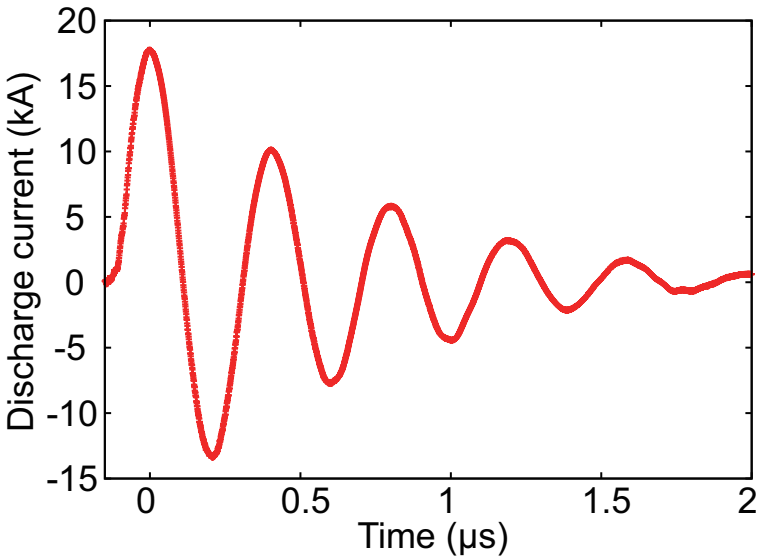

Figure 3.13: Typical waveform of main discharge current .

3.2.4 Devices for making well-controlled plasma

· Pre-filled gas condition through differential pumping

An illustration of the detailed structure of taper capillary and electrodes is shown in Fig. 3.14. Gas supply with "puffing" method was usually used for fast z-pinch devices [70, 71]. However, it was difficult to control the density profile of transient gas flow.

In our device, the working gas was supplied to the capillary through the cathode aperture and pumped by a turbo pump via the anode aperture as shown in Fig. 3.14. The finite gas conductance of anode aperture makes a pressure difference between outside and inside of the tapered capillary. The tapered capillary was filled quasi-statically with a well-defined density of argon by the continuous gas supply from the cathode aperture and differential pumping through the anode aperture.

The pre-filled gas density in the tapered capillary was calibrated in advance. An ionization gauge and a Pirani gauge were used to calibrate the pressures outside and inside the capillary. The relation between the outside and inside pressures is shown in Fig. 3.15. Typical values of the mean free path of the Ar gas were estimated to be ~ 0.1 mm in the capillary, ~ 10 cm in the test chamber.

· Dual pre-ionization for uniform implosion

Dual pre-ionizing circuit was installed to improve the reproducibility of tapered pinch discharge. To pre-ionize the Ar gas, a few kV of DC voltage was applied between the electrodes before pulse discharge. The DC pre-ionization could prevent localization of the current path of pulsed pre-ionization discharge. The main discharge current was driven after ~ 40 μs from the pulsed pre-ionizing current started. An oder of 10 A of pre-ionizing current moderates the non-uniformity of main discharge. The pre-ionization circuit was isolated from the main discharge circuit by an inductance $L_i \sim 10\mu$H.

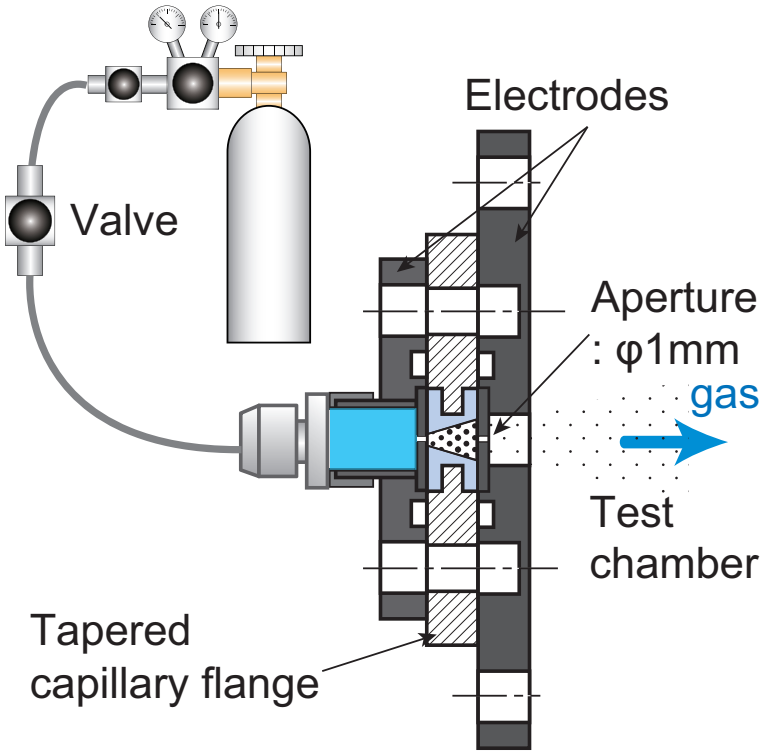

Figure 3.14: Schematic of gas supply and differential pumping system.

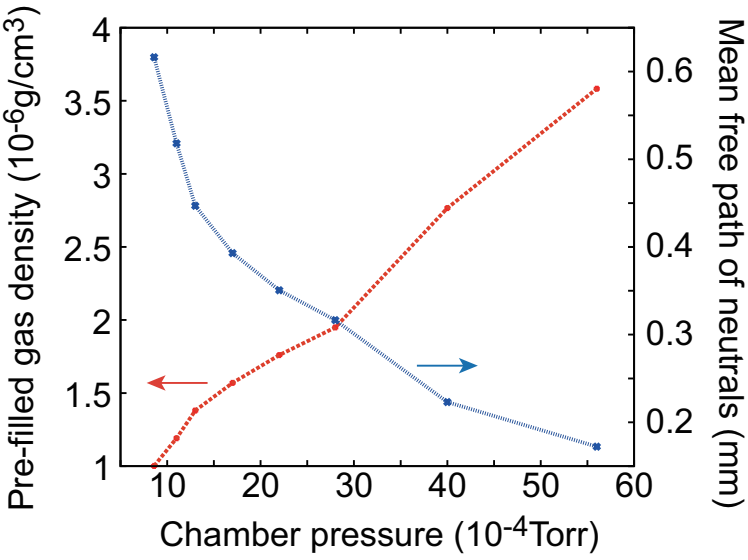

Figure 3.15: Calibration results of pre-filled gas in the capillary.

· **Magnetization control by apertured electrode**

From the estimation of skin depth in Sec. 3.2.1, the core part of pinching plasma is expected to be not magnetized strongly by the discharge current. The end electrode (Anode) has a small aperture of 1 mm in diameter which prevents the magnetic field from diffusion to the test chamber. Also, the discharge current decays at the time when the moving plasma arrives at a location of the test region. Then the moving plasma is expected to be not magnetized strongly by the discharge current.

· **Free-expansion for well-defined, high-Mach number flow**

The taper pinched plasma was extracted through the anode aperture. The point-like plasma at the aperture was accelerated and cooled through free expansion in the test chamber, which contributed to make a well-defined high-Mach number flow.

3.2.5 Typical flux-waveform and its reproducibility

Peak flux and drift speed of the moving plasma were measured by a Faraday cup (FC) as shown in Fig. 3.16, as a function of the gas density, the peak discharge current, the taper angle and the distance from capillary exit. The cup was made of brass with effective diameter of 20 mm and depth of 40 mm. The bottom of the cup has a conical shape to collect the secondly electrons. The flux collecting plate was biased to -100 V to suppress the co-moving electron signal. When the flux measurement was made at distance shorter than 350 mm, we decreased the effective diameter of FC to 5 mm and the depth to 10 mm to avoid the breakdown between the biased charge collector and the ground. In addition, a metal grid was installed on the cup aperture to equate the plasma potential to the ground that reduced the effective area to 44 %.

The drift velocity of plasma was estimated by the time of flight (TOF) of the plasma flux waveform: by the arrival time and a distance of the FC from the capillary. An arrival time of the plasma was defined by a time between the first peak of discharge

current and the peak value of plasma flux. For the drifting plasma, ion flux J_p can be described by:

$$J_p = Z_i e n_i v_i. \tag{3.22}$$

Employing $v_i = v_{TOF}$, ion density n_i at peak flux can be estimated.

Figure 3.17(a) and (b) show typical plasma flux waveforms measured at 200 mm. In order to evaluate the reproducibility, the waveforms in Fig. 3.17 were overlaid for successive three operations. The flux signal may contain ions of carbon, oxygen and hydrogen since the tapered capillary was made of molded epoxy compound. However, the reproducibility was fairly good thanks to the quasi-stational pre-filled gas supply and the dual-stage pre-ionization of the initial gas.

When the taper angle decreased, second peak appeared in the plasma flux waveform as shown in Fig. 3.17 (b). The plasma flux waveform also depended on the experimental parameters. As shown in this section, we found that the reproducibility of plasma formation is sufficient for parametric study of the taper-pinched plasma with well-defined experimental condition by the stationary gas supply and the pre-ionization.

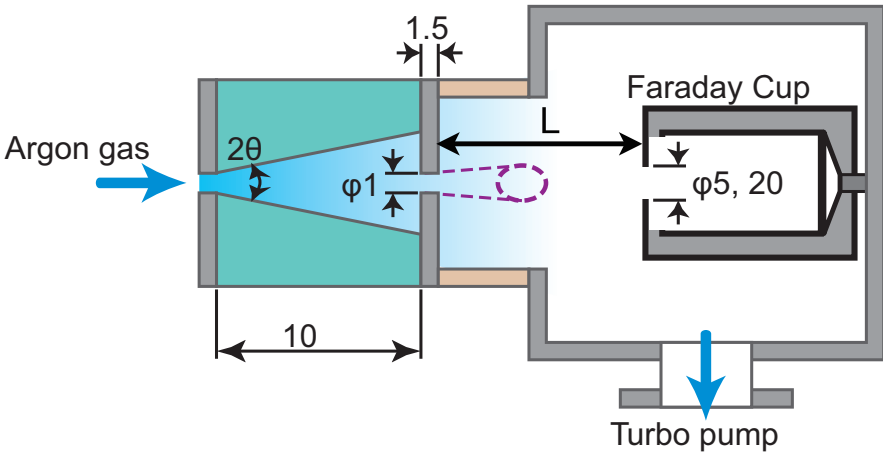

Figure 3.16: Schematic of plasma measurement.

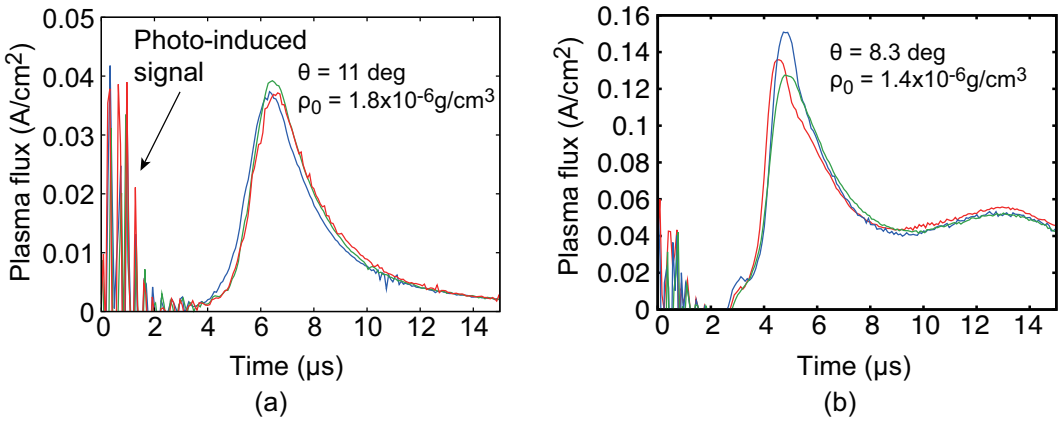

Figure 3.17: Typical plasma flux waveforms at 200 mm from the capillary with pre-filled gas density $\rho_0 = 1.4\times10^{-6}$ g/cm^3 and taper angle $\theta = 11$ deg (a) and with pre-filled gas density $\rho_0 = 1.8\times10^{-6}$g/cm^3 and taper angle $\theta = 8.3$ deg (b), where peak discharge current was 7 kA.

3.3 Controllability of tapered pinch discharge

Expected control parameters of the tapered pinch plasma can be predicted with consideration of the equation of motion of the current sheet shown by Eq. (3.9). That indicates the behavior of current sheet is basically controlled by initial mass density ρ_0, discharge current waveform $I(t)$ and initial radius r_0. In case of pinching process in the tapered discharge, the taper angle θ should become an important parameter in addition to those parameters.

The plasma flux and the velocity are difficult to estimate quantitatively with numerical simulation based on the 1D equation of motion because the axial pressure gradients and the effect of plasma accumulation are neglected in the simplified model. Thus, the relationships between the experimental conditions (i.e., initial gas density in the capillary, discharge current waveform, and capillary geometry) and the plasma parameters (i.e., axial velocity, flux, and temperature) are not clarified yet. Before applying the plasma source to laboratory astrophysics experiments, we examined characteristics of the TPP.

3.3.1 Dependence of plasma flux and velocity on pre-filled gas density

We found dependence of the plasma flux and the velocity on pre-filled gas density as shown in Fig. 3.18(a) and (b). As shown in Fig. 3.18 (a), the plasma flux increased with decreasing of pre-filled gas density. That is, increase of the pre-filled gas density caused the decrease of plasma flux, probably because of over-accumulation of particles during the sequential pinching process.

On the other hand, the plasma velocity kept the value $\sim$ 40 km/s in low density region and decreased in the region where the pre-filled gas density is larger than 3×10^{-6}g/cm^{-3} as shown in Fig. 3.18(b).

We also examined those dependences on taper angles (for θ= 5, 8.3, 9.6, 11 (deg)) of the capillary. The results are also shown in Fig. 3.18 that indicates changing the taper angle affects the dependences of the plasma flux and the plasma velocity on

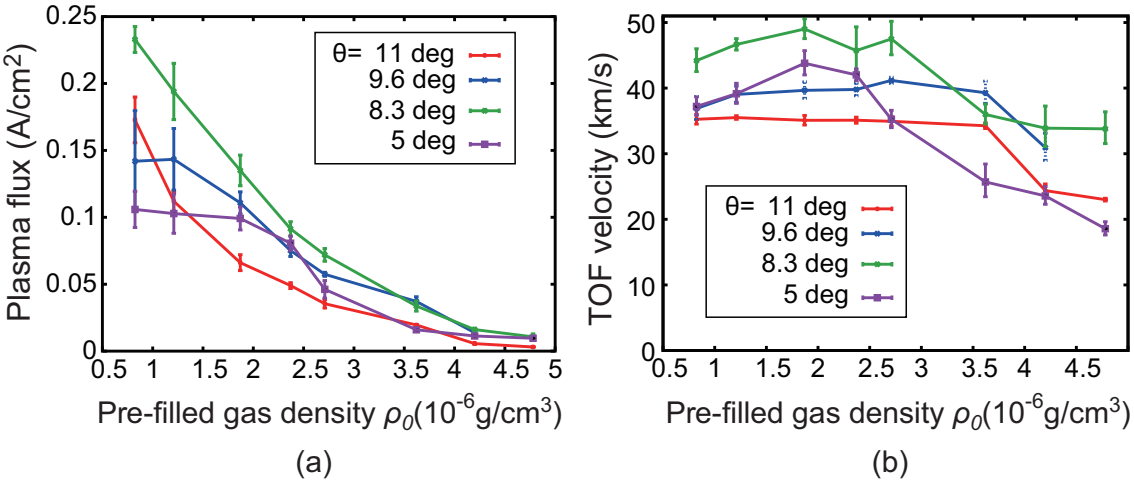

Figure 3.18: Dependence of plasma flux and velocity on pre-filled gas density (I_0 = 10kA).

pre-filled gas density. In the region where the pre-filled gas density was less than 3×10^{-6}g/cm^{-3}, the plasma velocity did not depend on the density.

3.3.2 Dependence of plasma flux and velocity on peak discharge current

Figure 3.19 (a) and (b) show the dependence of the plasma flux and the velocity on the peak discharge current. As shown, the plasma flux and the velocity increased almost linearly with increasing the discharge current in our experimental condition. We also show the fitting lines for the I_0-dependence with least square method in this figure.

For the capillary with θ = 9.6 deg we found that, the plasma flux J_p and the plasma velocity v_p can be scaled as:

$$J_p(\mathrm{A/cm^2}) = 0.0022 I_0(\mathrm{kA}) - 0.0091 \tag{3.23}$$

$$v_p = 4.2 I_0(\mathrm{kA}) + 6.9. \tag{3.24}$$

For the capillary with $\theta = 8.3$ deg, the plasma flux and velocity can be

$$J_p(\mathrm{A/cm^2}) = 0.0036 I_0(\mathrm{kA}) - 0.023 \tag{3.25}$$

$$v_p = 8.8 I_0(\mathrm{kA}) - 25. \tag{3.26}$$

Although, it is not clear whether these fitting lines can applicable for the region lager than the discharge current of 10 kA, we can use those scaling equations to predict J_p and v_p in the region.

Figure 3.20 shows dependence of plasma density on peak discharge current which is obtained from the results shown in Fig. 3.19 and the relation of $J_p = Zen_iv_i$. The effect of ionization degree Z will be discussed in Chapter 5. The plasma density was non-linearly dependent on the peak discharge current.

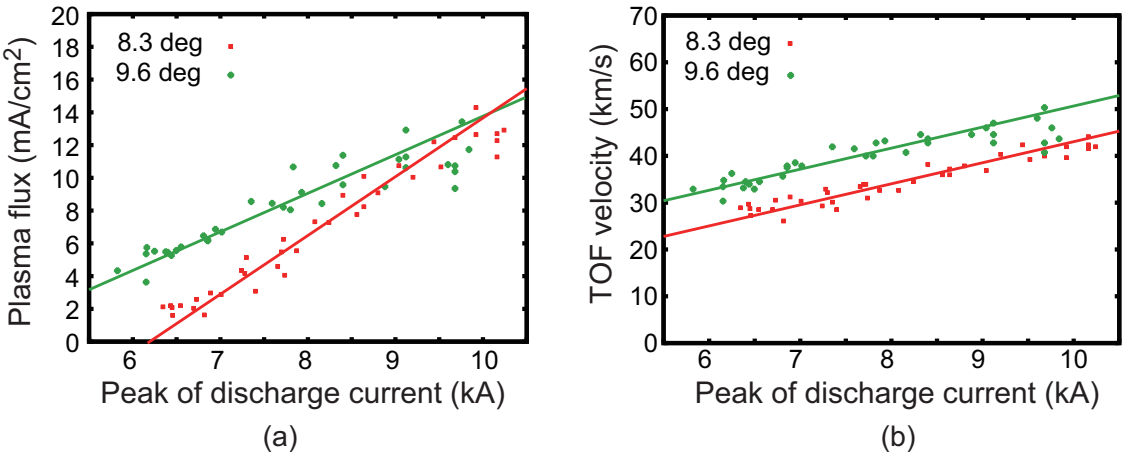

Figure 3.19: Dependence of plasma flux and velocity on peak discharge current.

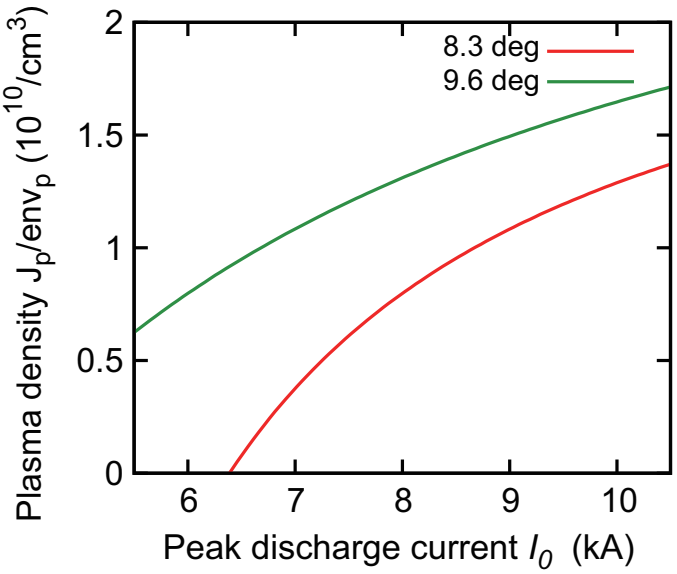

Figure 3.20: Dependence of plasma density on peak discharge current estimated by fitting lines in Fig. 3.19.

3.3.3 Geometry effect

In this device, although the geometry of tapered capillary is expected to play an important role in the compression and acceleration of pinch plasma, the geometrical effect was not discussed [38, 72]. We intend to clarify the behavior of the TPP using capillaries with various geometrical parameters. For example, the initial radius of plasma changes longitudinally by $r_0(z) = r_0(0) + z \tan\theta$ in case of conical capillary. Hence the pinching force depends on the axial distance z in the tapered capillary.

In the TPP device, the acceleration is expected to depend on the pinching dynamics in the changing geometry. We considered 1D motion of the pinching current sheet based on Eq. (3.9). The pinching time is determined by the initial radius of current sheet if discharge current and initial gas density are the same.

We intend to make synchronization between the axial motions of moving plasma in the capillary and the pinching current sheet. Figure 3.21 shows two types of tapered capillary geometries with which we considered the geometry effect. The pinching times of plasma in the two type of capillary were estimated with the 1-D snow-plow model and results are shown in Fig. 3.22. Where we defined a pinching time when the current sheet reaches to 10 μm from the center axis. Although the calculation does not include the plasma accumulation effects, it indicates that, if the plasma moves at 100 km/s from $z = 0$, the current sheet in the type 1 capillary does not contribute the acceleration of moving plasma.

In the two-step capillary (Fig. 3.21(b)), the pinching times are less than one-step capillary in the region of $z \geq 5$ mm and they approach to the dotted line. When we use the two-step geometry, the pinching plasma can contribute the acceleration in $z \geq 5$ mm also.

A comparison of the plasma flux measurements between the one-step (conical) and the two-step capillaries is shown in Fig. 3.23(a) and (b). When we increased the discharge current, the plasma flux of the two-step capillary increased rapidly than the one-step capillary as shown in Fig. 3.23 (a). The results indicate that the plasma density increased in the downstream of two-step capillary. This means that the plasma

density can be controlled by the capillary geometry in which synchronization of the moving plasma and the pinching current sheet are considered. Also, we found that the plasma flux waveform can be changed by the capillary geometry [39].

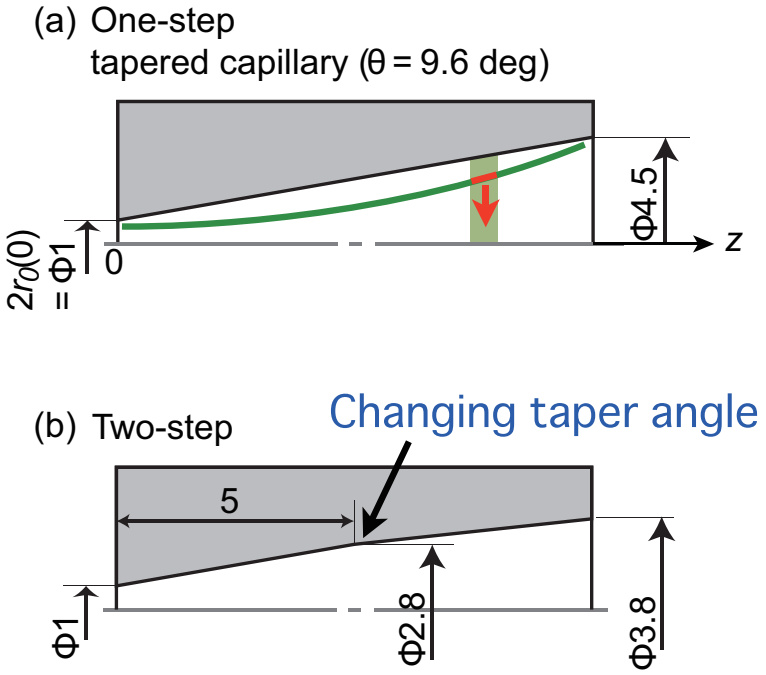

Figure 3.21: Capillary geometries used for characterization of geometrical effect on the pinched plasma.

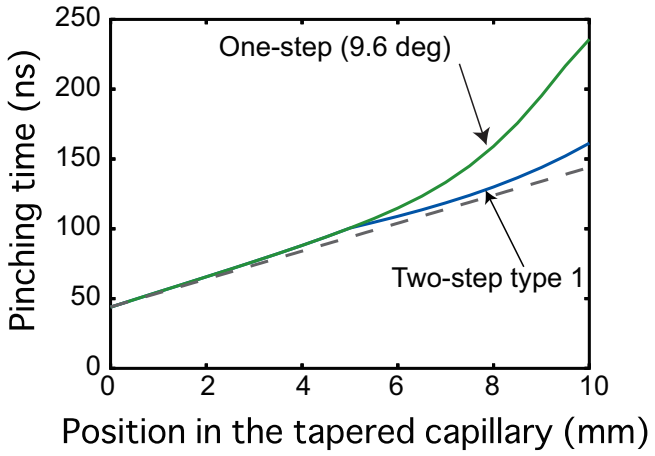

Figure 3.22: Geometry effect on pinching time, where the pinching times are estimated with simplified model described by Eq. (3.9) under the condition with initial gas density $\rho_0 = 2.4 \times 10^{-6}$ g/cm^3, and peak discharge current $I_0 = 10$ kA.

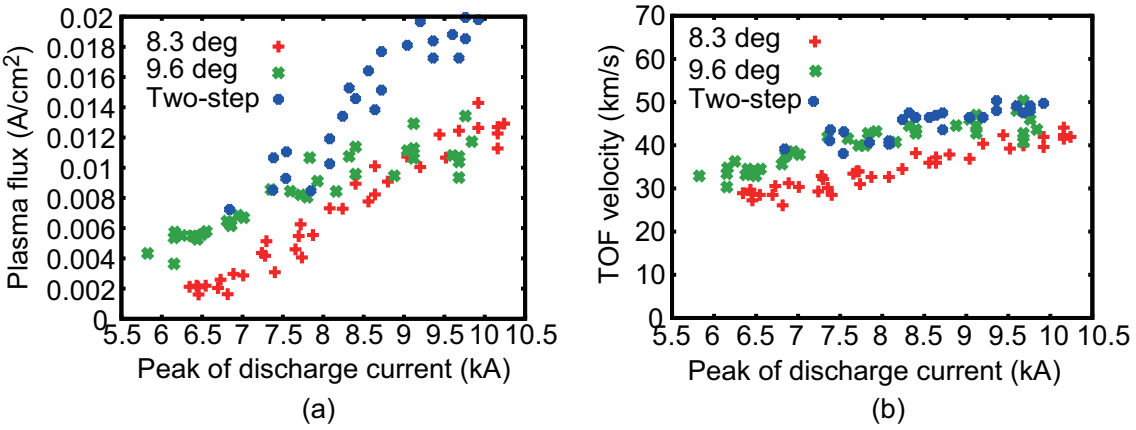

Figure 3.23: Dependence of plasma flux and velocity on peak discharge current at $\rho_0 = 2.4 \times 10^{-6}$g/cm^3 (FC was located 430 mm from the end of the tapered capillary).

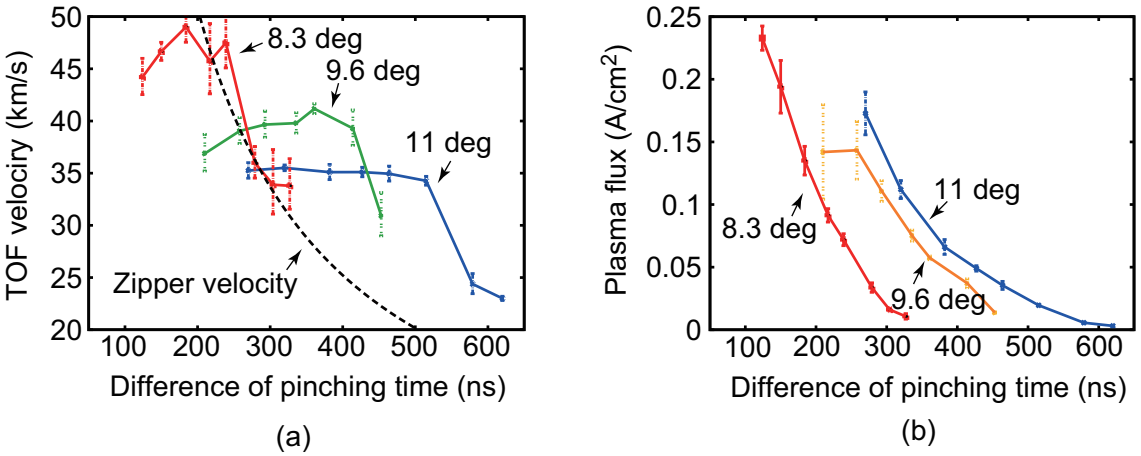

Figure 3.24: TOF velocity (a) and plasma flux (b) versus the pinching time difference, where zipper velocity (dashed line) based on pinching time estimated by Eq. (3.9).

3.3.4 Zipper velocity of taper pinched plasma

In order to derive a guideline for the capillary geometry, we assume the axial plasma velocity is constant. We define zipper velocity as $v_{zipper} = l/(tp_o - tp_i)$, where l, tp_i, and tp_o are length of the capillary, pinching time at inlet, and outlet of radius of the tapered capillary. We reproduced the plasma flux and TOF velocity data in Fig. 3.18 as a function of the difference of pinching time. Figure 3.24 shows dependences of the plasma velocity and flux on the pinching time difference. Here the pinching time difference means $tp_o - tp_i$ and the dached line denotes zipper velocity estimated by Eq. (3.9). As shown in Fig. 3.24 (a), the zipper velocity (dashed line) can predict the TOF velocity of plasma jet made by capillary with smaller expansion angle (θ= 8.3 deg) in which axial accumulation is insignificant. An order of the zipper velocity and its tendency on the pinching time difference well agrees with TOF velocity. This means zipper velocity can provide us the guideline of design of tapered capillary.

3.3.5 Evaluation of plasma outside the tapered capillary

We expected that the tapered pinch plasma freely expands from the anode aperture in the test chamber without disturbance, with a drift velocity v_d as schematically

shown in Fig. 3.25. The drifting plasma is expected to be spherically expanding from a point-like plasma.

Assuming that the Maxwell distribution in the center-of-mass system of the drifted plasma with velocity v_d, the velocity distribution of ions can be described by the following equation [73]:

$$f_s(v_x, v_y, v_z) = \frac{n_0}{(2\pi k_B T_i/m_i)^{3/2}} \exp\left(-\frac{m_i(v_x^2 + v_y^2 + (v_z - v_d)^2)}{2k_B T_i}\right), \tag{3.27}$$

where v_x, v_y, and v_z are the components of thermal velocities of the plasma in the cartesian coordinate system. T_i is ion temperature, subscript x and y show parallel direction to surface of a detector, and z is the vertical coordinate.

Then, axial flux of the particles in the range $(v_x, \mathrm{d}v_x;\ v_y, \mathrm{d}v_y;\ v_z, \mathrm{d}v_z)$ can be written as:

$$(\text{flux}) = (\mathrm{d}v_x \cdot \mathrm{d}v_y \cdot \mathrm{d}v_z) \times v_z f_s, \tag{3.28}$$

where $\mathrm{d}v_x$ and $\mathrm{d}v_y$ show velocities of particle that can be reached the detector with area of $(\mathrm{d}x\mathrm{d}y)$ in a time of flight t [73]. These velocities are given by, respectively,

$$\mathrm{d}v_x = \mathrm{d}x/t, \tag{3.29}$$

$$\mathrm{d}v_y = \mathrm{d}y/t, \tag{3.30}$$

$$\mathrm{d}v_z = z\mathrm{d}t/t^2. \tag{3.31}$$

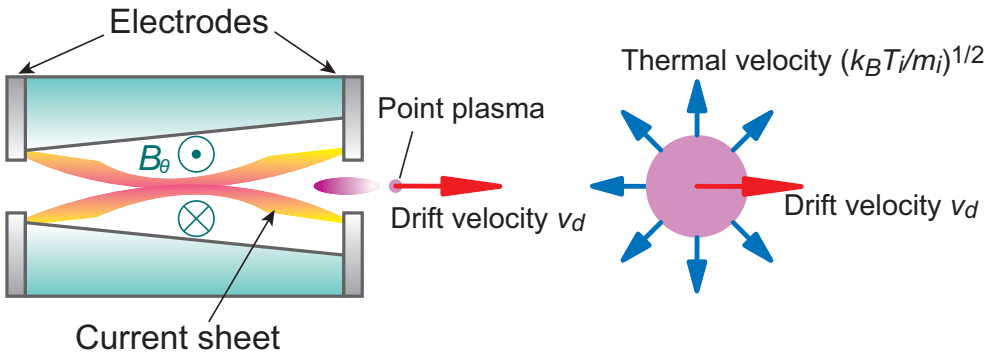

Figure 3.25: A schematic of plasma behavior in tapered pinch device which is pinched in capillary and freely expanding in test chamber.

Thus Eq. (3.28) becomes:

$$(\text{particle flux}) \propto (\mathrm{d}x\mathrm{d}y)\frac{z^2}{t^5}\frac{n_0}{(2\pi k_B T_i/m_i)^{3/2}}\exp\left(-\frac{m_i(v_x^2+v_y^2+(v_z-v_d)^2)}{2k_B T_i}\right). \quad (3.32)$$

For freely drifting plasma, the flux waveform is depending on the detector geometry. In case with surface sensitive detector such as Faraday cup, the flux J_p can be described based on the drift-Maxwellian distribution as:

$$J_p(z,t) \propto Ze\frac{z^2}{t^5}\exp\left[-\frac{M_i}{2k_B T_i}\left(\frac{z}{t}-v_d\right)\right], \quad (3.33)$$

where z is a distance from the capillary and t is the time from the plasma detached from the electrode and v_x and v_y are assumed to be zero. In case with volume sensitive detector such as ionization gauge, due to $\mathrm{d}v_z = \mathrm{d}z/t$, the flux J_p can be obtained as follows:

$$J_p(z,t) \propto Ze\frac{z}{t^4}\exp\left[-\frac{M_i}{2k_B T_i}\left(\frac{z}{t}-v_d\right)\right]. \quad (3.34)$$

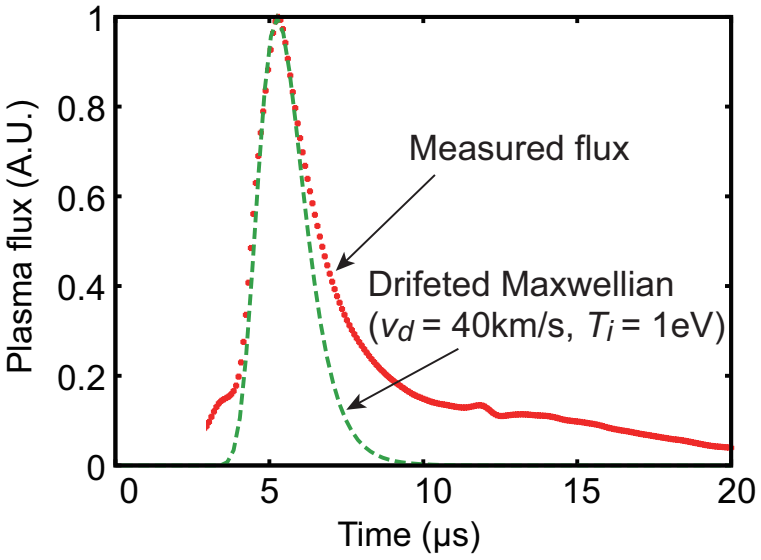

Figure 3.26: Comparison of plasma flux waveforms between the measured and estimated by drift-Maxwellian distribution with v_d=40km/s and $k_B T_i$=1 eV. The flux was measured at 23 cm from the capillary with taper angle θ=8.3 deg which is driven by peak discharge current of 10 kA.

Figure 3.26 shows a typical waveform of plasma flux at 23 cm from the end of capillary. As shown in Fig. 3.26, the plasma flux can be fitted by the drift-Maxwellian distribution except the tail part. The discrepancy between the plasma flux waveform and the drift-Maxwellian distribution may be attributed to the finite length of the capillary.

We measured the plasma flux as a function of the distance from capillary with the Faraday cup. Assuming that most ions at the peak plasma flux are drifting with $z/t = v_d$, Eq. (3.34) indicated that temporal evolution of peak plasma flux can be written as $J_p \propto z^{-3}$. Figure 3.27 shows the evolution of peak plasma flux in the chamber and the fitting curves by Eq. (3.34).

As was explained in Sec. 3.2.4, one of the advantages of TPP is the exclusion of current-induced magnetic field from the plasma flow. Also plasma can not be magnetized in the test chamber, as was shown in Fig. 3.13, because the discharge current decays almost completely after 2 μs from the start. The result shown in Fig.

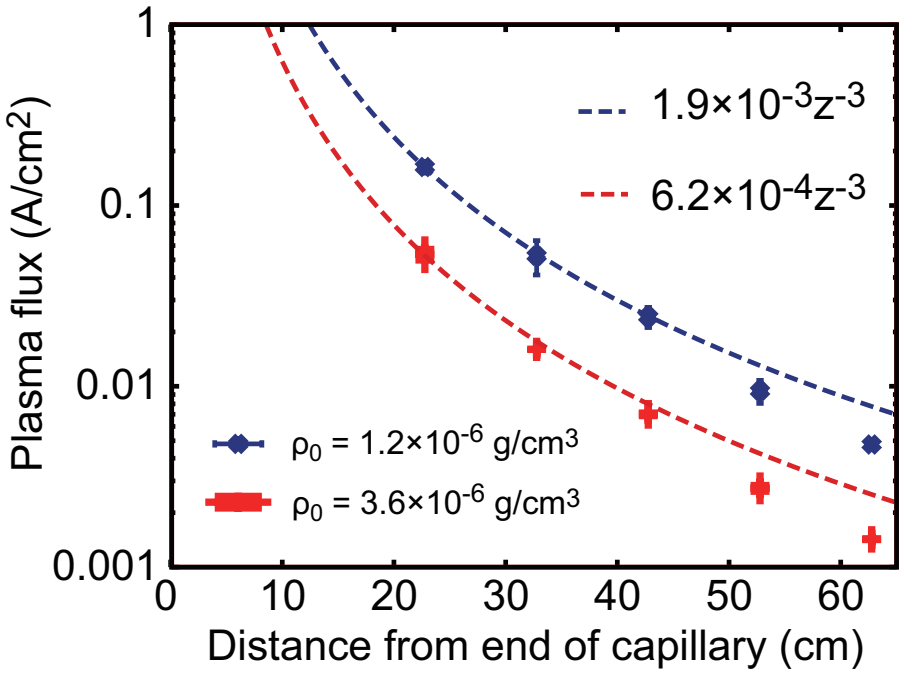

Figure 3.27: Evolution of peak plasma flux from capillary end.

3.27 indicates that the TPP is drifting freely in the test chamber without discharge-current-induced magnetic field.

3.4 Summary

In this chapter, we showed TPP device can form high-speed plasma flow with controllability, reproducibility, and repeatability to perform the parametric study relevant to astrophysics. We also emphasized that the TPP device can drive a plasma high-Mach number plasma flow with a table-top pulsed power device.

An experimental device composed of a tapered thin capillary, a fast pulsed power driver, a differentially pumped gas supply system, and a dual-stage pre-ionization circuit, has been constructed to make a dense, high-speed, and well-controlled plasma for laboratory astrophysics experiment. A strong magnetic field in a thin, tapered capillary contributed to form high-speed plasma flow. Pre-filled gas density inside the capillary wall was well-defined due to a continuous gas supply system. A well-defined initial condition of capillary discharge by virtue of the stational gas fill and dual-stage pre-ionization enabled us to make reproducible plasma flow. Detailed discussion of the ion acoustic Mach number will be shown in Sec. 5.2.

We measured the plasma flux and the plasma velocity in the chamber with Faraday cup measurements as a function of the pre-filled gas density, the peak discharge current, and the taper geometry. We found that the flux and the drift speed increase almost linearly with discharge current in the operational region of our device. The evolution of Faraday cup signal in the test chamber showed that the taper-pinched plasma expands from a point-like state almost free without magnetization. We also found that consideration on the synchronization of a moving plasma with a pinching current sheet is a key point to control the pinch process.

Chapter 4

Counter-stream Experiments

4.1 Concept of interaction experiments using counter-streaming plasma flow

Our aim of study is to perform an interaction experiment of high-speed flow under a well-defined plasma condition. We decided to use the taper pinched plasma with a counter-streaming configuration in which the high speed plasma interacts at the center of the test chamber with well-defined condition and good reproducibility. Counter-streaming plasma configurations have found in application for inertial fusion device from 1990's [74]. Recently, in the experiment with high-intensity laser facility [27] and related PIC simulation [75, 76] schemes with counter-streaming configurations have arisen much interests relevant to the astrophysics.

As has been discussed in Sec. 2.6.1, disadvantages of using the high-power laser facility are short interaction time, small scale length, and low capability of repetitive operation. Table-top pulse discharge devices can be useful for the laboratory astrophysics experiments. We expected to make interaction experiments using a counter-streaming force-free plasma flows made by TPP devices. An illustration of the arrangement of counter-streaming experiments with TPP is shown in Fig. 4.1.

Interaction experiments using counter-streaming configuration are useful for parametric study over a wide range of parameters of plasma shocks, which is inevitable for discussion of the complex structure.

In the counter-streaming experiments using TPPs, not only relative velocity of plasma flows, also the plasma density in the interacting region can be controllable. Collisional effects namely the ion density in the interacting region can be controlled by the drift distance of freely expanding plasma.

The advantages of the counter-flow experimental scheme based on the TPPs are summarized as follows:

- Well-defined and controllable plasma flows;
- Increase of relative velocity of plasma flows;
- Controllable magnetization;
- Reproducible and repetitive operation.

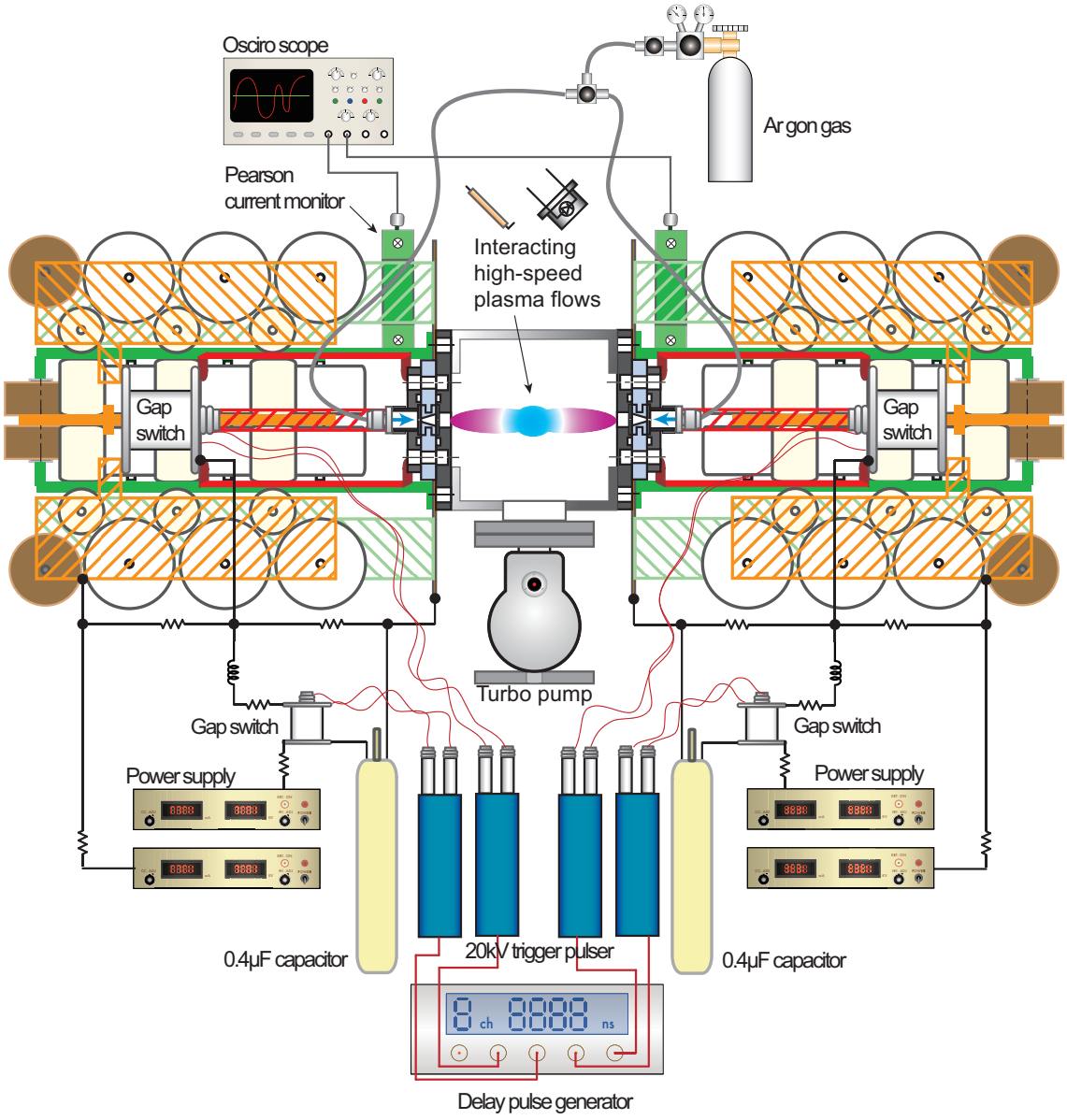

Figure 4.1: Schematic of the counter-streaming experiments.

4.2 Experimental setup

4.2.1 Synchronization of counter flows

We show a schematic view of the experimental setup for the counter-streaming plasma flows in Fig. 4.1. We installed a pre-filled gas supply system based on differential pumping and a two-stage pre-ionization circuits to get good reproducibility. As was discussed in the previous chapter, the pre-filled gas in tapered capillaries was pre-ionized by the dual-stage pre-ionization circuits which reduced the jitter of plasma formation. To synchronize the exposure time of fast framing camera and the plasma flow near the center of the chamber, the delay pulser DG535 controlled the timing.

In counter-streaming experiments, two TPPs must be synchronized without excessive jitter. For evaluation of the reproducibility, we use the arithmetic mean μ and the standard deviation of the discharge timing with unbiased variance σ:

$$\mu = \frac{1}{n}\sum_{i}^{n} X_i, \quad \sigma^2 = \frac{1}{n-1}\sum_{i}^{n}(X_i - \mu)^2 \tag{4.1}$$

where X_i and n are sample data and the number of data. We assumed that the arrival times from the trigger pulse are expected to follow the normal distribution as illustrated in Fig. 4.2. We evaluated the average and the standard deviation for 30 samples of the arrival times, peak discharge currents, Langmuir probe signals. The results are summarized in Tab. 4.1. We defined the trigger time as a time when the pulse was generated by the delay pulser DG535.

As shown in the table, the arrival times and the signal peaks existed within a region of about 20 percent of the average. We could perform reproducible counter-streaming experiments by adjusting those timings based on the data.

Table 4.1: Averages and deviations of arrival times and peak of signals.

	Average μ	Standard deviation σ	μ/σ
From trigger to current	2.48	0.491	0.199
From trigger to flux	6.31	1.20	0.191
From current to flux	3.83	0.748	0.195
Peak discharge current (kA)	10.0	1.87	0.187
Peak probe current (mA)	3.14	0.771	0.246

4.2.2 Setups of fast framing camera, photodiode, and Langmuir probe

For observation of the interacting plasma flow, a Langmuir probe, a photodiode detector and a high-speed camera were used simultaneously. The experimental arrangement and the diagnostics of interacting plasma are shown in Fig. 4.4.

The fast framing camera [DRS HANLAND. Ltd., Imacon 468] with lens [Nikon Co. Ai AF Micro Nikkor 105 mm F2.8D] can take the visible images of the counter-streaming plasma interaction with minimum exposure time of 10 ns. The trigger pulse for the framing camera was supplied by a Pearson current monitor placed in the current path of the pulsed power device. The camera can take four images at

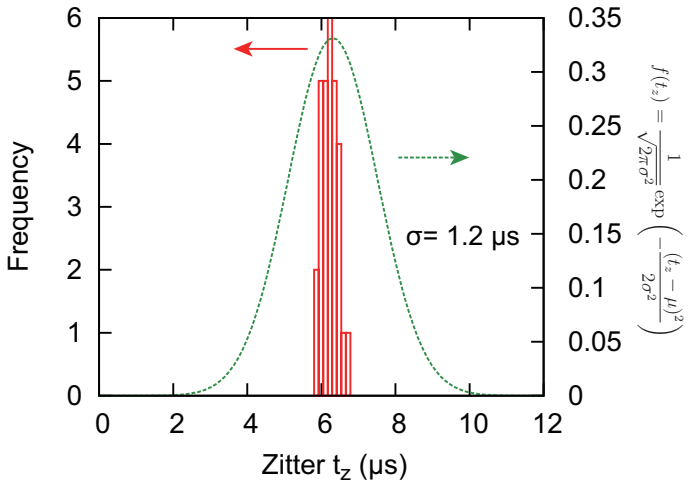

Figure 4.2: Histogram of arrival times of peak flux signals from trigger times of main discharge.

different timings. Thus, we can observe the successive visible images of the counter-streaming flows as a function of the discharge time. In the imaging experiments, the exposure time was extended to 500 ns to observe the faint light emission from the interacting plasma.

The light emission from the interacting plasma was measured also by photodiode [Hamamatsu photonics K.K, Co., S1223-01] with an imaging lens [Sigma Koki, Co., BK 7 ϕ100 - f100]. The photo-sensitivity of diode is shown in Fig. 4.3. As shown, range of sensitivity is from 320-1100 nm.

Photosensitive area of the diode is 3.6×3.6 mm^2. The imaging lens and the photodiode were located at 200 mm and 400 mm from the center of the chamber. Hence the spatial resolution of photodiode measurement is estimated to be about 3.6 mm square.

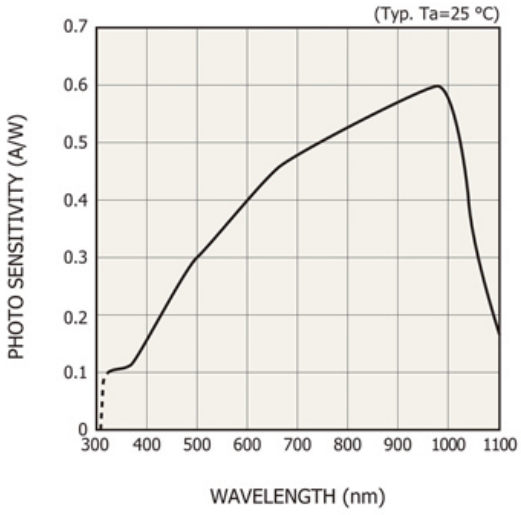

Figure 4.3: Photo-sensitivity of photodiode [77].

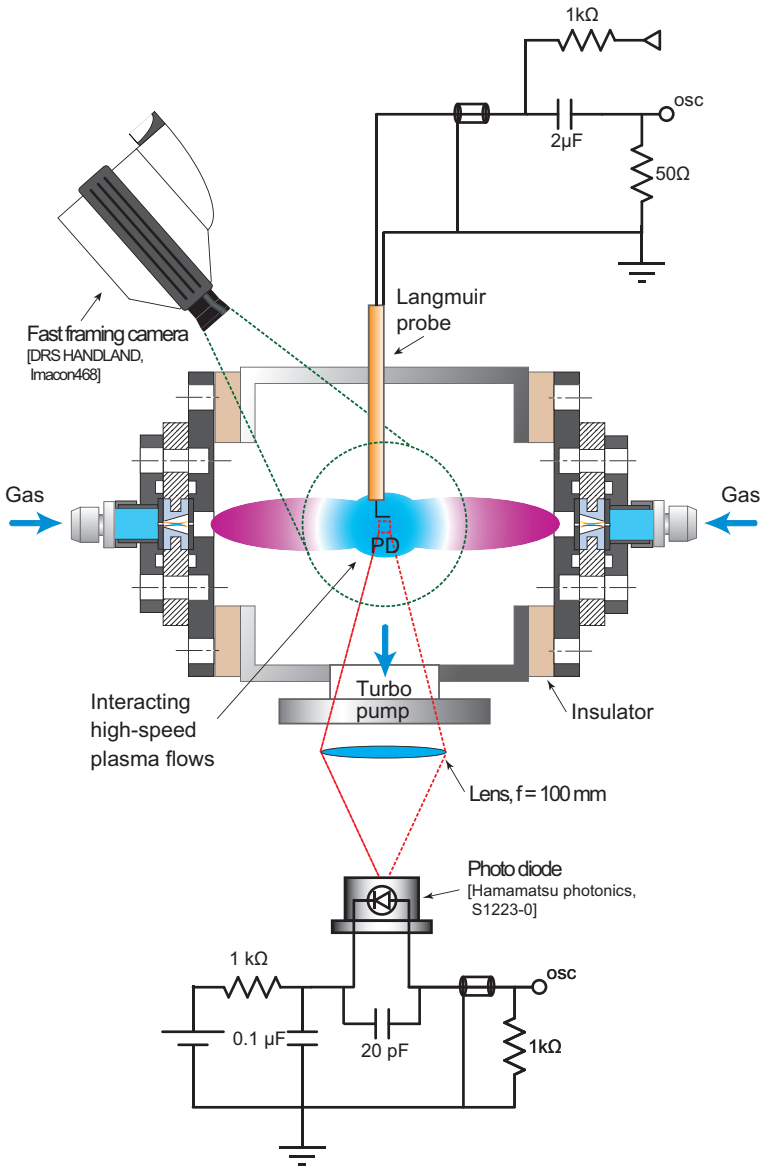

Figure 4.4: Schematic of diagnostics for interaction experiments with TPP device. Langmuir probe was located at the center of the test chamber; 80 mm from two tapered capillaries. Photo diode receives light emission from the center of the test chamber indicated by PD with spacial resolution of 3.6 mm square.

Table 4.2: Setup condition for photodiode.

Spatial resolution (mm^2)	3.6×3.6
Time resolution (ns)	30
Bias voltage (V)	15
Sensitive region of wavelength (nm)	320-1100

The setups of photodiode are summarized in Tab. 4.2. To observe the photo-induced signal, a load resistor of 1 kΩ was connected in parallel with a coaxial cable of $\sim$ 10 cm in length. The time resolution of the photodiode measurements was estimated from the product of load resistance R_{load} and the cable capacitance C_{cable} and the efective capacitance of photodiode terminals C_{diode}. The capacitance of the coaxial cable is estimated to be 10 pF from the calculation; $C_{cable} = 2\pi\epsilon/\ln(b/a) \sim$ 100 pF/m, where a, b, and ϵ are inner and outer diameter, and the permittivity of the cable material. Then, the time resolution $\sim R_{load}(C_{cable} + C_{diode})$ is estimated to be 30 ns, where C_{diode} is 20 pF.

A triple probe, allowing simultaneous measurement of plasma parameters without the need for voltage sweeps was established [79, 80] and applied to pulsed plasma flows [81]. However, in the interaction experiments, we used a single Langmuir probe with a simple configuration because the TPP had a good reproducibility.

In general, Langmuir probe consists of a wire or a metal disk, which is inserted into a plasma and electrically biased with respect to a reference electrode to collect electron and/or positive ion currents [78]. The probe current I_P consists of electron and ion components depending on the bias voltage. Several plasma parameters can be estimated from the relation between the probe current and the bias voltage. The Langmuir probe was used to observe the plasma flux and estimate the electron temperature in the interacting region.

In the interaction experiments, the Langmuir probe was located 8 cm from the anode. The probe was made of cylindrical copper wire with 0.1 mm diameter and 3 mm in length. The probe was placed so as to its longitudinal direction parallel to the plasma flow. Thus, the spatial resolution in the flow direction was 3 mm. the perpendicular part of the probe was covered by epoxy compound to reduce an amount

of the secondary electron emission and reduce the drift components from the probe current. The distance between the probe and center axis of the moving plasma was 5 mm as shown in Fig. 4.5.

In case with a bias voltage V_B is much larger than the plasma potential V_P ($V_B \gg V_p$), the probe collects the following electron saturation current I_{es}:

$$I_{es} = \frac{1}{4} e n_e S_p \left(\frac{8 k_B T_e}{2\pi m_e} \right)^{1/2} \tag{4.2}$$

where S_p shows the effective area of the probe. In case with electron temperature is larger than ion temperature, from formation condition of ion sheath [78], ion current is obtained by:

$$I_i = eZ n_i S_p \exp\left(-\frac{1}{2}\right) \left(\frac{k_B T_e}{m_i} \right)^{1/2}, \tag{4.3}$$

where factor $\exp(-1/2)$ shows decreasing rate of the density at the sheath edge.

The Langmuir probe measurement was conducted to estimate the electron temperature. For $V_B < V_P$ the electrons are partially repelled by the probe and the electron current decreases exponentially with V_B. For $V_B \ll V_P$ all electrons are repelled, so that electron current $I_e = 0$. The electron current can be expressed as

$$I_e = I_{es} \exp\left(-\frac{e(V_P - V_B)}{k_B T_e} \right), \quad V_B \leq V_P. \tag{4.4}$$

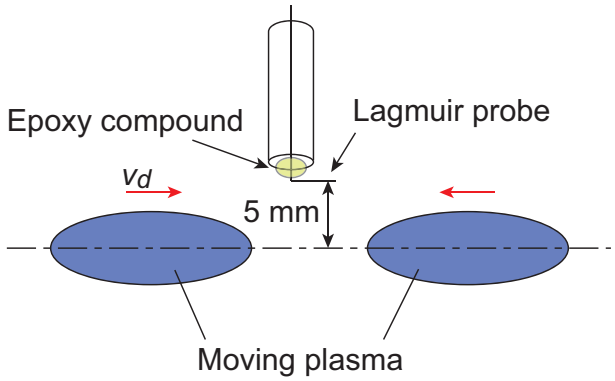

Figure 4.5: Schematic of Langmuir probe measurement.

Electron temperature was estimated by V-I characteristics of the Langmuir probe using the following equation

$$\ln \mid I_P(V_B) \mid = \frac{eV_B}{k_B T_e} + A, \tag{4.5}$$

where A is integrate constant.

In this experiment, the single probe was inserted to the high-speed plasma flow. The plasma potential may not be unique during the drift motion because the plasma flow can not connect directly to the wall of the chamber. Also, the plasma potential may be fluctuated due to the plasma interaction. However, the gradient of electron current versus the bias voltage at the timing of peak flux is expected to be reflecting the temperature.

4.2.3 Setup for spectroscopic measurement

We expected that the light emission from the high-speed plasma flow reflects the atomic process in the drifting plasma and also the effect of interaction of the flow. We made a spectrometer using a diffraction grating [Shimadzu Co., Ltd.] and a fast frame camera which was used to obtain the whole spectrum of the light emission in visible region from the plasma flows.

Figure 4.6 shows a top view of experimental setup composed of the whole view spectrometer and a streak unit [Hamamastu Photonics K.K., M2548 with C2830] with a CCD camera [Hamamatsu Photonics K.K., C3140]. The light from the plasma was focused on the 0.5 mm slit by a lens [Nikon, AF NIKKOR 50 mm; 1:1.4D]. The diffracted light was imaged on a frost diffuser panel with thickness of 2 mm [Sigma Koki], the spectral image was reflected by the mirror and imaged on the streak unit. The whole image of spectral emission was taken by the CCD camera.

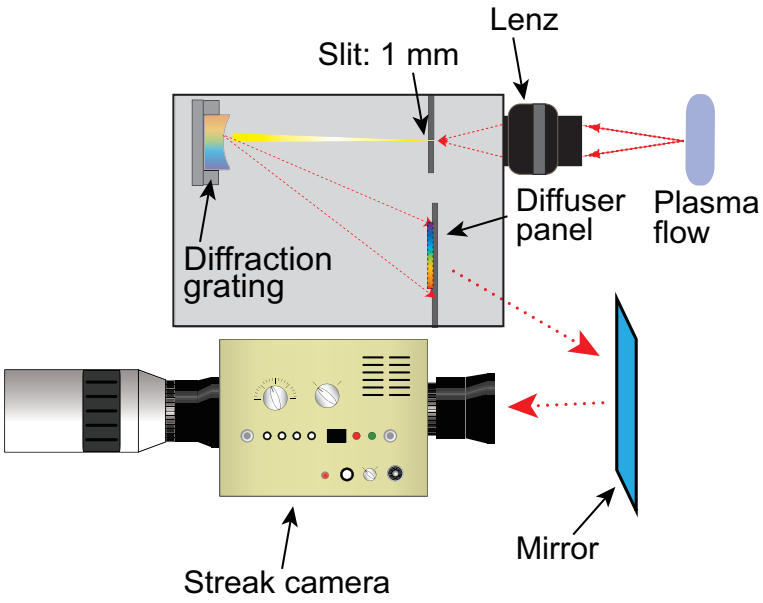

Figure 4.6: A schematic of "whole view" spectroscopic measurement.

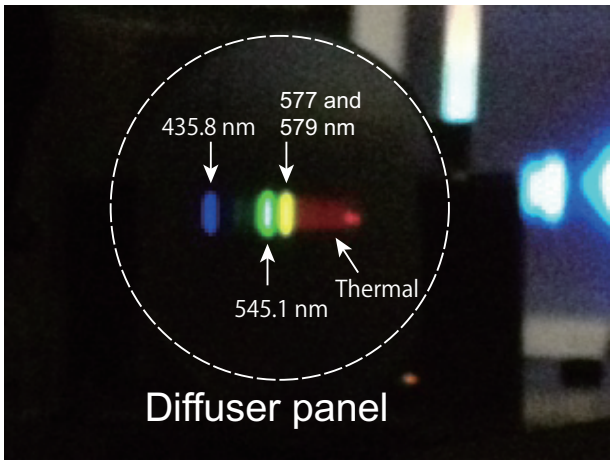

Figure 4.7: The spectrum of standard light source [Oriel Instruments, Co., 65130 (Hg)].

The spectrometer was calibrated by a spectral line lamp [Oriel Instruments, Co., 65130 (Hg)]. From the calibration, the sensitive region of the diffraction grating with width of 37 mm is estimated to be from 340 nm - 750 nm. We show the spectrum of the lamp in Fig. 4.7. As shown, the resonance lines and a continuum emission were confirmed.

The exposure timing was synchronized with the plasma behavior by a delay pulse generator. Because the light emission was very weak, the exposure time was set to be 1 ms after the pre-discharge current started.

Temporal behaviors of resonance lines of Ar were measured by a grating monochromator with Czerny-Turner configuration [Acton Research Co., VM-504] and a photomultiplier tube (PMT) [Hamamatsu Photonics K.K., R329-02]. We show the experimental setup for measurements of time resolved line emissions in Fig. 4.8. The bird's eye view of line emission measurements is shown in Fig. 4.9. The radiation emitted from the high-speed plasma flows was focused on the incident slit of 0.5 mm width by the lens [Nikon, AF NIKKOR 50 mm; 1:1.4D]. The spectral emission was focused on the PMT through the exit slit.

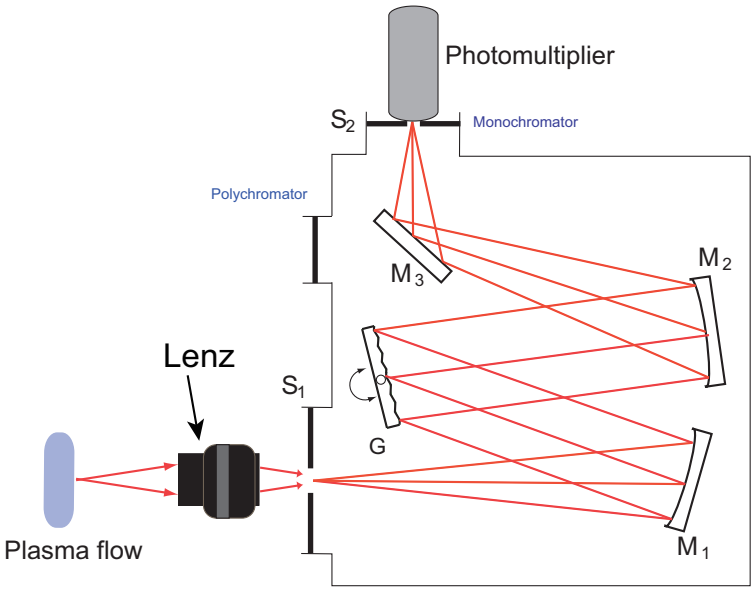

Figure 4.8: A schematic view of spectroscopic measurement of Ar-lines with photomultiplier.

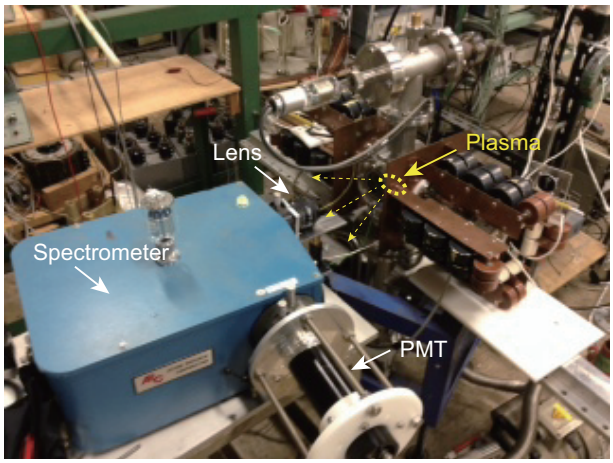

Figure 4.9: A photograph of spectroscopic measurement with photomultiplier.

In the PMT, photo electrons are amplified an order of 10^6 times using dynodes. Then we have to check the linearity of PMT signal. A schematic of the photomultiplier operation is shown in Fig. 4.10 [82]. The electron current at anode I_p increases from an initial photo-electron current I_{p0} according to the following relation:

$$I_p = \prod_{d=1}^{N} \delta_i(V_d) I_{pi} = A_p I_{p0}, \tag{4.6}$$

where δ, V_d, N, and A_p show an amplification factor at a dynode, voltage between the dynodes, number of the dynode, and the total amplification factor. The voltages of dynodes are supplied through a bleeder circuit. To maintain the amplification A_p constant against the signal level, the bleeder resisters and the decoupling capacitors were installed so as to keep the breeder voltage constant over a wide range of photo current.

The following is a required condition for liner amplification:

$$C_5 V_{13} \gg \int_{t_1}^{t_2} I_p \mathrm{dt}, \tag{4.7}$$

where C_5 and V_{13} are capacitance and voltage at resistor R_5 shown in Fig. 4.10. Table 4.3 and 4.4 show the installed decoupling capacitors and the resistors in the bleeder circuit. Bias voltage of - 1.9 kV was divided and was applied to the resistor R_5. We could estimate that the charge stored at C_5 ($C_5 V_{13}$) to be 0.1 C. As will be shown in Fig. 4.18, photo induced current was typically an order of 1 mA and the time scale was 10 μs. Then the total charge for photo signal was $\int_{t_1}^{t_2} I_p \mathrm{dt} = 0.01$ C. Hence, we can assume the liner relation in PMT signal was kept in our experiments.

The grating monochromator we used has a sensitive wavelength range of 115 - 1400 nm. On the other hand, the number of the grating and the reciprocal linear dispersion of this optics are 1200 g/mm and 2.1 nm/mm, respectively. Hence the spectral resolution of the set-up is estimated to be 6.3 nm. Meanwhile sensitive region of the PMT is from 165 nm to 650 nm.

The voltage was applied with a stabilized DC power supply [Hamamatsu Photonics K.K., C3360]. The load resister of the PMT was 1 kΩ and the time resolution was estimated to be 200 ns with a coaxial signal cable of 2 m in length. From the optical arrangement, the spatial resolution was estimated to be 1 mm. We summarize the setup condition for spectroscopic measurement in Tab. 4.5.

Table 4.3: Installed decoupling capacitors, (μF).

C_1	C_2	C_3	C_4	C_5
0.02	0.04	0.1	0.22	0.47

Table 4.4: Installed resistors in bleeder circuit, (kΩ).

R_1	R_2	R_3	R_4	R_5	R_6	R_7
475	160	120	-	-	-	120
R_8	R_9	R_{10}	R_{11}	R_{12}	R_{13}	
160	220	270	330	430	330	

Table 4.5: Setup condition of spectroscopy

Spacial resolution (mm)	1
Sensitive range of monochromator (nm)	115-1400
Reciprocal linear dispersion (nm/mm)	2.1
Resolution of wavelength (nm)	6.3
Sensitive range of PMT (nm)	165-650
Applied voltage (kV)	-1.9
Time resolution of PMT (ns)	200

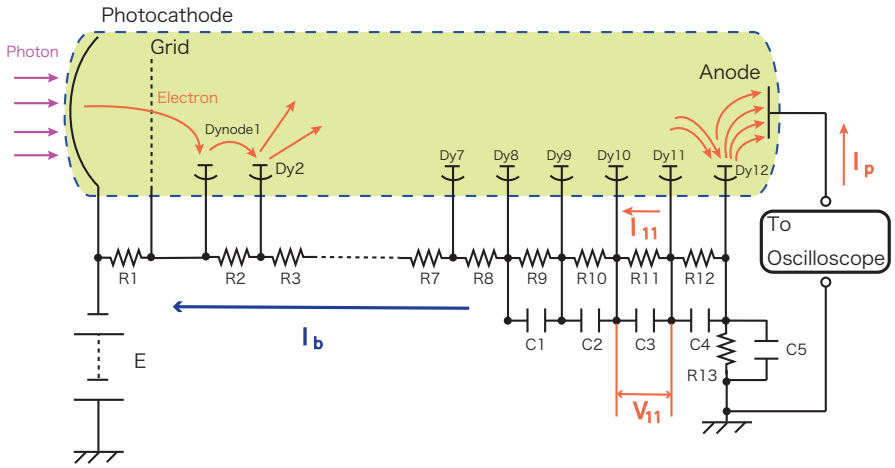

Figure 4.10: A schematic illustration of photomultiplier.

4.3 Spatial and temporal evolution of counter-streaming plasma

The visible image of the plasma were observed by the fast framing camera. The light emission from the plasma flow were measured by the photodiode and the monochromator with the PMT In addition, the plasma flux and electron temperature were estimated by the Langmuir probe. In this section, we show the results obtained with those diagnostics. We evaluate the signals from the interacting high-speed plasma from the comparison with those of the simple addition of independently operated single plasma flow, at base.

4.3.1 Optical and probe measurements of interacting plasma

Figure 4.11 shows typical framing images of the counter-streaming plasma, where PD in Fig. 4.11 shows observing area of the photodiode. Numbers 1, 2 and 3 in Fig. 4.11 and 4.13(a) show the timings of high speed camera. In this experiment, the exposure time was extended to 500 ns to adapt faint light emission from the plasma.

The jitter between arrival times of independent plasma flows is inevitable if the switch utilizes gas discharge. However the reproducibility of TPP was improved by pre-discharge and differential pumping as shown in Fig. 3.17. Hence the jitter of the

breakdown timing of gap switch i.e., the jitter of interacting plasma was suppressed to an order of 100 ns.

The color scale in Fig. 4.11 presents intensity of the light emission from the counter-streaming plasma flows in a range of visible light. The counter-streaming plasmas moved from both sides and merged at the center of vacuum chamber as shown in Fig. 4.11. The power density of light emission from the plasma flow was predicted to decrease with distance from the tapered capillary because the plasma was expanding freely outside the capillary.

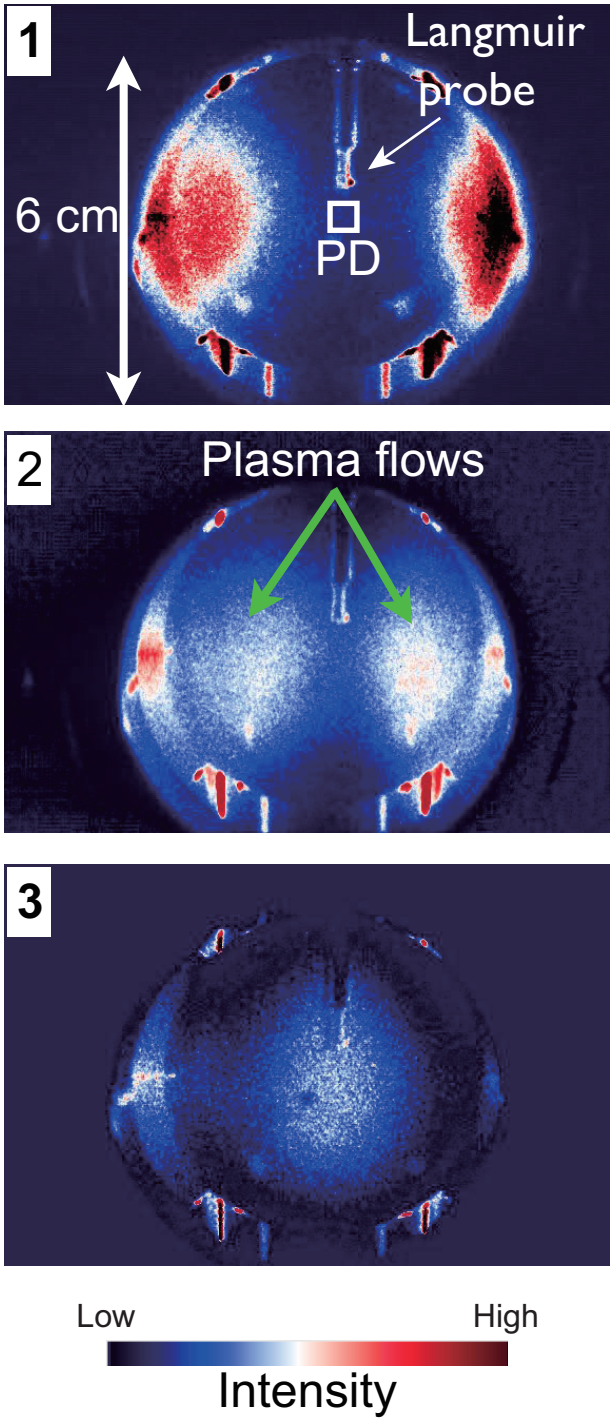

Figure 4.11: Typical frame images of counter-streaming plasma. No. 1, 2 and 3 correspond 3μs, 3.5μs and 4μs from the start of pinch discharge.

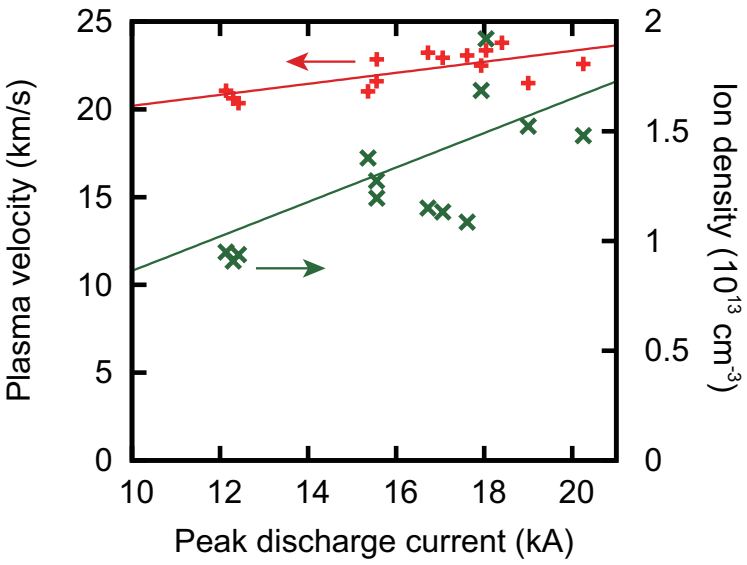

Figure 4.12: Dependence of plasma velocity and ion density on peak discharge current.

The distance from the center of test chamber to the tapered capillary was 8 cm. Then, the plasma velocity and ion density at the center were measured by the Faraday cap. Results of the Faraday cup measurement are shown in Fig. 4.12 where the Faraday cup with a metal aperture of 1 mm was biased to voltage of - 100 V.

Figures 4.13, 4.14, and 4.15 compare typical waveforms of the Langmuir probe and the photodiode signals for independently operated plasma jet (blue curves) and the counter-streaming plasma (red curves). The probe current in these figures denotes ion saturation current signals measured by the Langmuir probe at bias voltage -40V. These experiments were performed at peak discharge current of 10.5 kA, 12.5 kA, and 16.6 kA, respectively. In these experiments, pre-filled gas density was kept at 0.8×10^{-6} g/cm^3.

The rapidly fluctuating probe signals from 0-2μs shown in 4.13(a), 4.14(a), 4.15(a) are due to electro-magnetic noise because the pulsed discharge continued for 2 μs as shown in Fig. 3.13. As shown in Fig. 3.17, the reproducibility of independently operated plasma jet was good enough to discuss effect of the interaction. Three signals were overlaid in Figs. 4.13 and 4.14 for the probe current and light emission waveforms to check the reproducibility of the interacting flow. The plasma drift

velocity was estimated to be ∼20 km/s with TOF by the Langmuir probe. In Fig. 4.13(b), we can see a light emission before the counter-streaming plasmas arrived at the center of the chamber. The light signals during 0 to 2 μs were due to strayed radiation from pinching plasma in the tapered capillary.

The peak probe signals correspond to the time that counter-streaming plasma flows were merged at the center of the chamber as was shown by the corresponding image of framing camera in Fig. 4.11. The photodiode signals could be correlated well to the current signals by the Langmuir probe. When we look at Fig. 4.13, 4.14, 4.15, the light emissions from interacting plasma area always higher than the sum of emissions from independently operated plasma flow. These facts indicate that we could observe an enhancement of light emission clearly from the interacting high-speed plasma flows.

The light emission profile sometimes had two peaks. The arrival times of the first peak (high-energy part) and the second peak (low-energy part) of light emissions are 4.5 μs and 15 μs, respectively. The light emission of low-energy part was lower than high-energy part. A light emission from neutral Ar particle can be the source of the second peak in the low-energy part when we consider that the probe current already became nearly zero at 15 μs.

As shown with these figures, the probe signals decreased and light emission from the counter-streaming plasma flows clearly enhanced than the addition of signals of independent plasma flows. These tendencies were similar in the high-energy part. On the other hand, even after 10 μs, the enhancement of light emission was observed.

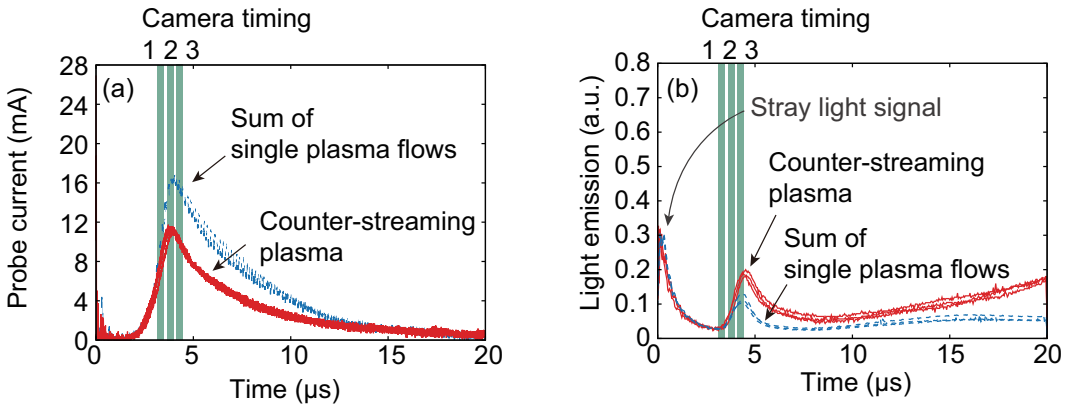

Figure 4.13: Probe signals (a) and light emissions (b) from counter-streaming plasma with pre-filled gas density $\rho_0 = 0.8\times10^{-6}$ g/cm^3, for peak discharge current of 10.5 kA and v_1=20 km/s.

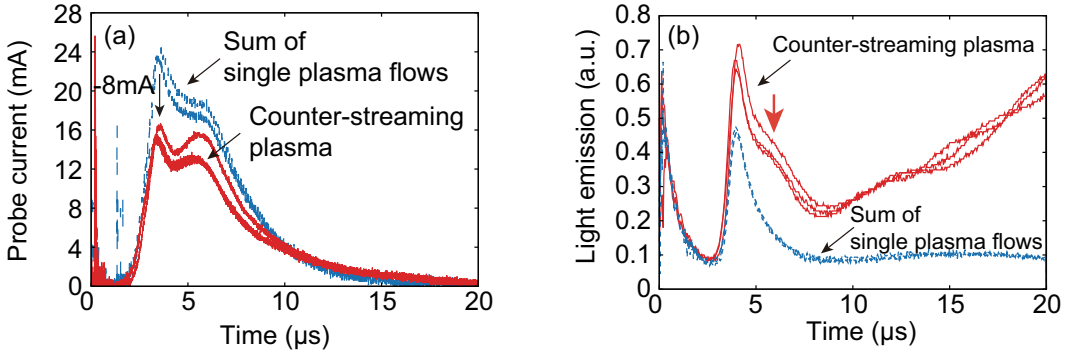

Figure 4.14: Probe signals (a) and light emissions (b) from counter-streaming plasma with pre-filled gas density $\rho_0 = 0.8\times10^{-6}$g/cm^3, for peak discharge current of 12.5 kA and v_2=21 km/s.

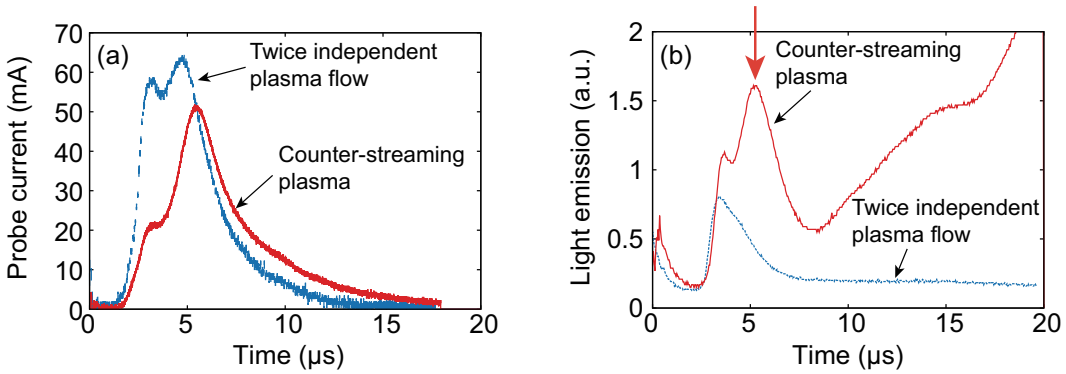

Figure 4.15: Probe signals (a) and light emissions (b) from counter-streaming plasma with pre-filled gas density $\rho_0 = 0.8\times10^{-6}$g/cm^3, for peak discharge current of 16.6 kA and v_1=23 km/s.

As shown in Fig. 4.14, when we increased the discharge current, double peaks were appeared in the probe signal. The second peak of the counter-streaming plasma were enhanced clearly compared with the peaks of sum of single plasma flows. We observed enhancement of light emission both in high-energy part and the low energy-part.

When we compare the results shown in Fig. 4.15, we have to note that the vertical axis was enlarged. When we compare those results with those in Fig. 4.13 and Fig. 4.14, we can conclude that the second peak enhances much more clearly with the increase of discharge current namely increase of flow velocity and/or ion density.

4.3.2 Electron temperature measurements of interacting plasma

We estimated electron temperature from the V-I characteristics of Langmuir probe measurement. Figure 4.16 shows typical results of the probe measurements at 8 cm and at peak flux timing in case of the single plasma flow and counter-streaming plasma flow, where ion density was estimated to be $\sim 10^{13}$ cm^{-3}.

The electron-ion mean free path $\lambda_{ei} = 4\pi\epsilon_0^2 m_e v_e^4/(Z^2 e^4 n_i \ln\Lambda)$ is estimated to be $\sim$1cm in our experimental condition with $v_e = \sqrt{k_B T_e/m_e}$. On the other hand, ion-ion mean free path $\lambda_{ii} = 2\pi\epsilon_0^2 m_i^2 v_{i_d}^4/(Z^4 e^4 n_i \ln\Lambda)$ is estimated to be $\sim$10m at condition corresponding to drift velocity $v_{i_d} = 24$ km/s. Although λ_{ei} was comparable to the scale length of the test chamber, λ_{ii} was much longer than the scale length. These results are indicating that the counter-streaming plasma is interacting under the plasma condition between slightly collisional (for electron-ion) and collision-less (for ion-ion).

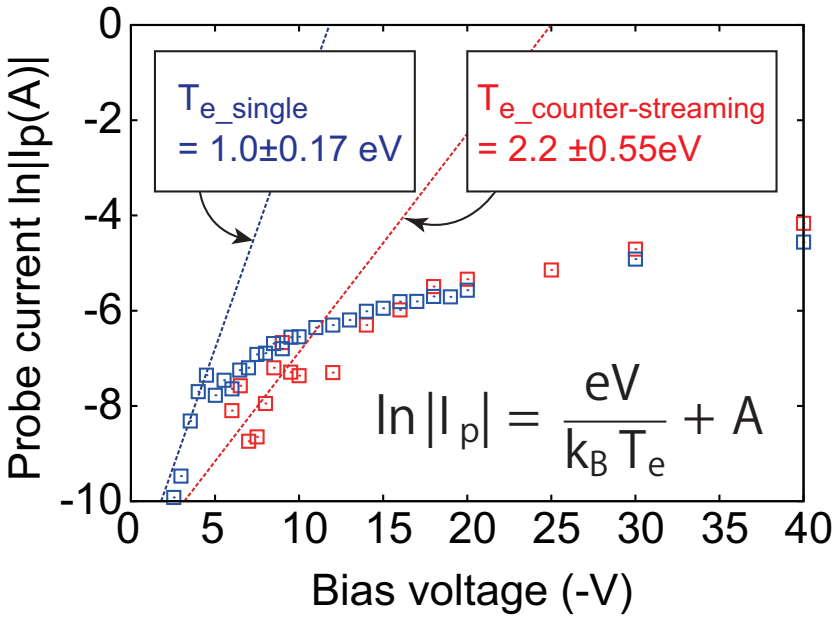

Figure 4.16: Comparison of electron temperature estimated by probe signals in single plasma jet and counter-streaming flow for ρ_0=0.8×10^{-6} g/cm^{-3} and the peak discharge current of 12.5 kA.

4.4 Discussion on the decrease of probe current in the counter-streaming plasma flows

Increase of the ion density in the interacting region by deceleration of drift plasma can induce the enhancement of the light emission. The drift component of probe current can be reduced due to decrease of the ion velocity in the interacting region.

The probe current consists of the ion current and the electron current. If enough negative bias voltage to repel electrons is applied to the Langmuir probe, ion saturation current corresponding local ion density, as described by Eq. (4.3), can be measured in a case of stationary plasma. In our expriment, however, the plasma was moving at a drift velocity v_d with kinetic energy of ∼120 eV which is much larger than the ion temperature.

The probe current I_p in a drifting plasma can be written by:

$$I_p = eZn_iS_p \exp\left(-\frac{1}{2}\right)\sqrt{\frac{k_BT_e}{m_i}} + eZS'_pn_iv_d, \tag{4.8}$$

where S'_p is effective probe area which is normal to the drift velocity.

In the case with probe signal shown in Fig. 4.14(a), the probe current decreased 8 mA at peak flux of the interacting plasma, where terminal resistance was 50 Ω.

Hence, the probe current can be expressed as follows:

$$I_{p,cs} = 2eZn_iS_p \exp\left(-\frac{1}{2}\right)\sqrt{\frac{k_BT'_e}{m_i}} + eZS'_p 2n_iv'_d, \tag{4.9}$$

$$I_{p,ss} = 2eZn_iS_p \exp\left(-\frac{1}{2}\right)\sqrt{\frac{k_BT_e}{m_i}} + eZS'_p 2n_iv_d, \tag{4.10}$$

$$\begin{aligned} I_{p,cs} - I_{p,ss} &= 2eZn_iS_p \exp\left(-\frac{1}{2}\right)\left(\sqrt{\frac{k_BT'_e}{m_i}} - \sqrt{\frac{k_BT_e}{m_i}}\right) \\ &\quad +2eZS'_p n_i(1-\alpha)v_d = -8[\mathrm{mA}], \end{aligned} \tag{4.11}$$

where $I_{p,cs}$ and $I_{p,ss}$ are the probe current of counter-streaming plasma and the sum of single plasma flows; T'_e and $v'_d = \alpha v_d$ are the electron temperature obtained and the plasma velocity in the interacting plasma; $S_p = 4.7 \times 10^{-6}\mathrm{m}^2$ and $S'_p = 1.5 \times 10^{-6}\mathrm{m}^2$. The electron temperature with Langmuir probe measurement are substituted for T_e and T'_e. Then, the ratio of ion flow speed α is estimated for $v_d = 24$ km/s and $n_i = 10^{13}\mathrm{cm}^{-3}$ to be:

$$\alpha = 0.88. \tag{4.12}$$

Therefore, when we consider the energy conservation of ions in an electrostatic potential, we can evaluate a feasible potential formed in the interacting plasma as:

$$\frac{1}{2}m_iv_d^2 = \frac{1}{2}m_iv_d'^2 + e\phi, \quad \phi = 27[\mathrm{eV}]. \tag{4.13}$$

Thus, decrease of the probe current seems to indicate deceleration of the ion in the counter-streaming flow due to formation of electric potential.

4.4.1 Spectroscopic measurements

In order to get detailed information on the atomic processes in the interacting pasma, spectroscopic measurements were tried. Assuming that the electrostatic

Table 4.6: Ar II atomic data [85]

Wavelength (nm)	Relative intensity	$A_{ij}(1/s)$	$E_i - E_j$	Configurations
485.59	83	1.5e7	19.96-22.51	$3p^4(^3P)4p$-$3p^4(^3P)5s$
487.98	2239	8.23e7	17.14-19.68	$3p^4(^3P)4s$-$3p^4(^3P)4p$
488.90	288	1.9e7	17.27-19.80	$3p^4(^3P)4s$-$3p^4(^3P)4p$
490.47	107	3.7e6	18.62-21.14	$3p^4(^3P)3d$-$3p^4(^1D)4p$

potential ϕ of 27 eV was formed in the interacting plasmas, it is considered that electrons were accelerated into the interacting region and can excite and enhance ion population of the energy levels of $\sim$20 eV.

Typical ArII atomic data of which the upper levels are about 20 eV are shown in Table 4.6. In the table, the first column provides the wave length in units of nm, the second means relative intensity, the third stands for radiative decay rate in units of 1/s, the fourth represents energy level, and the final provides configurations.

Figure 4.17 shows the integrated spectrum of radiation emitted from high-speed plasma flows obtained by the whole-view spectrometer. The light emission from the single plasma flow (blue line) was observed in a region between 450 - 650 nm. The light emission from the counter-streaming plasma (red line) was found almost in the same spectral range of the single plasma flow, but the intensity was enhanced more than 2 times. We overlaid a spectrum of the spectral line lamp (green line) for calibration. In this experiment, initial gas density ρ_0 was 0.8 $\times 10^{-6}$ g/cm^{-3} with the peak discharge current of 12.5 kA.

We observed the radiation from counter-streaming plasma in different wavelengths as shown in Fig. 4.18. When we consider that the arrival time of plasma estimated from the peak of the Langmuir probe signal was around 4 μs, the light emissions of the high energy part at ArII 488 nm (red line) and ArII 514 nm (green line) was observed after peak flux. The light emission in the high energy part was not confirmed at AII 611.5 nm (blue line). We consider that the low energy part of plasma almost contributed the enhancement of integrated line emissions from comparison of Fig. 4.17 and 4.18.

The waveforms of line emission had two stages similar to results of photodiode measurement. We observed that the line emissions from the counter-streaming plasma were clearly enhanced at AII 488 nm and ArII 514 nm. However the plasma did not almost exist after 12 μs because probe current at that time was much less than its peak value.

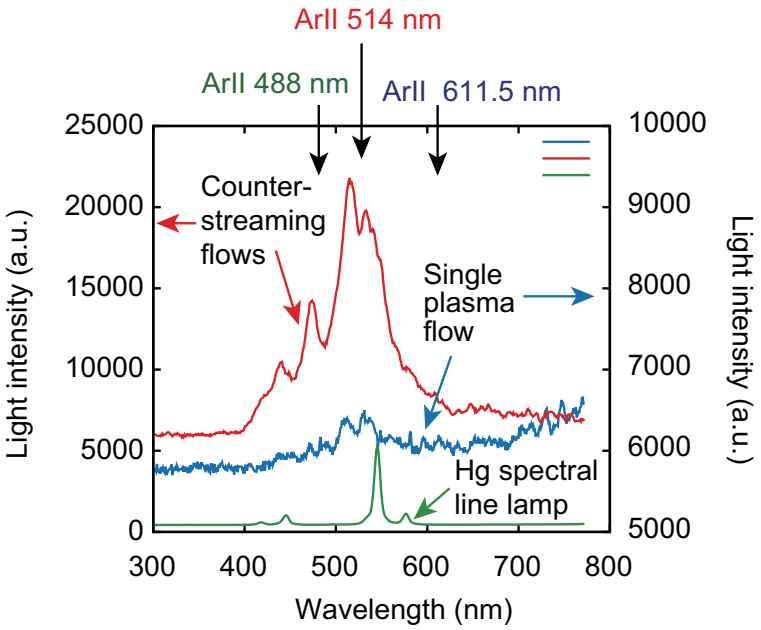

Figure 4.17: Time integrated spectrum of light emission from high-speed plasma flows.

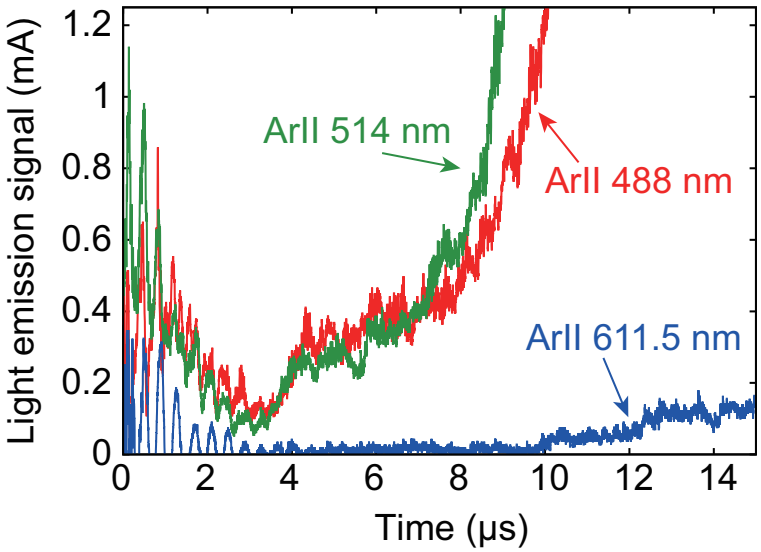

Figure 4.18: Temporal evolution of line emission of ArII in the region of interacting plasma flows.

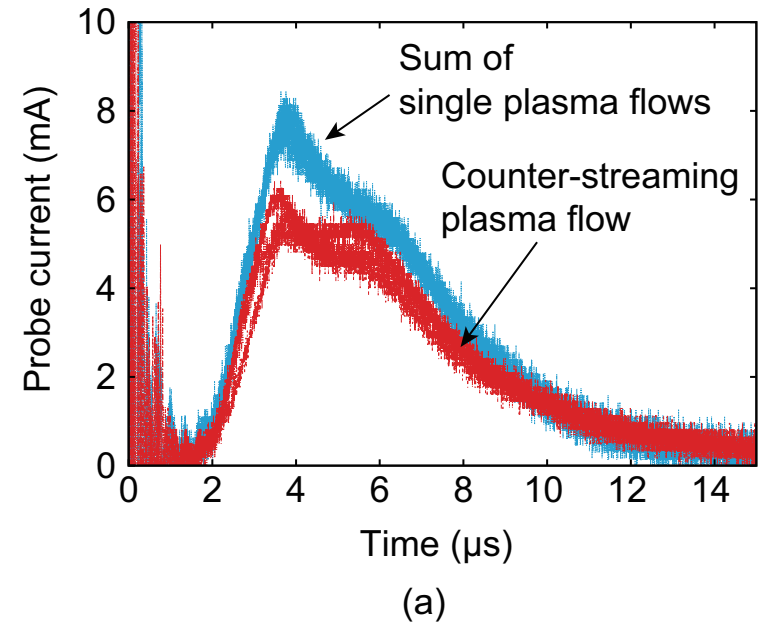

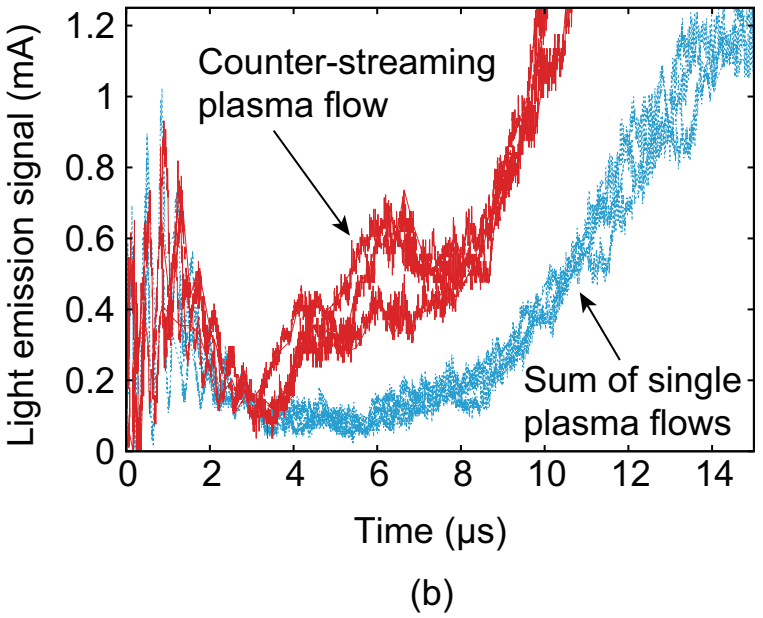

Figure 4.19: Temporal evolution probe signals (a) and emissions from ArII (488 nm) line (b) of sum of independent plasma flows and counter-streaming flows for $\rho_0 = 0.8 \times 10^{-6}\mathrm{g/cm^{-3}}$ and peak discharge current of 12.5 kA.

4.5 Discussion on the enhanced light emission from the counter-streaming plasma flows

The tapered pinch plasma outside the capillary is expected to be in recombining phase, because the TPP is not supplied any energy in the expanding phase. It is known that a recombining Argon plasma emits a radiation in a wide range of wave length containing visible light. Observed line emissions shown in Sec. 4.4.1 indicated existence of ion population with excited levels corresponding to ∼20 eV. In this experimental condition, neutral-neutral collision and ion-neutral collision can be negligible because the mean free path of neutral-neutral is an order of 10 cm. On the other hand, the mean free path between electron and ion is estimated to be comparable to scale length ∼1 cm of the plasma. The estimated electron temperature of ∼1 eV is not enough to excite the ions to the higher level. Although ions had kinetic energy of 120 eV, an order of the speed is ∼10 % of electron thermal speed $\sqrt{k_B T_e/m_e}$. Thus, we consider that the excited ions might be enhanced during the pinching phase in capillary.

If the counter-streaming flows pass through each other without any interactions, the light emission is expected to be simply the sum of the single plasma flows. In Sec. 4.3, the enhancement of the light emission from the counter-streaming plasma flows was shown in comparison with the addition of single plasma flows.

We considered two possible factors of the enhancement of light emission: electron heating and increase of collision rate due to increase of plasma density.

In general, electron heating causes increase of line emission. However in this experiments, electron-ion collision was not enough to be collisional due to the mean free path of an order of scale length of the plasma.

Assuming that electron and ion are collisional, time evolution of population of ions with energy level relating to the light emission can be described by Eq. (2.40). When both population of ions at p level and electrons are twice in comparison with single plasma flow, the collision rate becomes 4 times, in other words, the light emission

becomes twice of the sum of single plasma flow, as follows:

$$\sum_{q<p} C_{q,p} n_e n_q = \sum_{q<p} C_{q,p} (2n_e)(2n_q) = 4 \sum_{q<p} C_{q,p} n_e n_q. \tag{4.14}$$

However the observation revealed the enhanced light emission became more than twice of the sum of single plasma flows at time region after peak plasma flux. The enhancement of line emission from argon ions indicates the possibility of formation of electrostatic potential in the counter-streaming plasmas.

4.6 Summary

In this chapter, we showed that counter-streaming TPP device can perform interaction experiments relevant to astrophysics. An apparatus for conter-streaming experiment was proposed and constructed by a pair of counter-facing TPP devices. Preliminary experiments demonstrated that the TTP devices have good reproducibility to make a comparative study on the interacting high-speed plasma flows with Mach number $\sim$10. The fast framing camera and the photodiode revealed the enhancement of light emission in interacting region of the counter-streaming plasma.

Probe signals (ion saturation) were always smaller than the addition of independent plasma flows. The probe measurements indicated ion flow was decelerated under a condition that the ion-ion mean free path was enough larger than the scale length of test chamber in the experimental region. We also considered the possibility of electrostatic potential formation in the interacting region.

The results of spectroscopy also showed that light emission of ArII lines clearly enhanced more than the addition of those from independent plasma flows, in the interacting region of plasmas. We considered that electrons accelerated by the electrostatic potential contributed to the enhancement of line emission under the condition that the i-e mean free path was almost the scale length of interacting plasma flows.

The results of the probe and spectroscopy measurements indicated existence of a collisionless interaction (for ion-ion collision) in the high-Mach number counter-streaming flows.

Chapter 5

Discussion of Results

5.1 Controllability of counter-streaming taper pinched plasma

The structure of the plasma shocks depends on plasma parameters in upstream of the shock front. Controllability of the plasma parameters is of critical importance for parametric study on the laboratory astrophysics. As shown in Chapter 3, we proposed a tapered pinch discharge device which can form a controllable and well-defined plasma flows.

In Sec. 3.3, we have shown that the plasma velocity and the ion density can be controlled by the experimental condition: peak discharge current, pre-filled gas density, and taper geometry. In the counter-streaming configuration, the ion density can be also controlled by the flight distance of the plasma plume because the plasma is freely expanding.

We also showed that the plasma velocity almost linearly depends on the peak discharge current. Therefore, the combination of above three experimental parameters can control the plasma parameters of the interacting plasma. In particular, we would like to point out that the velocity and the ion density can be controlled separately

by the geometry effect as demonstrated in Fig. 3.23. The synchronization of axially moving plasma with the pinching discharge current sheet contributed independent controllability of plasma velocity and density.

In addition, we defined the zipper velocity and pinching time difference to predict the plasma velocity. An order of the zipper velocity and its tendency on the pinching time difference well agrees with TOF velocity. This indicated that the plasma velocity can be controlled by considering the synchronization.

5.2 Spatial distribution of plasma parameters in high-speed plasma flow

We performed interaction experiments of high-speed plasma flows using the tapered pinch discharge device. We obtained the good reproducibility for the interaction experiments of high Mach number flow relevant to astrophysics through the pre-filled gas supply and the pre-ionization.

In the counter-streaming experiments, the ion density can be also controlled by a distance between the counter-facing capillaries. The ion flux depended on z^{-3} according to the drift-Maxwellian distribution. This shows that the plasma is freely expanding in the test chamber.

We estimated the electron temperature T_e to be $\sim$1 eV and $\sim$2 eV for the single plasma flow and the counter-streaming plasma flows, respectively. We regarded that the electron temperature T_e is almost uniform in the plasma plume, in which electrons follow drifted Maxwellian distributed ions.

Figure 5.1 shows typical time-evolutions of plasma flux (red line), TOF velocity (green dotted line), and ion-ion mean free path (blue line) of the single plasma flow at the interacting region by Faraday cup measurement. In astrophysical plasma, the ion acoustic Mach number M_i is usually larger than an order of 10. Meanwhile M_i of the TPP flow was an order of 10 in a time region of 2.5 - 5.5μs in which the plasma

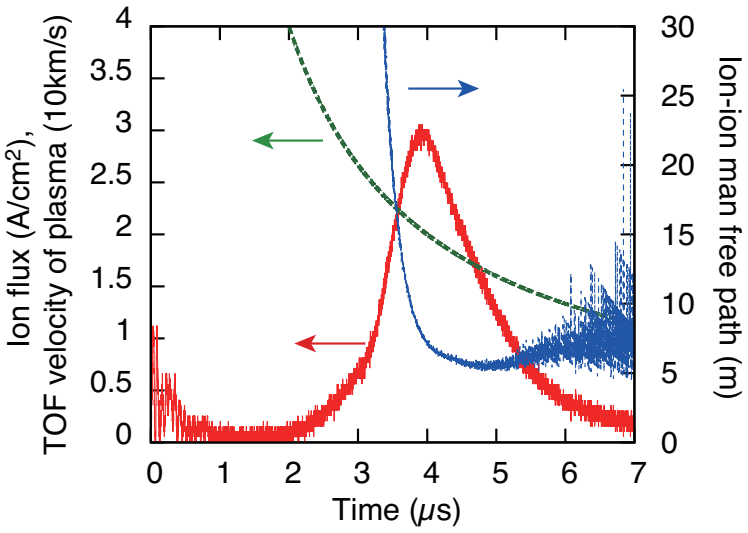

Figure 5.1: Time evolution of the plasma flux (red line), the TOF velocity (green dotted line), and the mean free path of ion-ion (blue line) for TPP with ρ_0=0.8×10^{-6} g/cm^{-3} at peak discharge current of 12 kA.

velocity was 16 - 30 km/s as shown in Fig. 5.1. Hence the astrophysical level of ion acoustic Mach numer M_i was obtained by the counter-stream device in the time region. The mean free path of ion-ion was much larger than the scale length of the chamber as shown in Fig. 5.1. This indicates that the plasma flows were interacting in a condition in which ion-ion collisions are negligible.

5.3 Non-linear enhancement of interaction effects derived from probe current and light emission

When we compared results in Fig. 4.13, 4.14, and 4.15, the enhancements of the second peaks of probe current and light emissions were non-linearly changed with the peak discharge current. When we remind that the relaxation time in collisionless shock was $\omega_{pi}^{-1} \propto \sqrt{m_i/n_i}$, the enhancement of light emission indicates that interaction effect was enhanced with the increase of ion density. These results also seem to indicate a shock structure in the interacting region of counter-streaming high-speed plasma flows.

5.4 Relationship between enhancement of line emission and the decrease of probe current in the counter-streaming plasma flows

In counter-streaming experiments, two cases, with and without interaction between counter-streaming plasma flows, were compared. If the counter-streaming flows pass through each other without any interaction, the probe current and the light emission are expected to be simply the sum of the single plasma flows. In Sec. 4.3, the enhancement of the light emission from the counter-streaming plasma flows and the decrease of the probe current were shown in comparison with the addition of single plasma flows.

The drift component of probe current can be reduced due to decrease of the ion velocity in the interacting region. In contrast, the thermal component of probe current can be increased by the electron heating as shown in Fig. 4.16. Decrease of the probe current seems to indicate deceleration of the ion in the counter-streaming flow due to formation of electric potential.

On the other hand, we considered two possible factors of the enhancement of light emission: electron heating and increase of collision rate due to increase of plasma density. Although electron heating causes increase of line emission in general, electron with temperature of a few eV cannot excite effectively ion population with upper level of ~ 20 eV. Assuming that electron-ion collision was enough to be collisional, the line emission from counter-streaming plasmas is expected to become four times larger than that from a single plasma flow if the single plasma flows are assumed to simply interpenetrate each other. However in this experiments, electron-ion collision was not enough to be collisional due to mean free path of an order of scale length of the plasma.

The observation revealed the enhanced light emission became more than twice of the sum of single plasma flows at time region after peak plasma flux. The probe measurements indicated formation of the electrostatic potential with an order of 20

eV. The enhanced line emission of ArII (488 nm: $3p^4 4s$-$3p^4 4p$) may be occurred by collision between electrons accelerated by the electrostatic potential and ions.

Meanwhile, ion-ion collision can cause transfer between different l levels before an electron drops to lower states via photon radiation. This l-mixing effects by ion-ion collision may affect the line emission. The enhanced line emission of ArII (488 nm: $3p^4 4s$-$3p^4 4p$) may reflect this process [83, 84]. Nevertheless the effect of l-mixing exists in the interacting plasma, ion-ion collision can be neglected based on plasma parameters estimated in this experiments.

Contribution of these two effects depends on the wavelength. However, spectroscopic measurements were performed with spectral resolution of 6 nm because intensity of line emission was small. Available ArII atomic data are shown in Table 4.6 in which lines in band of the spectral resolution of spectrometer. Spectroscopic measurements with higher resolution than this preliminary experiments is needed to further discussion of the effect of l-mixing and collision rate.

5.5 Concluding Remarks

We performed an interaction experiment of high-speed plasma flows with the controllable and well-defined tapered pinch plasma device. The effect of interaction was evaluated by a Langmuir probe, a photo diode, and a spectrometer. Results showed decrease of ion saturation current, and increase of light emission.

The enhancement of ArII line emission was more factor 2, namely more than the sum of single flows. In the experiments, mean free path of electron-ion was an order of the scale length of plasma flow. However the fact that the enhancement of ArII line emission and photodiode signal were more than factor 2 indicates existence of interaction mechanism independent of classical binary collisions of electron-ion and ion-ion.

The decrease of probe current indicated deceleration of ion flow. The electrostatic potential corresponding to the deceleration was estimated to be 20 % of the kinetic energy of high-speed Ar flow. The interaction occurred under a condition that the

scale length of the plasma flow was much smaller than the mean free path of ion-ion. In other words, the high-speed ion flow dissipated almost 20 % of their kinetic energy without ion-ion interaction. Non-linear enhancements of the line emission of Ar II and the probe current also seem to indicate a strong interaction in the collision-less condition.

Chapter 6

Conclusions

In this thesis, we have discussed a tapered pinch discharged plasma device to perform laboratory astrophysics experiments.

Chapter 1 started with an introduction on a brief history of space exploration. An explanation of the influence of cosmic rays on human body and interaction of high-speed plasma flows on terrestrial environment followed the introduction. We have pointed out that the cosmic rays can be formed in astrophysical shocks and those energy spectrum are depending on the shock structure of which structure is strongly affected by the plasma parameters in the upstream of the shock front. We also pointed out that the interactions of high-speed plasma flows; namely formations of shock, magnetic reconnections, and cosmic rays generally exist in the space. Besides we indicated the importance of parametric study of the phenomena for laboratory astrophysics with a brief review of previous experimental studies.

Chapter 2 overviewed the shock structure. We showed that the complicated structures are depending on the plasma parameters and explained that dissipation processes in strong shock waves enhance the complexity. We mentioned importance of scaling parameters for well-organized analysis of the complex shock structure. We also explained the importance of the formation time of the plasma flow and the controllability of the plasma devices on the experimental approach to the astrophysical phenomena.

Chapter 3 showed a new type of plasma source using a taper pinch capillary discharge for the parametric study on the strong shock waves. By a proof-of-principle experiment, we have shown that the tapered pinch plasma (TPP) was controlled by the pre-filled gas density in the capillary, the peak discharge current and the taper geometry. We could make clear that the peak flux outside the tapered capillary can be estimated by a drift-Maxwellian distribution. We also mentioned that the reproducibility of the TPP device is sufficient for performing laboratory astrophysics experiments.

Chapter 4 presented counter-streaming plasma experiments relevant to astrophysical phenomena. We explained that we have constructed an experimental apparatus that can drive counter-streaming plasma flows with Mach number $\sim$10 by a pair of the tapered pinch discharge devices. We showed that the counter-streaming TPP device can provide a controllable and well-defined interacting plasma with a wide parameter range of fluid velocity and plasma density. With preliminary experiment, enhancements of light emission from the interacting plasma and decrease of probe current were observed compared with the sum of the single plasma flows as a base.

In Chapter 5, we discussed the results obtained in this study. The discussion was concentrated on the interaction of high-speed plasma flows in collision-less condition. We indicated three possible factors of the enhancement of the light emission; increase of effective collision rate between ion and electron, deceleration of the ions, and/or electron heating in the interacting region of the counter-streaming flow.

In summary, we could demonstrate that a reproducible, controllable and well-defined interaction experiments are possible with high-speed plasma flows using the tapered pinch discharge. Thanks to the moderate spatio-temporal scale of the plasma, the measurement of the plasma parameters was possible with conventional and well-established diagnostics in the interacting region. All of the observations carried out with those diagnostics are indicating that high-speed Ar flows dissipate almost 20 % of ion kinetic energy in the interacting region without ion-ion collisions.

In the space, plasma shocks with Mach number of ~ 100 are formed. Plasma flow with the high-Mach number could not be formed not only in our laboratory astrophysical experiments, also in previous studies. We would like to emphasize that laboratory astrophysics experiments in wider region of the plasma parameters should contribute deeper understanding the structure of plasma shock waves that exist widely in the space.

Bibliography

[1] R.D. Blandford and D. Eichler, "Particle Acceleration at Astrophysical Shocks: A Theory of Cosmic Ray Origin", *Phys. Rep.*, **154**, 1 (1987).

[2] M. Takeda, N. Hayashida, K. Honda, N. Inoue, K. Kadota, F. Kakimoto, K. Kamata, S. Kawaguchi, Y. Kawasaki, N. Kawasumi, H. Kitamura, E. Kusano, Y. Matsubara, K. Murakami, M. Nagano, D. Nishikawa, H.Ohoka, N.Sakaki, M. Sasaki, K. Shinozaki, N.Souma, M.Teshima, R. Torii, I. Tsuchima, Y. Uchihori, T. Yamamoto, S, Yoshida, and H. Toshii, "Extension of the Cosmic-Ray Energy Spectrum beyond the Predicted Greisen-Zatsepin-Kuz'min Cutoff ", *Phys. Rev. Lett.*, **81**, 1163 (1998).

[3] S.P. Swordy, "The Energy Spectra and Anisotropies of Cosmic Rays", *Space Science Reviews.*, **99**, 85 (2001).

[4] J.A. Angelo, "Nuclear Technology", (Greenwood Press, Westport, 2004).

[5] L. I. Dorman, "Cosmic rays and space weather: effects on global climate change", *Ann. Geophys.*, **30**, 9 (2012).

[6] E. Dubinin, M. Fraenz, A. Fedorov, R. Lundin, N. Edberg, F. Duru, and O. Vaisberg, "Ion Energization and Escape on Mars and Venus", *Space Sci. Rev.*, **162**, 173 (2011).

[7] R. Lundin, "Ion Acceleration and Outflow from Mars and Venus: An overview", *Space Sci. Rev.*, **162**, 309 (2011).

[8] E. Fermi, "On the Origin of the Cosmic Radiation", *Phys. Rev.*, **31**, 1169 (1949).

[9] A.M. Hillas, "Can diffusive shock acceleration in supernova remnants account for high-energy galactic cosmic rays?", *J. Phys. G: Nucl. Part.Phys.*, **31**, R95 (2005).

[10] Y. Ohsawa, "Nonstochastic Particle Acceleration in Collisionless Shock Waves", *Physica Scripta,*, **T107**, 32 (2004).

[11] V.G. Eselevich, "Shock-wave Structure in Collisionless Plasmas From Results of Laboratory Experiments", *Space Science Rev.*, **32**, 65 (1982).

[12] NASA web site, http://www.nasa.gov/connect/chat/solar_chat.html

[13] Chandra X-ray observatory web site, http://chandra.harvard.edu/photo/2005/sn1006/

[14] ESA web site, http://spaceinimages.esa.int/Images/2007/11/Interaction_between_Venus_and_the_solar_wind2

[15] J. A. Biretta et al., Hubble Heritage Team (STScI /AURA), NASA, http://apod.nasa.gov/apod/ap000706.html

[16] T. J. Horcath, D. M. Tomek, K. T. Berger, S. C. Splinter, J. N. Zalameda, P. W. Krasa, S. Tack, R.J. Schwartz, D.M. Gibson, and A. Tietjen, "The HYTHIM project: Flight Thermography of the Space Shuttle During Hypersonic Reentry", AIAA 2010-241, 4 (2010).

[17] T. Ozawa, Jiaqiang Zhong, and D.A. Levin, "Development of Kinetic-based Energy Exchange Models for Noncontinuum, Ionized Hypersonic Flows", *Phys. Fluids*, **20**, 046102 (2008).

[18] C.E. Rakowski, P. Ghavamian, and J.P. Hughes, "The Physics of Supernova Remnant Blast Waves. II. Electron-Ion Equilibration in DEM L71 in the Large Magellanic Gloud",*Astrophys. J.*, **590**, 846 (2003).

[19] K. Koyama, R. Petre, E.V. Gotthelf, U. Hwang, M. Matsuura, M. Ozaki, and S.S. Holt, "Evidence for shock acceleration of high-energy electrons in the supernova remnant SN1006", *Nature*, **378**, 255 (1995).

[20] F.A. Aharonian, A.G. Akhperjanian, K.-M. Aye, A.R. Bazer-Bachi, *et al.*, "High-energy particle acceleration in the shell of a supernova remnant", *Nature*, **432**, 75 (2004).

[21] J. W. M. Paul, L. S. Holmes, M. J. Parkinson and J. Sheffield, "Experimental Observations on the Structure of Collisionless Shock Waves in a Magnetized Plasma", *Nature*, **208**, 5006, 133 (1965).

[22] M.R. Brown, C.D. Cothran, M. Landremanm, D. Schlossberg, and W.H. Matthaeus, "Experimental Observation of Energetic Ions Accelerated by Three-dimensional Magnetic Reconnection in a Laboratory Plasma", *Astrophys. J.*, **577**, L63 (2002).

[23] R.P. Drake, "High-Energy-Density Physics: Fundamentals, Inertial Fusion, and Experimental Astrophysics", (Springer, New York, 2006).

[24] R. P. Drake, "The Design of Laboratory Experiments to produce Collisionless Shocks of Cosmic Relevance", *Phys. Plasmas*, **7**, 4690 (2000).

[25] D. D. Ryutov, B.A. Remington, H.F. Robey, and R.P. Drake, "Magnetohydrodynamic Scaling: From Astrophysics to the Laboratory", *Phys. Plasmas*, **8**, 5, 1804 (2001).

[26] A.R.Bell, P.Choi, A.E.Dangor, O.Willi, D.A.Bassett, and C.J.Hooker, "Collisionless Shock in a laser-produced ablating plasma", *Phys. Rev. A*, **38**, 1363 (1988).

[27] J.S.Ross, S.H.Glenzer, P.Amendt, R.Berger, L.Divol, N.L.Kugland, O.L.Landen, C.Plechaty, B.Remington, D.Ryutov, W.Rozmus, D.H.Froula, G.Fiksel, C.Sorce, Y.Kuramitsu, T.Morita, Y.Sakawa, H.Takabe, R.P.Drake, M.Grosskopf, C.Kuranz, G.Gregori, J.Meineche, C.D.Murphy, M.Koenig, A.Pelka, A.Ravasio, T.Vinci, E.Liang, R.Presura, A.Spitkovsky, F.Miniati, and H.-S. Park, "Characterizing Counter-streaming Interpenetrating Plasmas Relevant to Astrophysical Collisionless Shocks", *Physics of Plasmas*, **19**, 056501 (2012).

[28] M.Inutake,A.Ando,K.Hattori,H.TobariandT.Yagai, "Characteristics of a Supersonic Plasma Flow in a Magnetic Nozzle", *J. Plasma Fusion Res.*,**78**, 1252 (2002).

[29] S.Minami, P.J.Baum, G.K.Kamin, Y. Takeya and R.S. White, "Laboratory Behavior of a Plasma Plume Injected into the Magnetized Plasma Flow", *J. Geomag. Geoelectro.*, **40**, 1283 (1988).

[30] R. Rana, S.Minami, S.Takechi, A.I.Podgorny and I.M.Podgorny, "The Dynamical Behavior of the Earth's Magnetosphere Based on Laboratory Simulation", *Earth Planets Space*, **56**, 1005 (2004).

[31] A.G. Ponomarenko, Yu.P.Zakharov, V.M.Antonov, E.L.Boyarintsev, A.V.Melekhov, V.G.Posukh, I.F. Shaikhislamov, and K.V. Vchivkov, "Simulation of Strong Magnetospheric Disturbances in Laser-produced Plasma Experiments", *Plasma Phys. Control. Fusion*, **50**, 074015 (2008).

[32] C. Constantin, W.Gekelman, P.Pribyl, E.Everson, D.Schaeffer, N.Kugland, R.Presura, S.Neff, C.Plechaty, S.Vincena, A.Collette, S.Tripathi, M.Villagran Muniz, C.Niemann, "Collsionless Interaction of an Energetic Laser Produced Plasma with a Large Magnetoplasma", *Astrophys Space Sci.*, **322**, 155 (2009).

[33] A.D.Craig, "Laboratory Investigation of Shock waves in a Weakly Magnetized Plasma",*Plasma Physics*, **17**, 1111 (1975).

[34] D.Mourenas, J.Vierne, F.Siemonet, V.I.Krauz, S.Nikulin, V.V.Mialton and M. A. Karakin, "Laboratory and Computer Simulations of Super-Alfvénic Shocks in a Weakly Ionized Medium", *Physics of Plasmas*, **10**, 605 (2003).

[35] K. Kondo, M. Nakajima, T. Kawamura, K. Horioka, "Compact Pulse Power Device for Generation of One-Dimensional Strong Shock Waves", *Rev. Sci. Instrum.*, **77**, 036104 (2006).

[36] S.V.Lebedev, D.Ampleford, A.Ciardi, S.N.Bland, J.P.Chittenden, M.G. Haines, A.Frank, E.G.Blackman, and A. Cunningham, "Jet Deflection via Crosswinds: Laboratory Astrophyscial Studys", *Astrophys. J.*, **616**, 988 (2004).

[37] V.V. Aleksandrov, E.V. Grabovski, G.G. Zukakishvili, K.N. Mitrofanov, S.F. Medovshchikov and I.N. Frolov, "Experimental Study of the Ion Flux Parameters and Anode Plasma Dynamics in the Angara-5-1 Facility", *Plasma Physics Reports*, **34**, 830 (2008).

[38] K. Adachi, M. Nakajima, T. Kawamura, and K. Horioka, "Formation Mechanism of Dense High-Speed Plasma Flow in Tapered Capillary Discharge", *Plasma and Fusion Research: Rapid Communications*, **6**, 1201019 (2011).

[39] K. Adachi, M. Nakajima, K. Horioka, "Control of Taper-Pinch Plasma by Geometrical Parameters of Capillary", *IEEE Transaction on Plasma Science*, **40**, 12, 3308 (2012).

[40] Fracis F. Chen, "Introduction to Plasma Physics", (Plenum Press, New York, 1974).

[41] M.E.Dieckmann, H.Ahmed, G.Sarri, D.Doria, I.Kourakis, L.Romagnani, M.Pohl, M.Borghesi, "Parametric Study of Non-relativistic Electrostatic Shock and the Structure of their Transition Layer", *Phys. Plasmas*, **20**, 042111 (2013).

[42] D.W. Forslund and J.P. Freidberg, "Theory of Laminar Collisionless Schocks", *Phys. Rev. Lett.*, **27**, 1189 (1971).

[43] R.J.Taylar, D.R.Baker, and H. Ikezi, "Observation of Collisionless Electrostatic shocks", *Phys. Rev. Lett.*, **24**, 206 (1970).

[44] R.W.Means, F.V. Coroniti, A.Y. Wong, and R.B. White, "Turbulence in Electrostatic Ion Acoustic Shocks", *Phys. Fluids*, **16**, 2304 (1973).

[45] G.Sorasio, M.Marti, R.Fonseca, and L.O.Silva, "Very High Mach-Number Electrostatic Shock in Collisionless Shock", *PRL*, **96**, 045005 (2006).

[46] Russel M. Kulsrud, "Plasma Physics for Astrophysics", (Prinstom University Press, Princeton, 2005).

[47] E. Priest and T. Forbes, "Magnetic Reconnection, MHD Theory and Application", (Cambridge University Press, Cambridge, 2000).

[48] H.E. Petschek, "Magnetic Field Annihilation", *The Physics of Solar Flares*, Proceeding of the AAS-NASA Symposium, 425 (1964).

[49] D. Biskamp, "Magnetic Reconnection", *Phys. reports*, **237**, 179 (1994).

[50] D. Salzmann, "Atomic Physics in Hot Plasmas", (Oxford University Press, New York, 1998).

[51] T. Fujimoto, "Plasma Spectroscopy", (Oxford University Press, New York, 2004).

[52] H.W. Liepmann and A. Roshko, "Elements of Gasdynamics", (Dover publications, New York, 1956).

[53] Y.B. Zel'dovich and Y.P. Raizer, "Physics of Shock Waves and High-Temperature Hydrodynamic Phenomena", (Academic Press, New York, 1967)

[54] D.W. Forslund and C.R. Shonk, "Numerical Simulation of Electrostatic Counterstreaming Instabilities in Ion Beams", *Phys. Rev. Lett.*, **25**, 281 (1970).

[55] J.P. Phillips, S.J. Bame, W.C. Feldman, J.T. Gosling, C.M. Hammond, D.J. McComas, B.E. Goldstein, and M. Neugebauer, "Ulysses Solar Wind Plasma Observations during the Declining Phase of Solar Cycle 22", *Adv. Space. Res.*, **16**, 9, 85 (1995).

[56] H.L. Marshall, C.R. Canzares, R. Hillwig, A. Mioduszewski, M. Rupen, N.S. Schlz, M.Nowak, and S. Heinz, "Multiwavelength Observations of the SS 433 Jets", *Astrophys. J.*, **775**, 75 (2013).

[57] M.N. Rosenbluth, W.M. MacDonald and D.L. Judd, "Fokker-Planck Equation for an Inverse-Square Force", *Phys. Rev.*, **107**, 1 (1957).

[58] D.H. McDaniel, M.G. Mazarakis, D.E. Bliss, J.M. Elizondo, H.C. Harjes, H.C. Ives III, D.L. Kitterman, J.E. Maenchen, T.D. Pointon, S.E. Rosenthal, D.L. Smith, K.W. Struve, W.A. Stygar, E.A. Weinbrecht, D.L. Johnson, J.P. Corley, "The ZR Refurbishment Project", *AIP Conf. Proc. Dense Z-Pinches*, **651**, 23 (2002).

[59] D.H. Cohen, J.J. MacFarkane, J.E. Bailey, and D.A. Liedahl, "X-ray Spectral Diagnostics of Neon Photoionization Experiments on the Z-machine", *Rev. Sci. Instrum.*, **74**, 1962 (2003).

[60] Sandia National Laboratories web site, http://www.sandia.gov/z-machine/

[61] N.A. Strokin, A.E. Indyukov, and G.N. Kichigin, "Relaxation of the Shock Wave-reflected Ion Beam, and Generation of Hot Electrons", *J. Geophys. Res.*, **103**, 20540 (1998).

[62] A.D. Craig, "An Experimental Investigation of Slow-mode Shock Waves", *J. Plasma Phys.*, **12**, 149 (1974).

[63] M.G.Haines, "A Review of the Dense Z-pinch", *Plasma Phys. and Control. Fusion*, **53**,168 (2011) .

[64] F.S. Felber, F.J. Wessel, N.C. Wild, H.Um Rahman, A. Fisher, C.M. Fowler, M.A. Liberman, and A.L. Velikovich, "Ultrahigh Magnetic Fields Produced in a Gas-puff Z Pinch", *J. Appl. Phys.*, **64**, 15 (1988).

[65] T.E. Markusic, K.A. Polzin, E.Y. Choueiri, M. Keidar, L.D. Boyd, and N. Lepsetz, "Ablative Z-Pinch Pulsed Plasma Thruster", *J. Propul. Power*, **21**, 392 (2005).

[66] K. Horioka, M. Nakajima, T. Aizawa and M. Tsuchida, "High Density Plasmoid Acceleration by Phased Implosion of Capillary Z-pinch and its Application to Hyper-velocity Projectile Acceleration", *AIP Proc. Dense Z-Pinches*, **CP409**, 311 (1997).

[67] J. Canto, G. Tenorio-Tagle, M. Rozyzka, "The Formation of Interstellar Jets by the Convergence of Supersonic Conical Flows", *Astronomy and Astrophysics*, **192**, 287 (1988).

[68] S.T. Pai, Q. Zhang, "Introduction to High Power Pulse Technology", (World Scientific Publishing, Singapore, 1995).

[69] A.A. Kim, M.G. Mazarakis, V.A. Sinebryukhov, B.M. Kovalchuk, V.A. Visir, S.N. Volkov, F.Bayol, A.N. Bastrikov, V.G. Durakov, S.V. Frolov, V.M. Alexeenko, D.H. McDaniel, W.E. Fowler, K. LeChien, C. Olson, W.A. Stygar, K.W. Struve, J. Porter, and R.M. Gilgenbach, "Development and tests of fast 1-MA linear transformer driver stages", *Physical Review Special Topics -Accelerators and Beams*, **12**, 050402 (2009).

[70] N. Qi, J. Schein J. Thompson, P. Coleman, M. McFarland, R.R. Prasad, M. Krishnan, B.V. Weber, B.G. Moosman, J.W. Schumer, "Z Pinch Imploding PlasmaDensity Profile Measurements Using a Two-Frame Laser Shearing Interferometer", *IEEE Transaction on Plasma Science*, **30**, 227 (2002).

[71] P.L. Coleman, D.C. Lamppa, R.E. Madden, K. Wilson-Elliott, B. Jones, D.J. Ampleford, D.E. Bliss, C. Jennings, A. Bixler, and M. Krishnan, "Development and Use of a Two-dimensional Interferometer to Measure Mass Flow from a Multi-shell Z-pinch Gas Puff", *Rev. Sci. Instrum.*, **83**, 083116 (2012).

[72] K. Adachi, M. Nakajima, T. Kawamura, and K. Horioka, "Formation of Dense, Electromagnetically Accelerated Plasma for Laboratory Astrophysics", *EPJ Web of Conferences*, **59**, 10003 (2013).

[73] R. Kelly and R.W. Dreyfus, "On the Effect of Knudsen-layer Formation on Studies of Vaporization, Sputtering, and Desorption",*Surface Science*, **198**, 263 (1988).

[74] R.A. Bosch, R.L. Berger, B.H. Failor, N.D. Delamater, and R.L. Kauffman, "Collision and Interpenetration of Plasmas Created by Laser-illuminated Disk", *Phys. Fluids B*, **4**, 979 (1992).

[75] C. Thoma, D.R. Welch, and S.C. Hsu, "Particle-in-cell Simulations of Collisionless Shock Formation via Head-on Merging Two Laboratory Supersonic Plasma Jets", *Phys. Plasmas.*, **20**, 082128 (2013).

[76] T.N. Kato and H. Takabe, "Electrostatic and Electromagnetic Instabilities Associated with Electrostatic Shocks: Two-dimensional Particle-in-cell Simulation", *Phys. Plasma*, **17**, 032114 (2010).

[77] Hamamatsu Photonics Catalog No. KPIN1050J02 (2013).

[78] R.L. Merlino, "Understanding Langmuir Probe Current-voltage Characteristics", *Am. J. Phys.*, **75**, 1078 (2007).

[79] S. Chen and T.Sekiguchi, "Instantaneous DirectDisplay System of Plasma Parameters by Means of Triple Probe", *J. Appl. Phys.*, **36**, 2463 (1965).

[80] M. Kamitsuma, S. Chen and J. Chang, "The Theory of the Instantaneous Triple-probe Method for Direct-Display of Plasma Parameters in Low-density Collisionless Plasmas", *J. Phys. D: Appl. Phys.*, **10**, 1065 (1976).

[81] N.A. Gatsonis, L.T. Byrne, J.C. Zwahlen, E.J. Pencil, and H. Kamhawi, "Current-Mode Triple and Quadruple Langmuir Probe Methods with Applications to Flowing Pulsed Plasmas", *IEEE Transaction on Plasma Sci.*, **32**, 2118 (2004).

[82] Hamamatsu Photonics K.K., "PHOTOMULTIPLIER TUBES -Basics and Applications-, third edition", (2007).

[83] R.J. Fonek, D.S. Darrow, and K.P. Jaehnig, "Determination of Plasma-ion Velocity Distribution via Charge-exchange Recombination Spectroscopy", *Pys. Rev. A*, **29**, 3288 (1984).

[84] R.M. Pengelly and M.J. Seaton, "Recombination Spectra: II. Collisional Transitions between States of Degenerate Energy Levels", *MNRAS*, **127**, 165 (1964).

[85] National Institute of Standards and Technology: Atomic Spectra Database, http://physics.nist.gov/PhysRefData/ASD.index.html

Acknowledgements

This thesis has been supported tremendously from numerous people. I would like to express my deepest gratitude to many people.

First and foremost, I want to acknowledge my supervisor Professor Kazuhiko Horioka at Tokyo Institute of Technology. He raised me patiently from a bachelor student to a Ph.D with his great enthusiasm and immense knowledge to science. His guidance helped me in all the time of research and writing of this thesis. I could not have imagined having a better advisor and mentor for my Ph.D study.

My special thanks go to Assistant Professor Mitsuo Nakajima at Tokyo Institute of Technology for his enormous support. He gave me many comment and proposal especially on constructing the experimental device, and also he always gave me pointed comments and insightful questions on this work. In addition, he taught me broad range of matter not only fundamental physics and engineering, biology, and more general issues such as social problems and economics. Through conversation with him, I had many chances to look back on my work in a different way. I am very grateful to Professor Jun Hasegawa, and Associate Professor Tohru Kawamura at Tokyo Institute of Technology for giving me significant comments on research activities through seminars and conferences. Prof. Hasegawa advised and helped me technical things on experiment in diverse way, and Prof. Kawamura suggested me to take consideration through atomic physics. Without their helpful suggestions, this work has never completed.

Beside my advisor, I would like to thank committee members on this thesis, Professor Yoshihiro Okuno and Professor Hiroshi Akatsuka at Tokyo Institute of Technology. I also want to thank Professor Tsutomu Takahashi for joining to the committee member and for spending his valuable time to examine this dissertation.

I would like to extend special thank to Horioka, Kohno, Kawamura, Hasegawa and Takayama laboratory members; Dr. Kotaro Kondo, Dr. Tohru Sasaki, Dr. Takashi Kikuchi Dr. Naoki Tajima, Mr. Yutaka Aoyama, Mr. Yuji Otsuka, Mr. Sota Kinoshita, Dr. Kazumasa Takahashi, Mr. Masakazu Tomii, Mr. Daisuke Nunotani, Mr. Takeshi Hosoi, Mr. Yuuki Uchida, Mr. Kazuki Takahashi, Mr. Kenji Hayashi, Mr. Yoshifumi Miyazaki, Mr. Kotaro Iwasaki, Mr. Yusuke Kuroda, Mr. Akira Nakayama, Mr. Takuya Ozawa, Mr. Yujin Ogata, Hiroki Sakai, Mr. Shunsuke Ikeda, Mr. Yasuo Sakai, Mr. Shuhei Yamamura, Mr. Nao Tatsumura, Mr. Takashi Yoshimoto, Mr. Liu Xiagguang, Ms. Yamamoto Akiko, Mr. Takayuki Ito, Ms. Yukako Hachiya Mr Ken Yonezawa, Mr. Seika Ryu, Mr. Masashi Masuda, Mr. Naoya Munemoto, Ms. Fumika Isono, Mr. Kaneo Kato, Mr. Koki Kanou, Mr. Akihito

Tezuka, Mr. Satoru Kanamaru, Mr. Kenta Kawaguchi. Through many conversations and discussions with them, my 6 years campus life at Horioka laboratory became very very fruitful, and brought me great growth in my mental and attitude to various issues.

Last in this list, but first in my heart, I would like to thank my family, my dormitory friends and my life partner for all their love and encouragement. Without them, this work would never have come into existence.

Thank you my parents for having respects to my will, taking snug home that can return at any time, and especially giving me a chance to dedicate myself to this study. For my two brothers who are realizing their respective dreams. Their existence encouraged me much. For my dormitory friends who come in contact with almost like a family. And for Miho who is closest to, give her love and supported me during my last year of Ph.D. Thank you.

Koichiro Adachi
Tokyo Institute of Technology
February 2014